

**NOAA NESDIS  
CENTER for SATELLITE APPLICATIONS and RESEARCH  
ALGORITHM THEORETICAL BASIS DOCUMENT**

**JPSS Aerosol Detection (Suspended  
Matter) Product**

NOAA/NESDIS/STAR

Version 1.1  
April 15, 2016

# TABLE OF CONTENTS

LIST OF TABLES .....	4
LIST OF FIGURES .....	5
LIST OF ACRONYMS .....	8
1 INTRODUCTION .....	10
1.1 Purpose of This Document.....	10
1.2 Who Should Use This Document .....	10
1.3 Inside Each Section.....	10
1.4 Related Documents .....	11
1.5 Revision History .....	11
2 OBSERVING SYSTEM OVERVIEW.....	11
2.1 Products Generated .....	11
2.2 Instrument Characteristics .....	13
3 ALGORITHM DESCRIPTION.....	18
3.1 Algorithm Overview .....	18
3.2 Processing Outline .....	18
3.3 Algorithm Input .....	19
3.3.1 Primary Sensor Data .....	19
3.3.2 VIIRS Product Precedence and Ancillary Data .....	20
3.4 Theoretical Description.....	24
3.4.1 Physics of the Problem.....	24
3.4.2 Mathematical Description.....	38
3.4.3 Algorithm Output.....	68
4 Test Datasets and Outputs.....	70
4.1 Proxy Input Data Sets and validation data.....	70
4.1.1 Input Data sets.....	70
4.1.2 Truth data.....	71
4.2 Output from proxy data sets.....	74
4.2.1. Output for Dust Detection.....	74
4.2.2. Output for Smoke Detection .....	79
4.1.3. Product Performance Evaluations.....	83
4.3 Framework run and validation .....	86
4.1.1. Framework run.....	86
4.1.2. Consistency tests with S-NPP VIIRS granules.....	86
4.1.3. Results from Framework run with global S-NPP VIIRS observation .....	87
5. PRACTICAL CONSIDERATIONS.....	88
5.1 Numerical Computation Considerations.....	88
5.2 Programming and Procedural Considerations .....	88
5.3 Quality Assessment and Diagnostics .....	89
5.4 Exception Handling .....	89
5.5 Algorithm Validations .....	89
6. ASSUMPTIONS AND LIMITATIONS .....	89
6.1 Performance .....	90
6.2 Assumed Sensor Performance .....	90
6.3 Pre-Planned Product Improvement.....	90

6.1.1. Improvement 1 .....	90
6.1.2. Improvement 2 .....	90
7. REFERENCES .....	92

## LIST OF TABLES

<i>Table 1. JPSS mission requirements for Suspended Matter product.....</i>	<i>12</i>
<i>Table 2. Output flags for JPSS ADP product .....</i>	<i>14</i>
<i>Table 3. Quality flags for JPSS ADP product.....</i>	<i>14</i>
<i>Table 4. Product quality information flags for JPSS ADP product.....</i>	<i>14</i>
<i>Table 5. Outputs from JPSS ADP product.....</i>	<i>15</i>
<i>Table 6. Channel numbers and wavelengths for the VIIRS. Channels used in the ADP product algorithm are highlighted in different colors. Key channels are identified by a check mark. ....</i>	<i>16</i>
<i>Table 7 Mapping of channels for different sensors to channels used in ADP Enterprise System algorithm .....</i>	<i>17</i>
<i>Table 8 ADP product primary sensor input data.....</i>	<i>20</i>
<i>Table 9 JPSS VIIRS Product Precedence and Ancillary input data.....</i>	<i>21</i>
<i>Table 10 VIIRS ADP product cloud mask tests to VIIRS cloud mask tests.....</i>	<i>22</i>
<i>Table 11 Mapping of ADP cloud tests with different cloud mask product .....</i>	<i>23</i>
<i>Table 12 JPSS ADP algorithm output summary.....</i>	<i>68</i>
<i>Table 13 Accuracy, Probability of True Positive Detection, and Probability of False Positive Detection of JPSS ADP product for Dust detection over AERONET Stations.....</i>	<i>84</i>
<i>Table 14 Accuracy, Probability of True Positive Detection, and Probability of False Positive Detection of JPSS ADP product for smoke detection over AERONET Stations .....</i>	<i>84</i>
<i>Table 15 Ensemble Accuracy, Probability of True Positive Detection, and Probability of False Positive Detection of JPSS ADP product for smoke and dust detection .....</i>	<i>85</i>
<i>Table 16. Accuracy, Probability of True Positive Detection, and Probability of False Positive Detection of JPSS ADP product for smoke and dust detection over land.....</i>	<i>86</i>
<i>Table 17. Accuracy, Probability of True Positive Detection, and Probability of False Positive Detection of JPSS ADP product for smoke and detection over water .....</i>	<i>86</i>

---

## LIST OF FIGURES

<i>Figure 1: High level flowchart of the ADP product algorithm, illustrating the main processing sections.</i>	19
<i>Figure 2: Real and imaginary part of dust, soot, water and ice as a function of wavelength. Plots are based on data obtained from CRTM.</i>	25
<i>Figure 3. Combined tri-spectral diagram of brightness temperature differences for ‘heavy dust’ pixels, indicated by the number 1 to 7, and for clear sky. From Darmenov and Sokolik [2005].</i>	28
<i>Figure 4: The relationship between various combinations of channels for heavy, thin dust, and clear conditions.</i>	29
<i>Figure 5: Ratio of the simulated TOA reflectance at MODIS band 8 (412 nm) and band 9 (440 nm) as a function of viewing zenith angle at a solar zenith angle of 10° (a), 30° (b) and 50° (c). Solid lines represent a clear atmosphere bounded by ocean (blue), vegetation (green), and desert (orange). Dashed lines represent an atmosphere with dust (AOD at 550 nm is 1.0) bounded by ocean (blue), vegetation (green) and desert (orange). Red solid lines are sunglint angle over ocean. Relative azimuth angle of 120° is used. Total ozone amount is set at 350 DU.</i>	31
<i>Figure 6: (a) RGB image of MODIS Aqua Granule on May 3, 2012, 1425 UTC; (b) RGB image of MODIS Aqua granule on June 23, 2012, 1320 UTC; Ratio of the observed TOA reflectance at MODIS band 8 (412 nm) and band 9 (440 nm) as a function of the observed TOA reflectance at MODIS band 8 (412 nm) for pixels identified as clear (blue) and dust-laden (orange) over land (c) and over ocean (d).</i>	33
<i>Figure 7: AAI as a function of viewing zenith angle over desert (a), over ocean (b) and over vegetation (c), for aerosol optical depth at 550 nm (<math>\tau</math>) of 0.0 (square), 0.5 (triangle), 1.0(circle) and 2.0(diamond). Solar Zenith Angle (SZA) of 10°, 30° and 50° is represented by dash-dotted, solid and dotted lines, respectively. Note that relative azimuth is set at 120°.</i>	34
<i>Figure 8: Ratio of the observed TOA reflectance at: a) MODIS band 8 (412 nm) and band 9 (440 nm), b) MODIS band 8 (412 nm) and band 7 (2130 nm), as a function of the observed TOA reflectance at MODIS band 8 (412 nm) for pixels identified as clear (blue), smoke-laden (red) and dust-laden (orange) over ocean.</i>	35
<i>Figure 9: Surface reflectance at M5( 0.67<math>\mu</math>m) vs. surface reflectance at M11(2.25<math>\mu</math>m) from S-NPP VIIRS.</i>	37
<i>Figure 10: Scatter plots of the ratio of <math>R_{0.47}</math> to <math>R_{1.61}</math> vs. <math>R_{0.47\mu m}</math>, the ratio of <math>R_{0.47}</math> to <math>R_{1.61}</math> vs. <math>R_{1.61\mu m}</math>, the ratio of <math>R_{2.25}</math> to <math>R_{1.61}</math> vs. <math>R_{0.47\mu m}</math>, the ratio of <math>R_{2.25}</math> to <math>R_{1.61}</math> vs. <math>R_{1.61\mu m}</math> for clear-sky pixels (blue), thick smoke pixels (dark brown), thin smoke (light brown) and cloudy pixels (red).</i>	38
<i>Figure 11: Detail Flow chart of dust detection over land.</i>	42
<i>Figure 12: Detail Flow chart of dust detection over land.</i>	44
<i>Figure 13: Top: a red-green-blue (RGB) false color image of S-NPP observation data on September 14, 2013 at approximate 20:20 UTC. Bottom: the results of the dust detection where pixels flagged as dusty are colored as yellow to brown, scaled by DAI.</i>	47
<i>Figure 14: Top: a red-green-blue (RGB) false color image of S-NPP observation data on December 14, 2013 at approximate 19:55 UTC. Bottom: the results of JPSS ADP algorithm where pixels flagged as dusty are colored as yellow to brown, scaled by DAI; pixels flagged as smoke are colored as pink to red, scaled by SAI.</i>	48
<i>Figure 15: Detailed flow chart of IR-visible based dust detection over water.</i>	49
<i>Figure 16: Detailed flow chart of deep-blue dust detection over water.</i>	50

Figure 17: S-NPP VIIRS observations on Feb 1, 2015 at approximate 11:25 to 11:28 UTC. A dust outbreak is flowing from the Sahara desert over the adjacent Mediterranean Ocean. .... 55

Figure 18: Detailed flow chart of IR-Visible based smoke detection over land..... 56

Figure 19: Detailed flow chart of deep-blue smoke detection over land ..... 58

Figure 20: Top: a red-green-blue (RGB) false color image of S-NPP VIIRS observation data on August 3, 2014 at approximate 20:10 UTC. Bottom: the results of the smoke detection where pixels flagged as smoky are pink to red. .... 61

Figure 21: Detailed flow chart of Visible-NIR based smoke detection over water. .... 62

Figure 22: Detailed flow chart of deep-blue smoke detection over water. .... 63

Figure 23: Top: a red-green-blue (RGB) false color image of S-NPP VIIRS observations on July 11, 2015 at approximate 12:58 UTC. Bottom: the results of ADP product algorithm. .... 68

Figure 24 : Top: histogram of Angstrom Exponent (AE) for pixels with smoke and haze in S-NPP VIIRS observations. Bottom: histogram of Angstrom Exponent (AE) for smoke, dust and haze from AERONET observations. .... 72

Figure 25: Schematic illustration of matchups between S-NPP VIIRS and CALISPO-VFM product. .... 73

Figure 26: TOP: S-NPP VIIRS RGB Image on April 5, 2015 at about 09:59 UTC. Middle: the results of the dust detection from JPSS ADP product. Bottom: S-NPP VIIRS AOD (only pixels with AOD > 0.2 are shown) ..... 75

Figure 27: Comparison of dust detected (orange) using VIIRS ADP product algorithm with CALIPSO Vertical Feature Mask (VFM) on January 30, 2013, UTC 14:33. a) RGB image, b) Aerosol Optical depth from S-NPP VIIRS aerosol Product, c) Dust mask from ADP product, d) Dust (orange) on CALIPSO track, e) Dust (orange) detected with VIIRS ADP product algorithm on CALIPSO track, f) Dust vertical distribution on the part of CALIPSO track collocated with VIIRS ADP product, g) Dust from VIIRS ADP product on the same part of track as in b. .... 77

Figure 28: Comparison of dust detected (orange) using JPSS ADP product algorithm with dust (orange) in CALIPSO Vertical Feature Mask (VFM) on June 30, 2015 at UTC 11:25. a) S-NPP VIIRS RGB image, b) Smoke/dust mask from JPSS ADP product, c) Dust (orange) on CALIPSO track, d) Dust (orange) detected with JPSS ADP product algorithm on CALIPSO track, e) Dust vertical distribution on the part of CALIPSO track collocated with JPSS ADP product, f) Dust from VIIRS ADP product on the same part of track as in b. .... 79

Figure 29: Left: S-NPP VIIRS RGB Image on June 29, 2015 over North America. Right: the results of the smoke detection (pixels flagged as smoky are in colored red) from JPSS ADP product... 80

Figure 30: Comparison of smoke detected (red) using VIIRS ADP product algorithm with smoke in CALIPSO Vertical Feature Mask (VFM) on July 25, 2006, UTC 05:15. a. RGB image b. Aerosol Optical depth from MODIS C5 aerosol Product. C. Smoke (red) on CALIPSO track. d. Smoke detected with VIIRS ADP product algorithm on CALIPSO track. e. Smoke vertical distribution on the part of CALIPSO track collocated with VIIRS ADP product d. smoke from VIIRS ADP product on the same part of track as in b. .... 81

Figure 31: Comparison of smoke detected (red) using VIIRS ADP product algorithm with smoke in CALIPSO Vertical Feature Mask (VFM) on October 2, 2007 at 17:50 UTC. a) RGB image, b) Aerosol Optical depth from MODIS C5 aerosol Product, c) Smoke (red) on CALIPSO track, d) Smoke detected with VIIRS ADP product algorithm on CALIPSO track, e) Smoke vertical distribution on the part of CALIPSO track collocated with VIIRS ADP product, d) smoke from VIIRS ADP product on the same part of track as in b. .... 82

*Figure 32: Comparison of offline run with framework run for S-NPP VIIRS observation on August 3, 2014, UTC13:20. a) smoke/dust mask from framework run, b) smoke/dust mask from offline run. .... 87*

*Figure 33: Comparison of offline run with framework run form S-NPP VIIRS observation on February 13, 2014, UTC 03:25. a) smoke/dust mask from framework run, b) smoke/dust mask from offline run. .... 87*

*Figure 34: Global smoke/dust mask from ADP product algorithm run in the framework for S-NPP VIIRS observations. a) July 15, 2014, b) July 16, 2014. Absorbing Aerosol Indexes from OMPS for these two days are also shown in c) and d). .... 88*

## LIST OF ACRONYMS

Acronym	Description
AERONET	<b>A</b> erosol <b>R</b> obotic <b>N</b> ETwork
AIT	Algorithm Integration Team
ADP	Aerosol Detection Product
AOD	Aerosol Optical Depth
ATBD	Algorithm Theoretical Basis Document
ATIP	Algorithm and Test Implementation Plan
AVHRR	Advanced Very High Resolution Radiometer
AWG	Algorithm Working Group
CALIPSO	Cloud-Aerosol Lidar and Infrared Pathfinder Satellite Observation
CONUS	CONTiguous United States
BT	Brightness Temperature
BTD	Brightness Temperature Difference
FMW	Fine Mode Weight
HMS	Hazard Mapping System
IMS	Interactive Multisensor Snow and Ice Mapping System
JPSS	Joint Polar Satellite System
MeanR	Mean of reflectance (in a box of 3 X 3 pixels)
MODIS	Moderate Resolution Imaging Spectroradiometer
MRD	Mission Requirements Document
NDVI	Normalized Difference Vegetation Index
NOAA	National Atmospheric and Atmospheric Administration
R	Reflectance
RTM	Radiative Transfer Model
SM	Suspended Matter
SST	Sea Surface Temperature
StdR	Standard Deviation of Reflectance (in a box of 3 X 3 pixels)
NPP	National Polar-orbiting Operational Environmental Satellite System Preparatory Project
TOA	Top of the Atmosphere
VFM	Vertical Feature Mask
VIIRS	Visible Infrared Imaging Radiometer Suite



## **ABSTRACT**

This document describes the algorithm for Aerosol Detection(ADP) (including smoke/dust detection) Product over land and water from the multispectral reflectance measurements observed by the Visible Infrared Imaging Radiometer Suite (VIIRS) onboard JPSS. It includes the description of theoretical basis, physics of the problem, validation of the product, and assumptions and limitations.

Episodic events, such as smoke and dust outbreaks, impact human health and economy. Therefore, it is desirable to have information on the time, location and coverage of these outbreaks for the monitoring and forecasting of air quality. JPSS VIIRS is designed to observe the globe with a spatial resolution of 750m at nadir in the visible, near-IR, and IR bands respectively. Taking advantage of the unique capability of JPSS VIIRS, ADP product will be produced with an algorithm designed to take advantage of various spectral measurements.

Aerosol detection algorithm is based on the fact that smoke/dust exhibits features of spectral dependence and contrast over both visible and infrared spectrum that are different from clouds, surface, and clear-sky atmosphere. The fundamental principle of the detection algorithm depends on threshold tests which separate smoke/dust from cloud and clear-sky over water and land.

By using Suomi National Polar-orbiting Operational Environmental Satellite System Preparatory Project (NPP) VIIRS observations as proxy, JPSS VIIRS ADP product algorithm has been tested for different scenarios such as wild fires, dust storms, and dust transport from Africa. Comparisons with RGB images, AERONET observations and other satellite products such as CALIPSO have been performed. In general, the requirement, i.e., 80% correct detection for dust over water and land, for smoke over land, and 70% correct detection for smoke over water, can be achieved.

# 1 INTRODUCTION

Aerosols perturb the Earth's energy budget by scattering and absorbing radiation and by altering cloud properties and lifetimes. They also exert large influences on weather, air quality, hydrological cycles, and ecosystems. Aerosols released into the atmosphere due to natural and anthropogenic activities lead to deteriorated air quality and affect Earth's climate. It is important to regularly monitor the global aerosol distributions and study how they are changing, especially for those aerosols with large spatial and temporal variability, such as smoke, sand storms, and dust [IPCC, 2007]. Detection of these highly variable aerosols is challenging because of strong interactions with local surface and meteorological conditions.

Because atmospheric aerosols can directly alter solar and Earth radiation in both visible and infrared (IR) spectral regions through scattering and absorption processes, both visible, including deep-blue, and IR remote sensing techniques have been used for detection of aerosols in the atmosphere [e.g., Tanre and Legrand, 1991; Ackerman 1989, 1997; Kaufman et al., 1997; Verge-Depre et al., 2006; Ciren and Kondragunta, 2014]. Visible and IR images can be used for detecting episodic smoke and dust particles due to the fact that these aerosol particles display their distinctive spectral variations in the visible and IR spectral regions different from those of cloud or clear-sky conditions. In practice, the detection is based on the analysis of reflectance (or radiance) in visible bands or brightness temperature (BT) in IR bands. The magnitude of the difference in reflectance or BTs in selected bands (or channels) can be used to infer the signature of dust and smoke. This is the basic idea of our aerosol detection algorithm, which will be described in detail in this document.

## 1.1 *Purpose of This Document*

The aerosol detection Algorithm Theoretical Basis Document (ATBD) provides a high level description of and the physical basis for the detection of smoke/dust contaminated pixels with images taken by the VIIRS flown on the JPSS series of next generation NOAA operational polar meteorological satellites. The algorithm provides an initial estimate of the presence or absence of smoke or dust within each VIIRS pixel.

## 1.2 *Who Should Use This Document*

The intended users of this document are those interested in understanding the physical basis of the algorithms and how to use the output of this algorithm to optimize the episodic aerosol detection for a particular application. This document also provides information useful to anyone maintaining or modifying the original algorithm.

## 1.3 *Inside Each Section*

This document is broken down into the following main sections.

- **System Overview:** Provides relevant details on VIIRS instrument characteristics and detailed description of the products generated by the algorithm.
- **Algorithm Description:** Provides the detailed description of the algorithm including physical basis, the required input and the derived output. Examples from algorithm processing using proxy input data are also provided.

- **Test Data Sets and Outputs:** Provides a description of the test data sets used to characterize the performance of the algorithm and the quality of the output. Precision and accuracy of the end product is estimated and Error budget is calculated.
- **Practical Considerations:** Provides an overview of the issues involving numerical computation, programming and procedures, quality assessment and diagnostics and exception handling.
- **Assumptions and Limitations:** Provides an overview of assumptions which the algorithm is based on and the current limitations of the approach. The plan for overcoming some limitations with further algorithm development is also given.

## 1.4 *Related Documents*

Besides the references given throughout, this document is related to documents listed as bellow:

- (1) JPSS Suspended Matter product Algorithm Theoretical Basis Document (ATBD)
- (2) JPSS Program Level 1 Requirements Document (L1RD)
- (3) JPSS Program Level 1 Requirements Document SUPPLEMENT (L1RDS)
- (4) JPSS VIIRS Aerosol Detection Product Validation Plan Document

## 1.5 *Revision History*

This is the second version (Version 1.1) of this document. All the documents were created by the JPSS Risk Reduction ADP product team led by Dr. Shobha Kondragunta of NOAA/NESDIS/STAR. The ADP product team includes Dr. Pubu Ciren of IMSG, Inc., Maryland. Version 1.1 ATBD accompanies the delivery of the version 1.1 algorithm to the JPSS Risk Reduction Algorithm Integration Team (AIT). Version 1.1 is an update on Version 1.0 to include the detailed description on the Enterprise System of the JPSS Risk Reduction algorithm as described in Version 1.0 and also some corrections.

# 2 **OBSERVING SYSTEM OVERVIEW**

This section will describe the products generated by the JPSS ADP product algorithm including smoke and dust and the requirements it places on the sensor.

## 2.1 *Products Generated*

As described in Table 1 ADP product measurement accuracy is defined as 80% of correct classification for dust over water and land, for smoke over land, and 70% correct classification for smoke over water with measurement range given as binary yes/no detection above threshold of 0.2 aerosol optical depth, as stated in JPSS Program Level 1 Requirements Document (L1RD) and JPSS Program Level 1 Requirements SUPPLEMENT (L1RDS). It should be noted that aerosol optical depth of 0.2 defines background atmospheric aerosol and is not computed within this algorithm.

**Table 1. JPSS mission requirements for Suspended Matter product**

EDR Attribute	Threshold	Objective
SM Applicable Conditions: 1. SM includes dust, volcanic ash, and smoke at any altitude. 2. Clear, for AOT greater than 0.2 daytime only.		
a. Horizontal Cell Size	3 km	1 km
b. Vertical Cell Size	Total Column	0.2 km
c. Mapping Uncertainty, 3 Sigma	3 km	0.1 km
d. Measurement Range		
1. Detect suspended matter (dust, smoke, volcanic ash) (1)(2)	Type: dust, volcanic ash, smoke	Dust, ash, smoke, sea salt
2. Radioactive/smoke plumes	0 to 150 $\mu\text{g}/\text{m}^3$ (smoke)	0 to 200 $\mu\text{g}/\text{m}^3$ (smoke)
e. Probability of Correct Typing		
1. Suspended Matter	80%	100%
2. Dust	80%	100%
3. Smoke	70%	100%
4. Volcanic Ash	60%	100%
5. Mixed Aerosol (2)		80%
f. Refresh	At least 90% coverage (product retrieval is attempted regardless of sky condition) of the globe over 24 hours (monthly average)	3 hrs
<b>Notes:</b>		
<ol style="list-style-type: none"> <li>The dust and volcanic ash categories were combined at the request of M. Pavalonis and supported by J. Gleason and H. Kilcoyne. The current algorithm cannot distinguish between dust and volcanic ash and the intent of the EDR was to say that there was “something” in the atmosphere. The dust and volcanic ash are separated into two categories in this revision. Although some dust may be falsely identified as ash by the volcanic ash algorithm, the suspended matter algorithm will identify dust explicitly.</li> <li>DOC has a responsibility for analyzing areas of volcanic ash, blowing dust, and smoke. There is therefore a requirement that the suspended matter algorithm identifies instances of multiple types of suspended matter at the same location and not merely provides a</li> </ol>		

single suspended matter type with the highest concentration or probability.

*This requirement table is currently being modified to map the products between GOES-R VIIRS and JPSS VIIRS for the Enterprise algorithm approach. Volcanic ash product will be moved to a separate table in the JPSS requirement document and also the smoke concentration will be changed to column smoke concentration in units of  $\mu\text{g}/\text{m}^2$ . When the revised table is approved, it will be updated in this document.*

The purpose of the ADP product algorithm is to identify VIIRS pixels which are contaminated by either smoke or dust during daytime to facilitate the monitoring of occurrences and development of smoke/dust episodes. However, due to the relatively weak contribution of aerosols compared to reflection from the surface to the satellite measured reflectances/brightness temperatures, the ADP product algorithm performs better for heavy smoke /dust episodes (with aerosol optical depth  $>0.2$ ) over dark surface than over bright surfaces. Smoke detection over semi-arid and arid regions is less accurate due to lower contrast with the background. The algorithm output is currently written in netCDF4 format for Volcanic Ash flag (1/0 for yes/no, passed down from VCM product), dust flag (1/0 for yes/no), smoke flag (1/0 for yes/no), cloud flag (1/0 for yes/no), none/unknown/clear flag (1/0 for yes/no), and snow/ice flag (1/0 for yes/no) (see Table 2) and 4 quality flags (contained in a 1 byte integer), i.e., smoke detection quality flag (10/01/11 for low/medium/high quality), Dust detection quality flag (10/01/11 for low/medium/high quality), volcanic ash quality flag (10/01/11 for lower/medium/high quality) and none/unknown/clear quality flag (10/01/11 for low/medium/high confidence). In addition, product quality information flags (contained in a 4 byte integer) are also generated but only as internal output. The details on both quality flags and product quality information flags are given in Table 3 and Table 4 respectively. And, details on determination of quality flags are given in section 3.4.2.2.3., section 3.4.2.3.3., section 3.4.2.4.3. and section 3.4.2.5.3.. In addition, scaled smoke/dust aerosol index, which is related to the intensity of smoke/dust event, non-dust aerosol index and smoke concentration in a unit of  $\mu\text{g}/\text{m}^3$  are also provided in the output and are given in Table 5.

## 2.2 Instrument Characteristics

The ADP product will be produced for each pixel observed by the VIIRS. Table 6 summarizes the channels used by the current ADP product algorithm. Note that, the ADP algorithm is designed as Enterprise System, which means the ADP algorithm is able to handle multi-spectral observations from sensors which cover wavelength range from deep-blue to IR, such as VIIRS and MODIS, or from Visible to IR, such as AHI and ABI. In the following sections, VIIRS will be mainly used as an example. However, the mapping of channels or bands from different sensors to the channels used in enterprise system algorithm is given in Table 7.

The backbone of the ADP product algorithm is the distinctive spectral and spatial signature of aerosol (smoke/dust). Like any other threshold-based algorithm, the ADP product algorithm requires optimal performance of the instrument. First, the ADP product algorithm is designed to work when only a subset of the expected channels are available. Missing channels, especially the crucial ones, will impact directly the performance of the algorithm. Second, the ADP product algorithm is sensitive to instrument noise and calibration error. Thresholds are required to be adjusted accordingly to the status of instrument

operation and performance. Third, calibrated observations are also critical, but since the algorithm does not compare the observed values to those from a forward radiative transfer model, uncertainties in calibration can be ameliorated by modifying thresholds post launch of the JPSS VIIRS. The channel specifications for VIIRA are given in the MRD.

**Table 2. Output flags for JPSS ADP product**

Type/Byte	Flag Name	Meaning		
		Value: 0 (default)	1	
Integer	1	Volcanic Ash	No	yes
	2	Cloud	No	yes
	3	Dust	No	yes
	4	Smoke	No	yes
	5	None/Unknown/Clear	No	yes
	6	Snow/ice	No	yes

**Table 3. Quality flags for JPSS ADP product**

Byte/Bit*	Quality Flag Name	Meaning			
		2bit: 10 (default:00)	01	11	
1	0-1	QC_ASH_DETECTION	Low	Medium	High
	2-3	QC_SMOKE_DETECTION	Low	Medium	High
	4-5	QC_DUST_CONFIDENCE	Low	Medium	High
	6-7	QC_NUC_CONFIDENCE	Low	Medium	High

\*Start from the least significant bit

**Table 4. Product quality information flags for JPSS ADP product**

Byte/Bit*	Diagnostic Flag Name	Meaning			
		1bit: 0 (default)	1		
		2bit: 00 (default)	01	11	
2	0	QC_INPUT_LON	valid longitude	Invalid longitude 180<longitude or longitude <-180	
	1	QC_INPUT_LAT	valid latitude	Invalid latitude 90<latitude or latitude <-90	
	2-3	QC_INPUT_SOLZEN	Valid solar zenith angle (SZA) 0≤SZA≤90	invalid solar zenith angle(SZA) 90<SZA or SZA <0	90≥Solar zenith angle >60
	4-5	QC_INPUT_SATZEN	Valid local zenith angle(VZA) 0≤VZA≤90	invalid local zenith angle(VZA) 90<VZA or VZA <0	90≥Local zenith angle >60

	6-7	QC_INPUT_SNOW/ICE_SOURCE	Snow/ice Mask from VIIRS retrieval	Snow/ice Mask from IMS	Snow/ice Mask from Internal test
3	8	QC_INPUT_SUNGLINT_SOURCE	VIIRS sun glint Mask (from Cloud Mask product)	Internal sun glint Mask	
	9	QC_INPUT_SUNGLINT	outside of sun glint	within sun glint	
	10	QC_INPUT_LAND/WATER	Water	Land	
	11	QC_INPUT_DAY/NIGHT	Day	Night	
	12	QC_WATER_SMOKE_INPUT	Valid VIIRS inputs	invalid VIIRS inputs	
	13	QC_WATER_SMOKE_CLOUD	Cloud-free	Obscured by clouds	
	14	QC_WATER_SMOKE_SNOW/ICE	Snow/ice free	With snow/ice	
	15	QC_WATER_SMOKE_TYPE	Thin Smoke	Thick Smoke	
4	16	QC_WATER_DUST_INPUT	Valid VIIRS inputs	Invalid VIIRS inputs	
	17	QC_WATER_DUST_CLOUD	Cloud-free	Obscured by clouds	
	18	QC_WATER_DUST_SNOW/ICE	Snow/ice free	With snow/ice	
	19	QC_WATER_DUST_TYPE	Thin dust	Thick dust	
	20	QC_LAND_SMOKE_INPUT	Invalid VIIRS inputs	Valid VIIRS inputs	
	21	QC_LAND_SMOKE_CLOUD	Cloud-free	Obscured by clouds	
	22	QC_LAND_SMOKE_SNOW/ICE	Snow/ice free	With snow/ice	
5	23	QC_LAND_SMOKE_TYPE	fire	Thick smoke	
	24	QC_LAND_DUST_INPUT	Valid VIIRS inputs	Invalid VIIRS inputs	
	25	QC_LAND_DUST_CLOUD	Cloud-free	Obscured by clouds	
	26	QC_LAND_DUST_SNOW/ICE	Snow/ice free	With snow/ice	
	27	QC_LAND_DUST_TYPE	Thin dust	Thick dust	
	28-29	Smoke_Detection_Algorithm_Path	Deep-blue based algorithm	IR-Visible based algorithm	Both
30-31	Dust_Detection_Algorithm_Path	Deep-blue based algorithm	IR-Visible based algorithm	Both	


\*Start from the least significant bit

**Table 5. Outputs from JPSS ADP product**

Bytes	Type	Name	Meaning
4	Float 32	Smoke/Dust aerosol index	Index scaled by the corresponding threshold to illustrate the intensity of smoke/dust event
4	Float 32	Dust Smoke Discrimination Index	an index used to separate smoke from dust
4	Float32	Smoke concentration	in a unit of $\mu\text{g}/\text{m}^3$ to describe mass concentration from smoke

**Table 6. Channel numbers and wavelengths for the VIIRS. Channels used in the ADP product algorithm are highlighted in different colors. Key channels are identified by a check mark.**

Band Name	Nominal Wavelength Range (μm)	Nominal Central Wavelength (μm)	Horizontal Sample Interval (Km) (Along-Track×Along-Scan)		Sample Use
			Nadir	End of Scan	
M1	0.402-0.422	0.412	0.742×0.259	1.60×1.58	Dust/Smoke
M2	0.436-0.454	0.445	0.742×0.259	1.60×1.58	Dust/smoke
M3	0.478-0.498	0.488	0.742×0.259	1.60×1.58	Dust/Smoke
M4	0.545-0.565	0.555	0.742×0.259	1.60×1.58	Smoke
M5	0.662-0.682	0.640	0.742×0.259	1.60×1.58	Dust/Smoke
M6	0.739 – 0.754	0.746	0.742×0.776	1.60×1.58	Smoke
M7	0.846-0.885	0.865	0.742×0.259	1.60×1.58	Dust/Smoke
M8	1.230-1.250	1.24	0.742×0.776	1.60×1.58	Dust/Smoke
M9	1.371-1.386	1.378	0.742×0.776	1.60×1.58	Dust
M10	1.580-1.640	1.61	0.742×0.776	1.60×1.58	Smoke
M11	2.225-2.275	2.25	0.742×0.776	1.60×1.58	Dust/Smoke
M12	3.660-3.840	3.70	0.742×0.776	1.60×1.58	Dust/Smoke
M13	3.973-4.128	4.05	0.742×0.259	1.60×1.58	Smoke
M14	8.400-8.700	8.55	0.742×0.776	1.60×1.58	
M15	10.263-11.263	10.763	0.742×0.776	1.60×1.58	Dust/Smoke
M16	11.538-12.488	12.013	0.742×0.776	1.60×1.58	Dust

 Input for both  
Dust and smoke

 Input for smoke

 Input for dust



**Table 7 Mapping of channels for different sensors to channels used in ADP Enterprise System algorithm**

Channel In EPS		Sensors			
		VIIRS	MODIS	ABI	AHI
1	0.412µm	M1	Band 8	X	X
2	0.445 µm	M2	Band 9	X	X
3	0.488 µm	M3	Band 3	Band 1	Band1
4	0.555 µm	M4	Band 4	X	x
5	0.640 µm	M5	Band 1	Band 2	Band3
6	0.746 µm	M6	Band 15	X	X
7	0.865 µm	M7	Band 2	Band 3	Band 4
8	1.24 µm	M8	Band 5	X	X
9	1.38 µm	M9	Band 26	Band 4	X (Band 5)*
10	1.61 µm	M10	Band 6	Band 5	Band 5
11	2.25 µm	M11	Band 7	Band 6	Band 6
12	3.70 µm	M12	Band 20	X(Band 7)*	X(Band 7)*
13	4.05 µm	M13	Band 21	Band 7	Band 7
15	10.7 µm	M15	Band 31	Band 14	Band 14
15	12.01 µm	M16	Band 32	Band 15	Band 15

**Green:** used by both deep-blue based and IR-visible based detection algorithms

**Blue:** only used by deep-blue based detection algorithm

**Brown:** only used by IR-Visible based detection algorithm.

**\*:** band is missing but using the corresponding band in the parentheses instead.

**X:** channel is missing, but not needed, and filled with “-999.9”

## 3 ALGORITHM DESCRIPTION

### 3.1 *Algorithm Overview*

The ADP product serves to aid air quality forecasters in identifying smoke and dust laden atmosphere. The ADP product algorithm follows heritage algorithms:

- Non-cloud obstruction (including smoke and dust) detection in the MOD/MYD35 MODIS cloud mask developed for MODIS by the University of Wisconsin (UW).
- Operational dust detection from MODIS developed for NWS and run by NESDIS/OSOPO.

The fundamental outputs of the ADP product consist of 10 flags. They are 6 type flags, respectively for the presence of volcanic ash, smoke, dust, none/unknown/clear, clouds and snow/ice, and 4 quality flags, respectively for volcanic ash flag, smoke flag, dust flag and none/unknown/clear flag. Type flag has a value of 0 for the presence and 1 for the absence. As an example, in the smoke/dust flag, 1 represents smoke/dust and 0 represents no smoke/dust, respectively. The details on quality flags are given in section 2.1. The following sections describe the JPSS VIIRS ADP product algorithm.

### 3.2 *Processing Outline*

The processing outline of the ADP product algorithm is summarized in Figure 1, which includes the basic modules as input, output, and detection over land and water. The algorithm is written in C++, and products are outputted in netCDF4 format. For optimizing CPU usage, the ADP product algorithm is designed to run on segments of data. Each segment is comprised of multiple scan lines (12 lines). This Enterprise algorithm is able to run through three paths, they are IR-visible based detection algorithm, defined as path **1**, deep-blue based detection algorithm, defined as path **2**, and combined IR-Visible based and deep-based detection algorithms, defined as Path **3**. The algorithm path is supplied or determined by spectral coverage of the input data. The algorithm path taken to generate the product is outputted in the product quality information flags (see Table 4, byte 5), respectively for the detected smoke and dust.

**Figure 1: High level flowchart of the ADP product algorithm, illustrating the main processing sections.**

### **3.3 *Algorithm Input***

This section describes the input needed to process the ADP product algorithm. While the ADP product is derived for each pixel, it does require knowledge of the surrounding pixels. In its current operation, we run the ADP product algorithm on segments of 12 scan-lines.

#### **3.3.1 Primary Sensor Data**

Calibrated/Navigated VIIRS reflectances and brightness temperatures on selected channels, geolocation (latitude/longitude) information, and VIIRS sensor quality flags are used as the sensor input data for the algorithm. Table 8 contains the primary sensor data used by the ADP product algorithm. Note that, the cloud mask required in ADP product algorithm is designed to primarily come from JPSS VIIRS cloud product. Channels used to determine the cloud mask are not listed here as that information is part of the VIIRS cloud mask ATBD.

**Table 8 ADP product primary sensor input data.**

Name	Type	Description	Dimension
M1 reflectance	input	Calibrated VIIRS level 1b reflectance at M 1	grid (xsize, ysize)
M2 reflectance	input	Calibrated VIIRS level 1b reflectance at M 2	grid (xsize, ysize)
M3 reflectance	input	Calibrated VIIRS level 1b reflectance at M 3	grid (xsize, ysize)
M4 reflectance	input	Calibrated VIIRS level 1b reflectance at M 4	grid (xsize, ysize)
M5 reflectance	input	Calibrated VIIRS level 1b reflectance at M 5	grid (xsize, ysize)
M6 reflectance	input	Calibrated VIIRS level 1b reflectance at M 6	grid (xsize, ysize)
M7 reflectance	input	Calibrated VIIRS level 1b reflectance at M 7	grid (xsize, ysize)
M8 reflectance	input	Calibrated VIIRS level 1b reflectance at M 8	grid (xsize, ysize)
M9 reflectance	input	Calibrated VIIRS level 1b reflectance at M 9	grid (xsize, ysize)
M10 reflectance	input	Calibrated VIIRS level 1b reflectance at M 10	grid (xsize, ysize)
M11 reflectance	input	Calibrated VIIRS level 1b reflectance at M 11	grid (xsize, ysize)
M12 brightness temperature	input	Calibrated VIIRS level 1b brightness temperature at M12	grid (xsize, ysize)
M 13 brightness temperature	input	Calibrated VIIRS level 1b brightness temperature at M13	grid (xsize, ysize)
M15 brightness temperature	input	Calibrated VIIRS level 1b brightness temperature at M15	grid (xsize, ysize)
M16 brightness temperature	input	Calibrated VIIRS level 1b brightness temperature at M16	grid (xsize, ysize)
Solar zenith angle	input	Pixel solar zenith angle	grid (xsize, ysize)
Solar azimuth angle	input	Pixel solar azimuth angle	grid (xsize, ysize)
Satellite zenith angle	input	Pixel satellite zenith angle	grid (xsize, ysize)
Satellite azimuth angle	input	Pixel satellite azimuth angle	grid (xsize, ysize)
Latitude	input	Pixel latitude	grid (xsize, ysize)
Longitude	input	Pixel longitude	grid (xsize, ysize)
QC flags	input	VIIRS quality control flags with level 1b data	grid (xsize, ysize)

### 3.3.2 VIIRS Product Precedence and Ancillary Data

The dynamic data are from both VIIRS Level-1b and Level-2 products that needed by the ADP product algorithm and are listed in Table 9. They include cloud mask from VIIRS cloud product, snow/ice mask from VIIRS level-2 product. Sun glint mask and day/night flag are determined internally in the ADP product algorithm from viewing and illuminating geometry information.

- **Snow/Ice mask**

Primary source of snow/ice is VIIRS Level-2 Snow/Ice Product. However, under the situation that the primary source is missing, Interactive Multisensor Snow and Ice Mapping System (IMS) (<http://nsidc.org/data/g02156.html>) snow/ice mask will be the secondary source. In addition, the ADP product algorithm has internal snow/ice test over land, whose function is to eliminate the residuals from external snow/ice mask over land. It is applied after the primary/secondary snow/ice mask. Details on the internal snow/ice mask are given in section 3.4.2.1.

- **Cloud mask**

The purpose of using cloud mask in the ADP product algorithm is to eliminate pixels with obvious clouds, such as high and ice cloud, before performing smoke/dust detection. Hence, the requirement of ADP product algorithm for cloud mask is more specific than just cloud or clear mask. Stringent cloud mask has the potential to classify smoke/ dust as cloud, while loose cloud mask increases the chance of misidentifying clouds as smoke/dust. The ADP product algorithm intends to use only individual tests in JPSS VIIRS cloud mask product which indicate the existence of high cloud, ice cloud and thin cirrus cloud. In addition, some tests in cloud mask product, such as cloud shadow and fire hot spot, are used as quality control for the detected smoke/dust in ADP product. And, flag for volcanic ash from JPSS L-2 Volcanic ash product is used to set volcanic ash flag in ADP product output. Currently, the ADP product algorithm is using Suomi NPP VIIRS data as proxy, including NPP VIIRS Cloud Mask (VCM). Based on the definition of individual tests from VCM, the individual tests used in JPSS ADP product algorithm are given in Table 10. Table 11 gives mapping of JPSS ADP cloud test to individual tests in other cloud mask products, such as JPSS VIIRS cloud mask (i.e., Bayesian cloud mask) and MODIS cloud mask.

**Table 9 JPSS VIIRS Product Precedence and Ancillary input data.**

	Name	Type	Source	Dimension
VIIRS Product Precedence Data	Cloud mask	input	JPSS VIIRS level 2 cloud product	grid(xsize, ysize)
	Snow/Ice mask	input	JPSS VIIRS level 2 Snow/Ice Product	grid(xsize, ysize)
	Volcanic ash	input	JPSS VIIRS level 2 Volcanic ash Product	grid(xsize, ysize)
	Sun glint mask	input	Internally determined but needs information on viewing geometry	grid(xsize, ysize)
	Day/night flag	input	Internally determined but needs information on viewing geometry	grid(xsize, ysize)
Ancillary Data	Land/Water mask	Input	1 km dataset <a href="http://glcf.umiacs.umd.edu/data/landcover">http://glcf.umiacs.umd.edu/data/landcover</a>	grid(xsize,ysize)

- **Sun glint mask**

The ADP product algorithm is designed to generate internal sun glint mask based on VIIRS viewing and illuminating angles. The sun glint angle ( $\eta$ ) is calculated as follows

$$\cos(\eta) = \cos(\theta_0) * \cos(\theta) + \sin(\theta_0) * \sin(\theta) * \cos(180 - \varphi)$$

$\theta_0$  : solar zenith angle

$\theta$  : satellite zenith angle

$\varphi$  : relative azimuth angle

Note that,  $\varphi$  is defined as the difference between solar azimuth angle and satellite azimuth angle. An area with calculated sun glint angle greater than zero and less than  $40^\circ$  is defined as sun glint area.

- **Day/night mask**

A day/night flag is determined internally based upon the solar zenith angle. Day is defined as solar zenith angle of less than or equal to  $87^\circ$ , while night is defined as solar zenith angle greater than  $87^\circ$ .

- **Land/water mask**

The only static input data required by the ADP product algorithm is a global 1km land/water mask. The global land cover classification collection created by The University of Maryland Department of Geography with Imageries from the AVHRR satellites acquired between 1981 and 1994 [Hansen et al., 1998] is the source (<http://glcf.umiacs.umd.edu/data/landcover/>).

**Table 10 JPSS VIIRS ADP product cloud mask tests to NPP VIIRS cloud mask (VCM)tests**

Cloud tests in ENTERPRISE algorithm No.	VCM tests Byte No. (Bit No.)*	Description	Locations where the tests are used in ADP product
pCirrus1	5(3)	Thin Cirrus Flag	Smoke over Water Dust over water Smoke over land Dust over land
pCirrus2	1(7)	Cirrus Detection (IR) (BT <sub>M15</sub> -BT <sub>M16</sub> )	Smoke over Water Dust over water Smoke over land Dust over land
pCirrus3	1(6)	Cirrus Detection (Solar) (R <sub>M9</sub> )	Smoke over Water Dust over water Smoke over land Dust over land
pFlag1	2(2)	IR Temperature Difference Test (BT <sub>M14</sub> - BT <sub>M15</sub> ) &(BT <sub>M15</sub> - BT <sub>M16</sub> )	Smoke over water Smoke over land
pFlag2	2(1)	High Cloud Test (BT <sub>M12</sub> - BT <sub>M16</sub> )	Smoke over land
pShadow	1(3)	Shadow Detected	Smoke over Water Dust over water Smoke over land Dust over land
pFire	2(5)	Fire Detected	Smoke over land Dust over land

\*Both byte and bit starting from 0

**Table 11 Mapping of ADP cloud tests with different cloud mask product**

Cloud tests in ENTERPRISE algorithm	MODIS CLOUD MASK Byte No. (Bit no.)	Suomi NPP VIIRS Cloud mask (VCM) tests	JPSS VIIRS BAYESIAN CLOUD_MASK tests Byte No. (Bit No.)	Description of Bayesian Cloud Mask tests	Locations where the tests are used in ADP
pCirrus1	2(0) (High cloud 1.38um)	pVCM_Cirrus1 Cirrus Detection (Byte 1, bit 6)	7 (5-6)	CIRREF- Near IR Cirrus Test (1.38 μm) value=3 (confident cloudy)	Smoke over land Dust over land
pCirrus2	1(7) (High cloud 6.7um test)	pVCM_Cirrus2 Cirrus Detection (Byte 1, bit 7)	7 (5-6)	CIRREF- Near IR Cirrus Test (1.38 μm) value=3 (confident cloudy)	Smoke over Water Dust over water Smoke over land Dust over land
pCirrus3	1(1) (thin cirrus, solar test)	pVCM_Cirrus3 Cirrus Detection (Byte 5, bit 3)	7(5-6)	CIRREF- Near IR Cirrus Test (1.38 μm) value=3 (confident cloudy)	Smoke over Water Smoke over Land
pFlag1	2(2) (IR Temperature difference)	pVCM_Flag1 IR temperature difference test (BTM14 - BTM15) &(BTM15-BTM16) (Byte 2, bit 2)	5 (3-4) &4(5-6)	PFMFT – Positive FMFT (Split-Window BTD) Test and 11um -8.5um test value=3 (confident cloudy)	Smoke over land
pFlag2	2(3) (3.7um-11um test)	pVCM_Flag2 Temperature difference test (BTM15 - BTM12) (Byte 2, bit 3)	6(3-4)	11um -3.75um test value=3 (confident cloudy)	Smoke over land
pShadow	1(2) Shadow Test	Shadow Detected	2(7)	Shadow contaminated Flag	Smoke over Water Dust over water Smoke over land Dust over land
pFire	N/A	Fire Detected	2(8)	Fire contaminated Flag	Smoke over land Dust over land

### **3.4 Theoretical Description**

The ADP product algorithm attempts to separate cloudy and clear pixels from those with smoke or dust. The detection of smoke or dust relies on the distinctive signature of smoke or dust which is often expressed in terms of spectral variations of the observed brightness temperature or solar reflected energy. The spectral variation of the refractive index plays an important role in the success of these methods. In addition, the scattering and absorption properties of an aerosol also depend on the particle size distribution and the particle shape. Several aerosol remote sensing techniques have been developed using observations from the Advanced Very High Resolution Radiometer (AVHRR) [e.g. Barton et al., 1992]. Similar to the dust plumes, the volcanic ash plumes often generate negative brightness temperature differences between  $11\mu\text{m}$  ( $BT_{11}$ ) and  $12\mu\text{m}$  ( $BT_{12}$ ). Prata [1989] has demonstrated the detection of volcanic aerosols using two infrared channels, while Ackerman and Strabala [1994] applied observations at 8.6, 11 and  $12\mu\text{m}$  from the Hyper Spectral Infrared Sound (HIRS) instrument to study the Mt. Pinatubo stratospheric aerosol. Recently, Ciren and Kondragunta [2014] developed a simple and fast technique to detect dust based on MODIS observations in the deep-blue (412 nm), blue (440 nm) and shortwave-IR (2130 nm) bands. This technique utilizes the spectral dependence of dust absorption, surface reflectance, and differences in absorbing/scattering properties between small and large particles.

Image based aerosol detection always involves assumptions of the radiometric characteristics of aerosol, clear and cloudy scenes. The surface conditions also influence the separation of aerosol pixels from those with clear-sky or cloud. The ADP product algorithm currently uses spectral and spatial tests to identify pixels with smoke or dust in the daytime. The algorithm also treats the detection differently for water and land.

#### **3.4.1 Physics of the Problem**

Techniques for the remote sensing of aerosols using solar and thermal measurements from satellites have been developed for several instruments, including AVHRR and MODIS. Fundamentally, these methods are based on the radiative signatures of aerosols. The problem of accurate detection and classification is compounded by the fact that the physical characteristics of aerosols (e.g. particle size distribution, concentration, chemical composition, location in the atmosphere) change as the aerosol layer develops and dissipates. These physical changes are capable of affecting the radiative characteristics of the original aerosol and our capability to detect them from satellite observations. In addition to being present at the source region, aerosols are transported by winds to other regions of the globe.



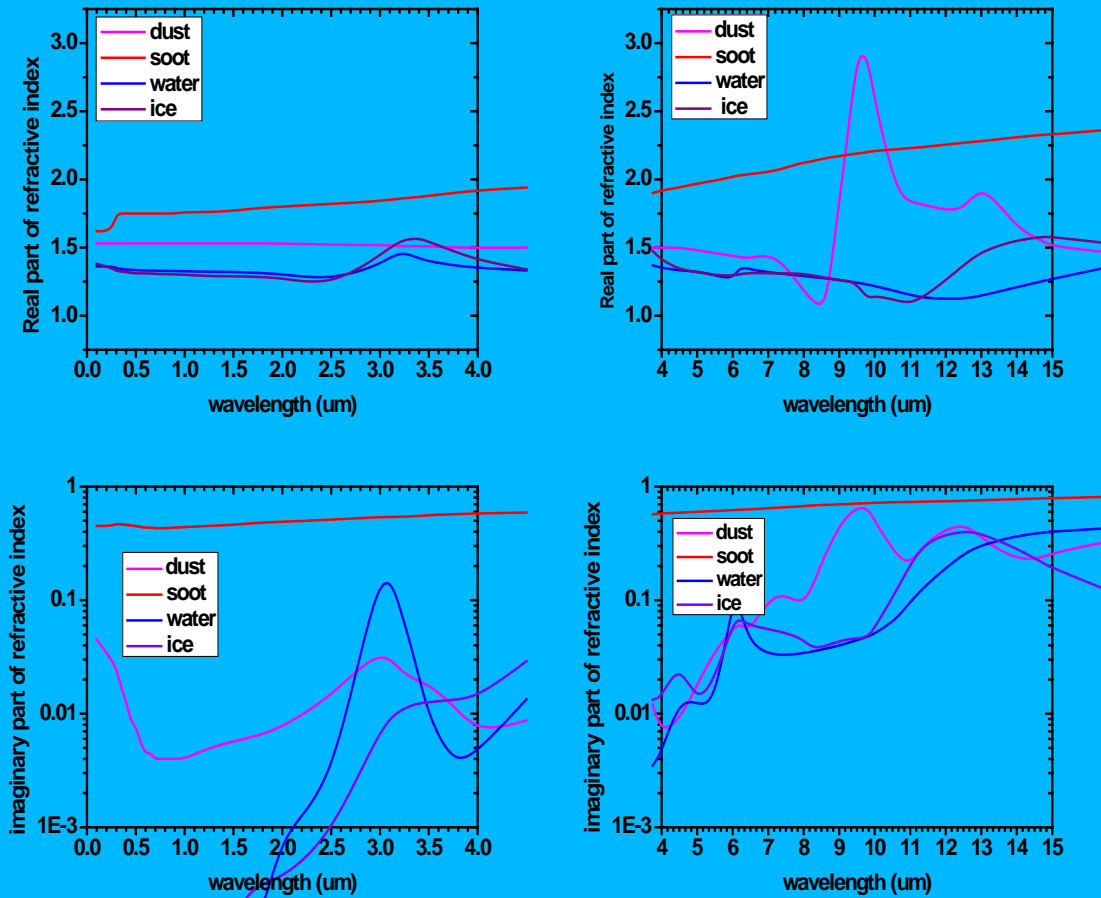


Figure 2: Real and imaginary part of dust, soot, water and ice as a function of wavelength. Plots are based on data obtained from CRTM.

Fundamentally, the radiative signatures of an aerosol layer are determined by the scattering and absorption properties of the aerosol within a layer in the atmosphere. These are:

- Extinction coefficient,  $\sigma_{\text{ext}}$  (which integrated over path length gives the optical thickness,  $\tau$ ). This parameter characterizes the attenuation of radiation through an aerosol volume due to aerosol scattering (measured by scattering coefficient  $\sigma_{\text{sca}}$ ) and absorption (measured by absorption coefficient  $\sigma_{\text{abs}}$ ) so that  $\sigma_{\text{ext}} = \sigma_{\text{sca}} + \sigma_{\text{abs}}$ .
- Single scattering albedo,  $\omega_0 = \sigma_{\text{sca}} / \sigma_{\text{ext}}$ , which describes how much attenuation of radiation is due to scattering. It ranges between 1 for a non-absorbing medium and 0 for a medium that absorbs and does not scatter energy.
- Phase function,  $P(\mu, \mu')$  which describes the direction of the scattered energy. Here  $\mu$  and  $\mu'$  are the cosine of solar and local zenith angles, respectively.

There are three important physical properties of a particle that are needed to determine the scattering and absorption properties listed above:

- The index of refraction ( $m = m_r - im_i$ ) of the particle: The index of refraction of the medium is also required, but for air it is 1. Measurements of the index of refraction of a material are very difficult to make [Bohren and Huffman 1983]. The  $m_r$  is an indication of the scattering properties while the  $m_i$  is an indication of the absorption characteristics of the material. The scattering and absorption properties of an aerosol also depend on the particle size distribution. The index of refraction of smoke and dust is different from ice or water (Figure 2), which suggests that multi-spectral techniques should be useful in separating the aerosol from clouds. In addition,  $m_i$  of dust exhibits a sharpest increase with the decreasing wavelength in deep blue region, indicating the spectral contrast between two neighboring wavelengths in this region is able to separate dust from others.
- The shape of the particle: Microscopic analysis reveals that aerosols are irregular in shape. Thus, the assumption of spherical particles is often not accurate but a reasonable approximation. Shape effects may be a particular problem in the vicinity of strong infrared absorption bands for small particles with a uniform size distribution [Bohren and Huffman, 1983]. As no satisfactory method of handling the radiative properties of irregular shaped particles has been developed for general application to remote sensing techniques, the sensitivity studies generally assume spherical shaped particles.
- The size distribution of the particles,  $n(r)$ : In addition to defining the radiative properties, the  $n(r)$  also determines the aerosol mass concentration. Particle size distributions of aerosols are often expressed as a log-normal distribution.

Because of these distinctive wavelength dependent aerosol properties, the spectral threshold based techniques are used to detect dust, smoke, volcanic ash work. Those techniques generally can be grouped as IR-based, IR/Visible based and UV/Deep-blue based, depending on the wavelength range of the utilized aerosol signatures. For aerosols with a small particle size, such as smoke and haze, their distinctive signatures are mainly in the short-wavelength, while for aerosols with a large particle size, such as dust and volcanic ashes, their distinctive signatures are in the IR wavelengths.

As for dust, it exhibits distinct radiative signatures in the UV, visible and IR regions (Sokolik, 2002). Various satellite-based dust detection techniques have been developed by utilizing its signature either in the UV (Herman et.al, 1997), visible (Miller, 2003; Jankowiak and Tanre', 1992; Martins et al., 2002; Kaufman et al., 1997), IR (Ackerman, 1997; Darmenov and Sokolik, 2005; Hansell et al., 2007) or a combination of visible and IR (Evan et al., 2006; Cho et al., 2013). Strong absorption by dust and low surface reflectivity in the UV spectral region enables the detection of absorbing aerosol including dust in the atmosphere (Herman et al., 1997). In addition, unlike most other dust detection techniques which can only provide a simple binary mask, absorbing Aerosol Index (AI) is also associated with the intensity of dust, although quantifying the dust loading in terms of optical depth requires the knowledge of dust layer height ( Hsu et al., 1999; Torres et al., 2002). However, UV aerosol detection technique is limited by its inability to separate dust from other absorbing aerosol such as smoke. Dust absorption features in the visible region (a brownish color as seen by human eyes), is well utilized to detect dust using spectral and spatial variability tests (Miller, 2003, Darmenov and Sokolik, 2009; Zhao et al., 2010; Cho et al., 2013). However, clouds, other type of aerosols, and bright surfaces can become a major interference. A unique radiative signature of dust in the IR window region, i.e., a negative brightness temperature difference between 11  $\mu\text{m}$  and 12  $\mu\text{m}$ , is widely used to distinguish the effect of dust from that of clouds (Sokolik, 2002; Legrand et al., 2001; Bullard et.al, 2008). Some algorithms use 8.5  $\mu\text{m}$  in addition to 10

$\mu\text{m}$  and  $11 \mu\text{m}$  to detect dust using tri-spectral differencing techniques (Hu et al, 2008; Ackerman, 1989; Ackerman, 1997, Ashpole *et al.*, 2012). However, as Darmenov and Sokolik (2005) indicated that the magnitude or even the sign of the brightness temperature difference depends on the composition of the dust, height of the dust layer and surface emissivity, and thus the ability of detecting dust can vary from location to location. In addition, another complication with IR detection of dust is from the water vapor absorption in longwave IR, which significantly affects the detection over regions and/or seasons depending on atmospheric water vapor content (Ashpole *et al.*, 2012). Besides utilizing the dust signature in brightness temperature difference between  $11 \mu\text{m}$  and  $12\mu\text{m}$ , Kluser and Schepanski (2009) further utilized the dust effect on diurnal cycle of brightness temperature in  $11 \mu\text{m}$  to derive a Bi-temporal Mineral Dust Index (BMDI) for Meteosat Second Generation (MSG) IR observations. However, it is only for over land, applicable only to geostationary satellite observations, and based on the assumption that diurnal variability of dust plume is small, which is not always true for transported dust.

For dust and volcanic ashes, their bulk transmittances display a strong spectral variation in the  $8\text{-}10 \mu\text{m}$  and  $10\text{-}12 \mu\text{m}$  regions. This is also a spectral region over which the atmosphere is fairly transparent. For these reasons, techniques have been developed which successfully employ satellite radiance measurements at  $11$  and  $12 \mu\text{m}$  to detect dust and volcanic ashes. These split window IR techniques have primarily been applied to volcanic aerosols, particularly those from sulfur-rich eruptions [e.g. Prata 1989; Barton et al. 1992] as well as dust outbreaks [Legrand et al., 1992, 2001; Evan et al., 2006]. As demonstrated in Figure 3, dust absorbs more radiation at  $12\mu\text{m}$  than  $11\mu\text{m}$ , which causes the brightness temperature difference between the two to be negative.

The positive  $BT_{11\mu\text{m}}-BT_{12\mu\text{m}}$  values are usually associated with clear sky atmospheres, since water vapor has both absorption and emission in the  $11$  and  $12 \mu\text{m}$  channels, and the weighting function for the  $11\mu\text{m}$  channel peaks lower in the atmosphere than the  $12\mu\text{m}$  channel does. However, with the presence of a dry air mass, often associated with dust events, will tend to reduce the positive  $BT_{11\mu\text{m}}-BT_{12\mu\text{m}}$ . In addition, as shown in Figure 2, dust has a larger absorption at  $12\mu\text{m}$  than at  $11\mu\text{m}$ , so that dust plumes generally have a higher emissivity and lower transmissivity in the  $12 \mu\text{m}$  channel [Ackerman, 1997; Dunion and Velden, 2004]. For more elevated dust layers, the increased temperature separation between the dust layer and the surface, and coincident reduction of dry air closer to the peak of the  $11\mu\text{m}$  weighting function makes the split window brightness temperature difference even more less positive. However, this difference has also been observed to be affected by the optical thickness of a given dust plume, so that in thick optical depths the  $BT_{11\mu\text{m}}-BT_{12\mu\text{m}}$  difference becomes more negative.

Darmenov and Sokolik [2005] further explored the brightness temperature difference technique using MODIS data applied to dust outbreaks from different regions of the globe. In general,  $BT_{8\mu\text{m}}-BT_{11\mu\text{m}}$  becomes less negative and  $BT_{11\mu\text{m}}-BT_{12\mu\text{m}}$  becomes more negative with increasing dust loading (Figure 3). However, in the ADP algorithm, the  $3.9 \mu\text{m}$  is chosen instead of  $8 \mu\text{m}$  because  $3.9 \mu\text{m}$  has less water vapor absorption and also to eliminate the false alarm from low level clouds (often towering cumulus).

In the short-wavelength region, dust absorbs at blue wavelengths and appears visually brown in color. Clouds are spectrally neutral and appear white to human eyes. For this reason, the reflectances at  $0.86$ ,  $0.47$  and  $0.64\mu\text{m}$  have been used to identify dust. This is often done in a ratio of one to another or as a normalized difference index. For example, the MODIS aerosol optical depth retrieval algorithm has a condition that ratio of reflectances between  $0.47 \mu\text{m}$  and  $0.64 \mu\text{m}$  should be less than  $0.75$  for the central

pixel in a 3 X 3 box to be identified as dust. Evan et al [2006] use a constraint that the reflectance value of the 0.86 $\mu\text{m}$  channel ( $R_{0.86\mu\text{m}}$ ) divided by the reflectance value of the 0.63 $\mu\text{m}$  channel ( $R_{0.63\mu\text{m}}$ ) is within the range of 0.6–1.0 for the AVHRR (this range is slightly different for MODIS due to differences in the spectral response functions). Again, due to the nonlinear relationship with optical thickness, we chose to square the reflectances prior to applying a test. The physical basis for this test is that the presence of smaller aerosols, like smoke, tends to reduce the values for this ratio, as smaller particles are more efficient at scattering light at 0.63 $\mu\text{m}$ . Although dust particles are observed to scatter more light at 0.63 $\mu\text{m}$  than at 0.86  $\mu\text{m}$  probably due to their size, they tend to exhibit more uniform scattering across this spectral region [Dubovik et al., 2002]. A ratio type test of  $R_{0.86\mu\text{m}}/ R_{0.63\mu\text{m}}$  has been found to be useful in discriminating pixels containing smoke from those with dust

Although dust particles are observed to scatter more light at 0.63 $\mu\text{m}$  than at 0.86 $\mu\text{m}$  probably due to their size, they tend to exhibit more uniform scattering across this spectral region [Dubovik et al., 2002]. Thus, the ratio  $R_{0.86\mu\text{m}}/ R_{0.63\mu\text{m}}$  test [Evan et al., 2006] has been found to be useful in discriminating pixels containing smoke from those with dust. Another test for dust examination over water is the requirement that the ratio of reflectance at 0.47  $\mu\text{m}$  and 0.64  $\mu\text{m}$  is smaller than 1.2. Similar to the dust detection over land, low level clouds (often towering cumulus) can also have a negative split window brightness temperature difference. Therefore, brightness temperature between 3.9  $\mu\text{m}$  and 11  $\mu\text{m}$  can be used to screen out cloud contaminated pixels.

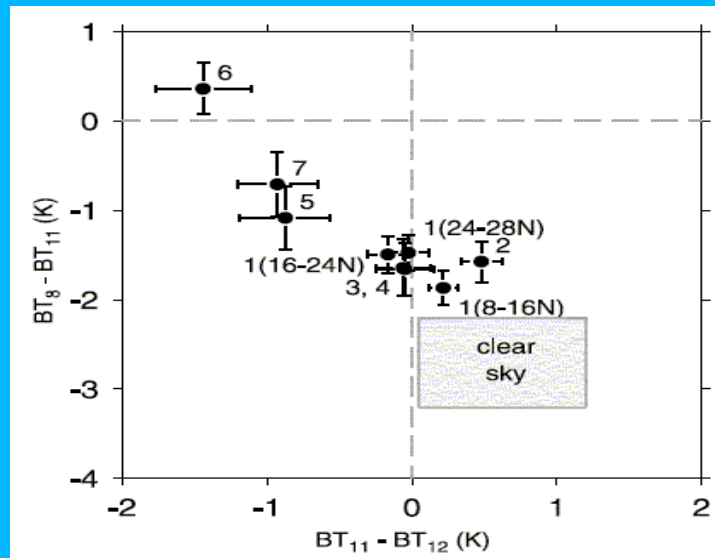
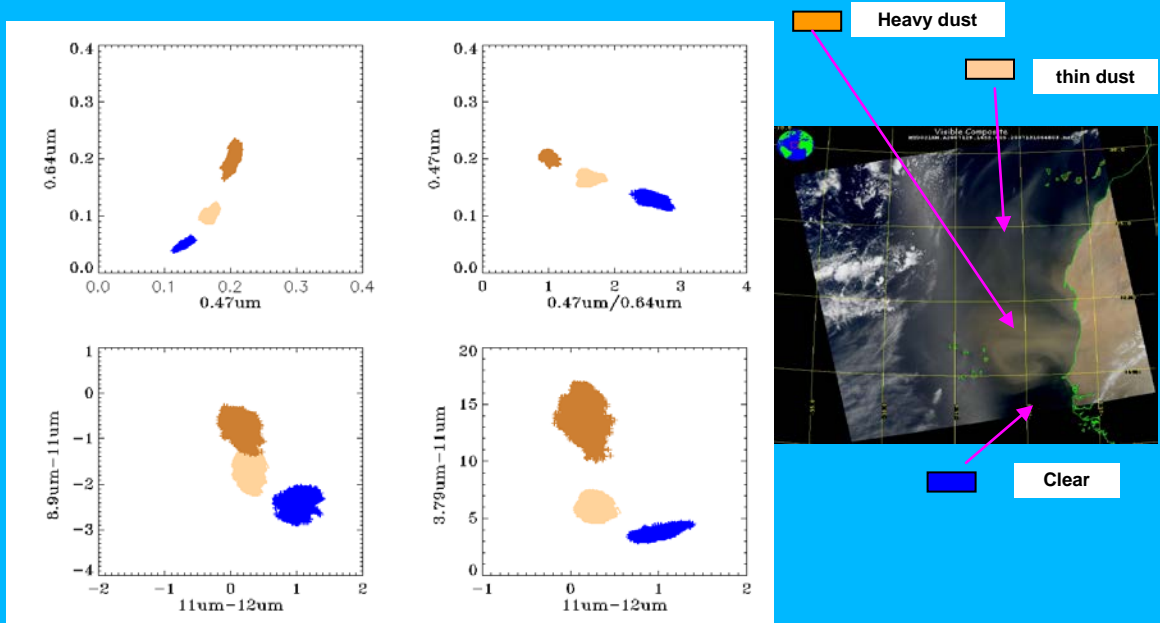


Figure 3. Combined tri-spectral diagram of brightness temperature differences for “heavy dust” pixels, indicated by the number 1 to 7, and for clear sky. From Darmanov and Sokolik [2005].

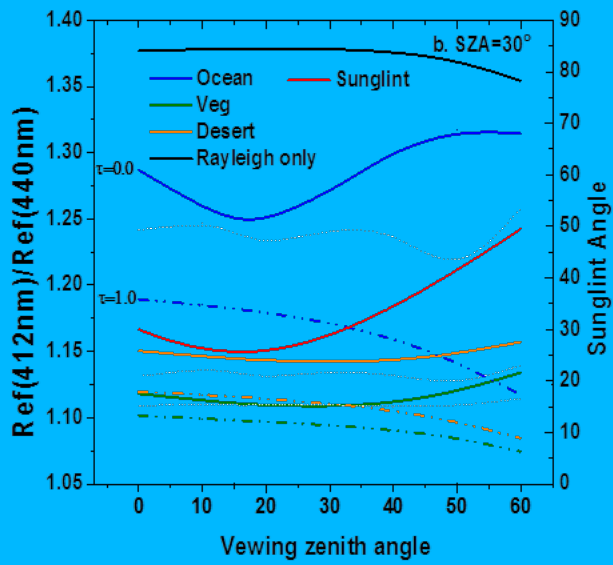
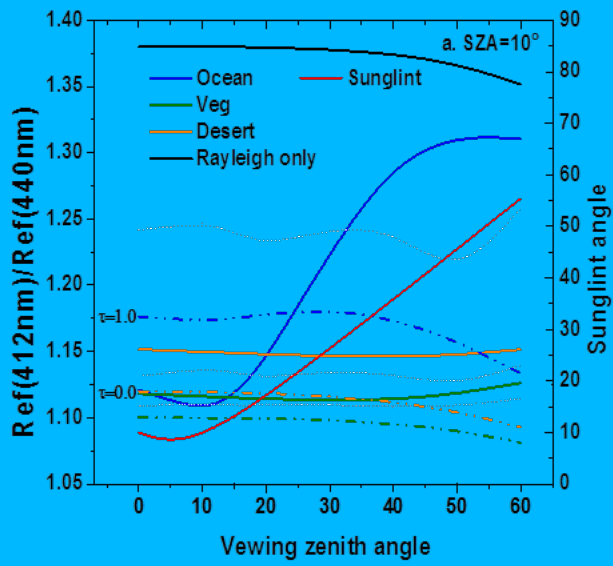
The RGB image in Figure 4 shows a dust plume with different regions of heavy dust, thin dust, and clear sky clearly identified. For these different regions, the relationship between different visible and IR BTD are plotted in the four panels of Figure 4. Clear sky pixels have low reflectance at both 0.47 and 0.64  $\mu\text{m}$ , thin dust has elevated reflectances at these channels, and thick dust pixels have 20% or greater reflectance at these channels. The BTD between 3.9  $\mu\text{m}$  and 11  $\mu\text{m}$  plotted against the BTD between 11  $\mu\text{m}$  and 12  $\mu\text{m}$  shows a clear separation of thick dust pixels compared to thin dust and clear-sky.



**Figure 4: The relationship between various combinations of channels for heavy, thin dust, and clear conditions.**

Besides separating clouds from other type of aerosols, the challenge of detecting dust lies largely in separating it from a bright surface that is generally the source of airborne dust. In the deep-blue to blue wavelength region, reflectance from a bright surface is well below the critical surface reflectance: a quantity to define if signal from aerosol is distinguishable from the surface. A deep-blue aerosol optical depth algorithm developed by Hsu et al (2004) shows aerosol properties can successfully be retrieved even over a bright surface, when measurements at deep blue channels are used. In the deep blue aerosol retrieval algorithm, deep-blue Absorbing Aerosol Index (AAI) defined in a manner similar to the Total Ozone Mapping Spectrometer (TOMS) AI is used for cloud screening to separate aerosol from clouds but aerosol type is determined using the aerosol model selected in the aerosol optical thickness retrieval algorithm. Note that, like TOMS AI, the AAI described by Hsu et al (2004) cannot separate dust from other absorbing aerosols.

The advantage of using measurements in the blue wavelength region (410 to 490 nm) to retrieve aerosol optical properties has been clearly demonstrated by Hsu et al. (2004, 2006). Due to the fact that the sensitivity of reflectance to the dust in the atmosphere decreases with the increasing wavelength, the spectral contrast between two neighboring wavelengths can be used as an indicator for the presence of dust. The spectral shape of the reflectance at the Top of the Atmosphere (TOA) for a cloud-free atmosphere is determined by three main processes: Rayleigh scattering, absorption and scattering by aerosols, and reflection by the underlying surface. The strong wavelength-dependent Rayleigh scattering creates a strong contrast between two neighboring wavelengths. The presence of dust, however, reduces this contrast as a result of the increased absorption with decreasing wavelength. As for the underlying surfaces, their effects on spectral contrast depend on the spectral variability of surface reflectance. For surface type such as water, the surface reflectance is nearly independent of wavelength within deep-blue to blue region except for areas with sunglint; therefore, its effect on the spectral contrast is minimal. However, arid or desert surfaces show an increased reflection with the increasing wavelength (Hsu et.al. 2004), similar to absorbing aerosol; reflection from these surfaces will also reduce the spectral contrast.



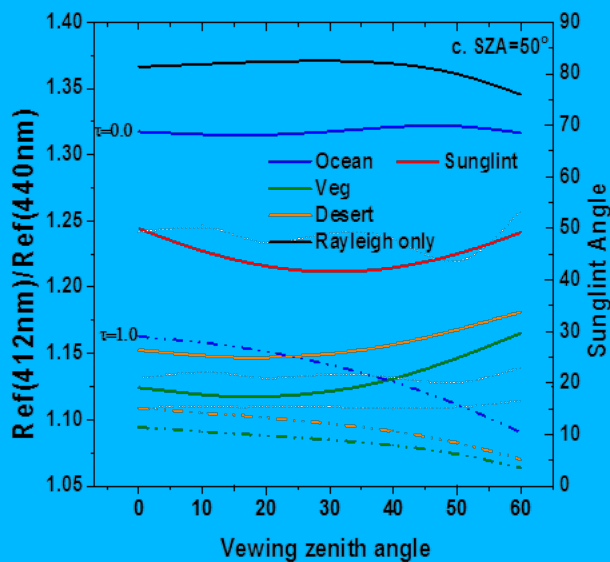


**Figure 5: Ratio of the simulated TOA reflectance at MODIS band 8 (412 nm) and band 9 (440 nm) as a function of viewing zenith angle at a solar zenith angle of 10° (a), 30° (b) and 50° (c). Solid lines represent a clear atmosphere bounded by ocean (blue), vegetation (green), and desert (orange). Dashed lines represent an atmosphere with dust (AOD at 550 nm is 1.0) bounded by ocean (blue), vegetation (green) and desert (orange). Red solid lines are sunglint angle over ocean. Relative azimuth angle of 120° is used. Total ozone amount is set at 350 DU.**

This is illustrated by simulating the spectral dependence of TOA in the blue wavelength region for different surface and atmospheric conditions with a thoroughly tested vector version of 6S radiative transfer code (Kotchenova et. al. 2006). Figure 5 shows the ratio between MODIS band 8 (412 nm) and band 9 (440 nm) TOA reflectance at three solar zenith angles (SZA) (i.e. 10°, 30° and 50°) for various scenarios: (a) an atmosphere with only Rayleigh scattering bounded by a black surface (surface reflectance of 0.0), (b) an atmosphere with Rayleigh scattering bounded by desert, vegetation and water, and (c) an atmosphere with Rayleigh scattering and dust bounded by desert, vegetation and water. Note that, the sunglint angles are also shown to illustrate the sunglint region over ocean.

In Figure 5, for different scenarios, dashed line and solid lines represent dust-free and dust with an aerosol optical depth ( $\tau$ ) of 1.0, respectively. A non-spherical dust, i.e., spheroid dust model, based on almucantur inversion of AERONET observations [Dubovik, 2006] is used in the simulations. The details of the microphysical/optical properties of the dust model were given by Remer et al. [2006]. Surface spectral reflectance of vegetation and sand embedded in 6S are used to represent vegetated and desert surface. Ocean Bi-directional Reflectance Distribution Function (BRDF) from 6S was selected to calculate the ocean surface reflectance for an easterly wind speed of 6 m/s. It is seen that the contrast between reflectances at 412 nm and 440 nm become smaller when dust is present in the atmosphere for desert, vegetation and sunglint-free (with a sunglint angle  $>30^\circ$ ) ocean surface, compared to dust-free condition. The reduction in contrast between the two wavelengths is most significant for sunglint-free ocean surface and relatively smaller for desert and vegetated surfaces because sunglint-free ocean surface has a relatively lower and flat spectral reflectance. For a clear atmosphere over ocean outside of sunglint region, TOA reflectance is dominated by the spectral signature of Rayleigh scattering. While desert and vegetated surfaces are brighter and have spectrally increasing reflectance that is opposite to

the spectral signature of Rayleigh scattering. Therefore, the spectral variation of TOA reflectance is reduced for dust-free atmosphere over desert and vegetation. In addition, it is also seen that the decrease in spectral contrast is larger at both a larger viewing zenith angle (VZA) and a larger SZA, since the slant path increases with the increasing SZA and VZA. However, it is also seen that the spectral contrast decreases largely with the decreasing sun glint angle for ocean surface without dust, indicating that reflection from sun glint itself may reduce the spectral contrast as well. This has to be taken into account to avoid misidentifying sun glint as dust.

The reduction in spectral contrast of Rayleigh scattering when dust is present in the atmosphere is also seen in satellite observations. Figure 6a-b shows the regions highlighted by boxes where pixels are identified as clear and as dusty, respectively for over land and ocean. Figure 6c-d shows the ratio of TOA reflectance at 412 nm and 440 nm as a function of TOA reflectance at 412 nm for pixels from the selected boxes over land and over ocean. It is seen that the ratio of 412 nm to 440 nm for pixels with dust is distinct from clear pixels over ocean, showing the reduced contrast between 412 nm and 440 nm (see Figure 6d). Such separation is also seen for dust over desert (Figure 6c), although not as distinct as that for over ocean.

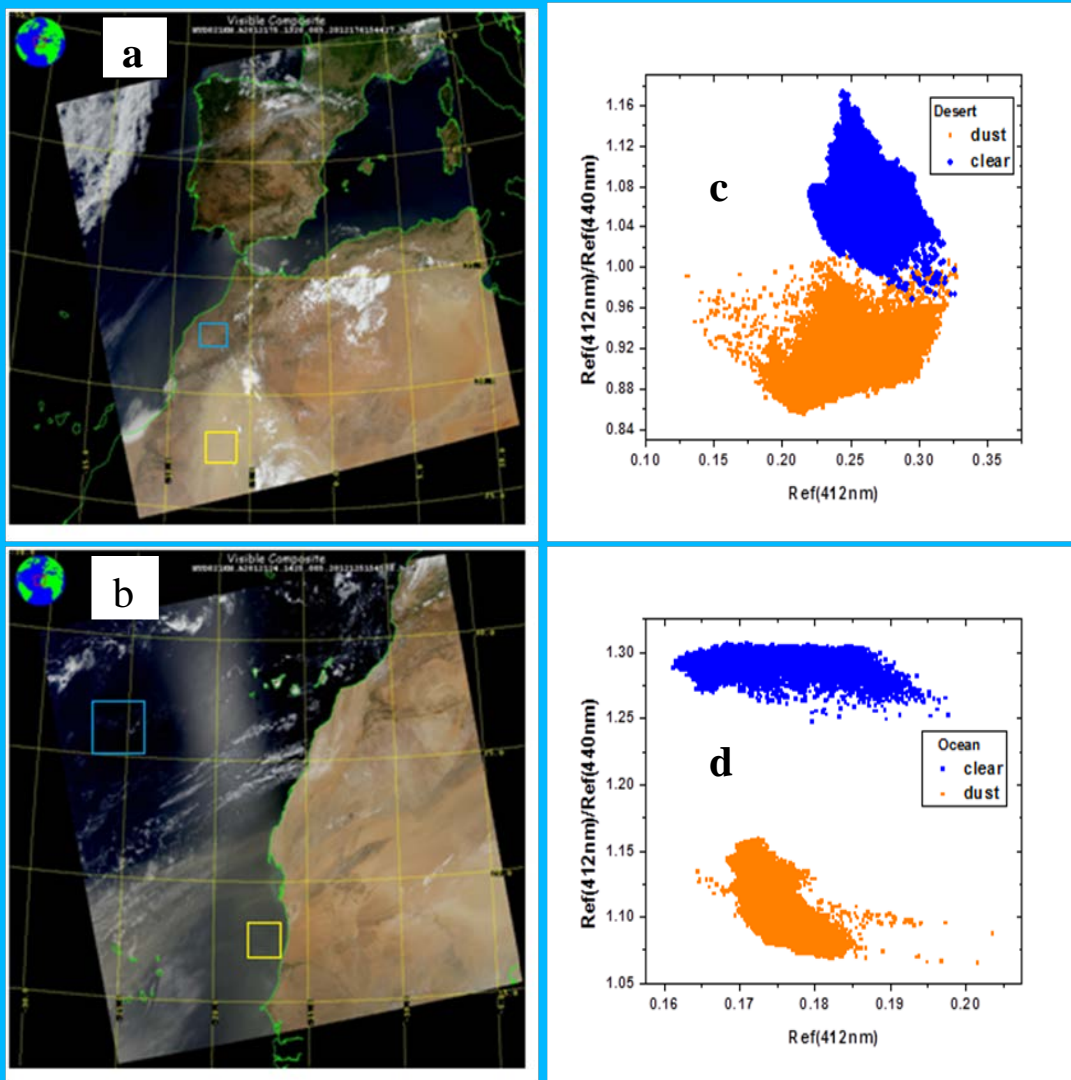




**Figure 6: (a) RGB image of MODIS Aqua Granule on May 3, 2012, 1425 UTC; (b) RGB image of MODIS Aqua granule on June 23, 2012, 1320 UTC; Ratio of the observed TOA reflectance at MODIS band 8 (412 nm) and band 9 (440 nm) as a function of the observed TOA reflectance at MODIS band 8 (412 nm) for pixels identified as clear (blue) and dust-laden (orange) over land (c) and over ocean (d).**

This analysis based on theory and observations suggests that the effect of dust in reducing the spectral contrast between 412 nm and 440 nm could be used as a way to detect the presence of dust in the atmosphere. However, using the spectral contrast under clear condition as a reference to detect dust requires the knowledge of spectral reflectance of underlying surface. To bypass this problem, the spectral contrast from a pure Rayleigh scattering is used as a reference, and different thresholds for the reduction in spectral contrast is chosen for over land and water. Therefore, an index similar to AI and absorbing aerosol index used in SeaWiFS (Hsu et al, 2000), named as Absorbing Aerosol Index (AAI) shown in Equation 1 has been developed.

$$AAI = -100[\log_{10}(R_{412nm}/R_{440nm}) - \log_{10}(R'_{412nm}/R'_{440nm})] \quad (1)$$

In Equation 1,  $R$  is the TOA reflectance,  $R'$  is the reflectance from Rayleigh scattering as computed by 6S code for a given location and satellite viewing geometry. To illustrate how AAI changes with the dust loading, 6S radiative transfer model simulations were used to calculate AAI for dust with different optical depths (at 550nm): no dust ( $\tau=0.0$ ), weak ( $\tau=0.5$ ), heavy ( $\tau=1.0$ ) and extreme dust loading ( $\tau=2.0$ ). Results are given in Figure 7a-c, showing the AAI as a function of viewing zenith angle, respectively for over desert, over ocean and over vegetation. Filled square, triangle, circle and diamond respectively represent different dust-loading indicated by dust aerosol optical depth at 550nm ( $\tau$ ) of 0.0, 0.5, 1.0 and 2.0. Dash-dotted, solid and dotted lines are for solar zenith angles of 10°, 30° and 50° respectively. The AAI values for heavy and extreme dust loadings are well separated from those of no dust for both desert and vegetation surface and especially for ocean surface outside sunglint region, indicating AAI is well suitable to detect heavy to extreme dust over both land and ocean. For over desert and vegetation, it is clearly seen that the separation increases with the increasing solar zenith angle and the increasing viewing zenith angle, suggesting AAI performs better for a larger solar and viewing zenith angle. And, the difference in AAI becomes smaller with the increasing dust loading. However, it should also be noted that the AAI threshold to detect dust has to be carefully chosen to minimize false alarms and maximize detection, especially for low aerosol loading at a lower solar and viewing zenith angle. Over ocean, it is seen that sunglint is a large factor to cause weak dust not detectable over sunglint region. As for over sunglint-free ocean, the separation between weak dust (represented by  $\tau=0.5$ ) and no dust (represented by  $\tau=0.0$ ) is much larger than those over land surface and is less sensitive to the changing solar and viewing zenith angles. This finding suggests that detecting low to weak dust with AAI is much better over ocean than over land surface.

However, as given in Figure 8a, other absorbing aerosol such as smoke also shows a similar effect on the spectral contrast between 412 nm and 440 nm as dust. Due to the fact that particle size of dust is considerably larger than smoke, therefore, dust extends its scattering signature even to shortwave IR wavelength, whereas smoke is mostly transparent (Kaufman et al, 2000). By introducing the observations at shortwave IR wavelength, it is possible to separate dust from other absorbing aerosols. As an example, Figure 8b shows a scatter plot between TOA reflectance at 412 nm and 2130 nm from MODIS for pixels identified as smoke, dust and clear over ocean. One can see that pixels with dust have higher reflectance at 2130 nm and are well separated from clear pixels and pixels with smoke. To this

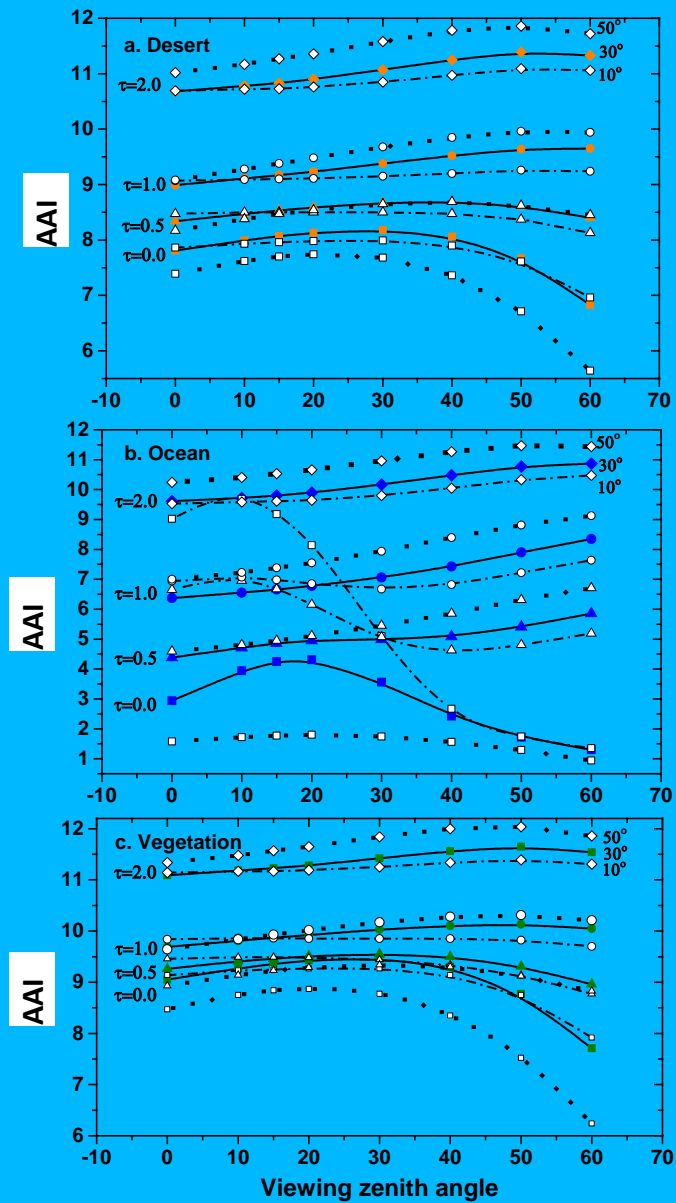


Figure 7: AAI as a function of viewing zenith angle over desert (a), over ocean (b) and over vegetation (c), for aerosol optical depth at 550 nm ( $\tau$ ) of 0.0 (square), 0.5 (triangle), 1.0(circle) and 2.0(diamond). Solar Zenith Angle (SZA) of 10°, 30° and 50° is represented by dash-dotted, solid and dotted lines, respectively. Note that relative azimuth is set at 120°.

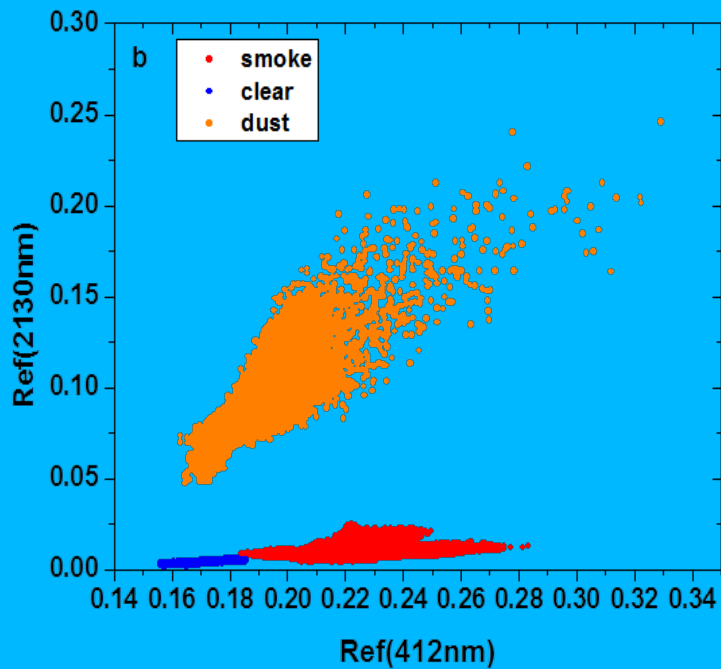
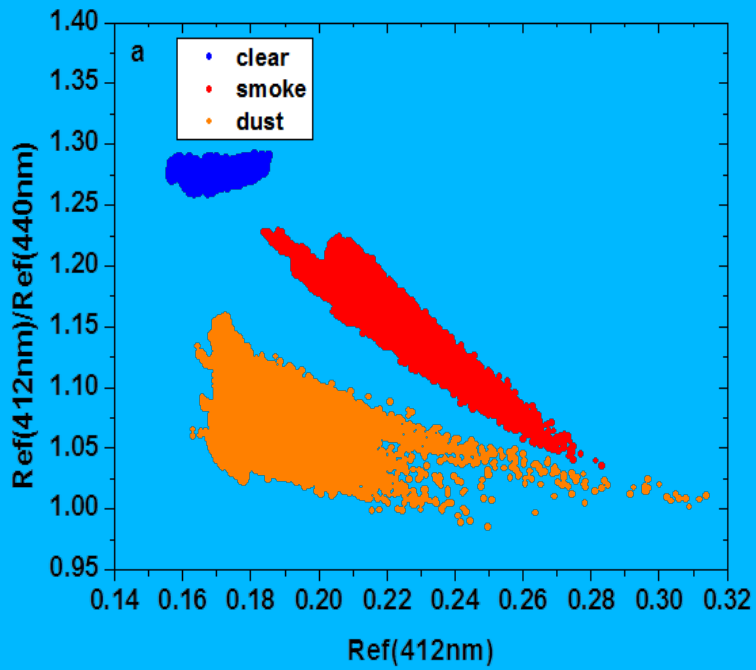


Figure 8: Ratio of the observed TOA reflectance at: a) MODIS band 8 (412 nm) and band 9 (440 nm), b) MODIS band 8 (412 nm) and band 7 (2130 nm), as a function of the observed TOA reflectance at MODIS band 8 (412 nm) for pixels identified as clear (blue), smoke-laden (red) and dust-laden (orange) over ocean.

end, a second index, named as Dust Smoke Discrimination Index (DSDI) is computed using the formula shown in Equation 2.

$$DSDI = -10[\log_{10}(R_{412nm}/R_{2130nm})] \quad (2)$$

In Equation 2,  $R$  is the observed TOA reflectance. The DSDI is applied to pixels which pass through the AAI threshold test.

As shown in above section, by using the spectral contrast between deep-blue and blue wavelength, absorbing aerosols, including smoke and dust, can be detected, furthermore, with the spectral contrast between deep-blue and shortwave IR wavelength, dust can be separated from other, including smoke, indicating this technique can also be used for both smoke and dust detection.

Besides the above-motioned deep-blue technique, signatures of smoke presence in other wavelengths are also used for smoke detection. For smoke detection overland, fire spots are first detected by looking at pixels with BTs at  $4.05 \mu\text{m}$  greater than  $350\text{K}$  and the BTD between  $4.05 \mu\text{m}$  and  $10.76 \mu\text{m}$  greater than or equal to  $10\text{K}$ . It is assumed that Pixels that pass fire test usually have thick smoke. Secondly, the smoke tests over land also take advantage of a linear relationship between the reflectance at visible band ( $0.67 \mu\text{m}$  for VIIRS) and shortwave IR band ( $2.25 \mu\text{m}$  for VIIRS). Figure 9 shows this relationship with the correspond bands at VIIRS. It is seen that surface reflectance at M5 is generally around 80 % of the surface reflectance at  $2.25\mu\text{m}$ . However, due to the fact that the size of smoke particle is relatively small, the signal from smoke will be extremely small in the shortwave IR wavelength; therefore, there is a larger increase in  $R_{0.67\mu\text{m}}$  than  $R_{2.25\mu\text{m}}$  for an atmosphere with the presence of smoke. As for separating smoke from clouds, spatial uniformity tests for M5 ( $0.67 \mu\text{m}$ ) band is used for over land, since clouds show large variability in this band compared to smoke, and also surface is darker.

As for smoke detection over water, spatial variability tests will also help in avoiding the misclassification of clouds as smoke. Since clear pixels, pixels loaded with thick smoke and clouds are more uniform than pixels with partial cloud or thin dust, by using the standard deviation of reflectance at  $0.86 \mu\text{m}$ , where both aerosol and clouds effects are moderate, pixels which contain thick smoke vs. clouds/thin smoke can be separated. It is known that smoke in visible channels looks brighter than water surface but darker than a cloud. However, it is very difficult to completely separate them by only using the reflectance test. Therefore, based on the fact that reflection from clouds is spectrally independent, while reflection from smoke has strong wavelength dependence, spectral contrast tests are combined to separate clouds, smoke and water surface. First of all, the ratio between  $R_{0.47\mu\text{m}}$  and  $R_{1.61\mu\text{m}}$  is used, the rationale for choosing these two channels is due to the fact that aerosol effect is larger at  $0.47\mu\text{m}$  but water is darker at  $1.61\mu\text{m}$ . Secondly, the ratio between  $R_{2.25\mu\text{m}}$  and  $R_{1.61\mu\text{m}}$  is combined to enhance the separation of smoke from clouds. Thirdly, by constraining  $R_{0.47\mu\text{m}}$  and  $R_{1.61\mu\text{m}}$ , thick smoke can be identified.

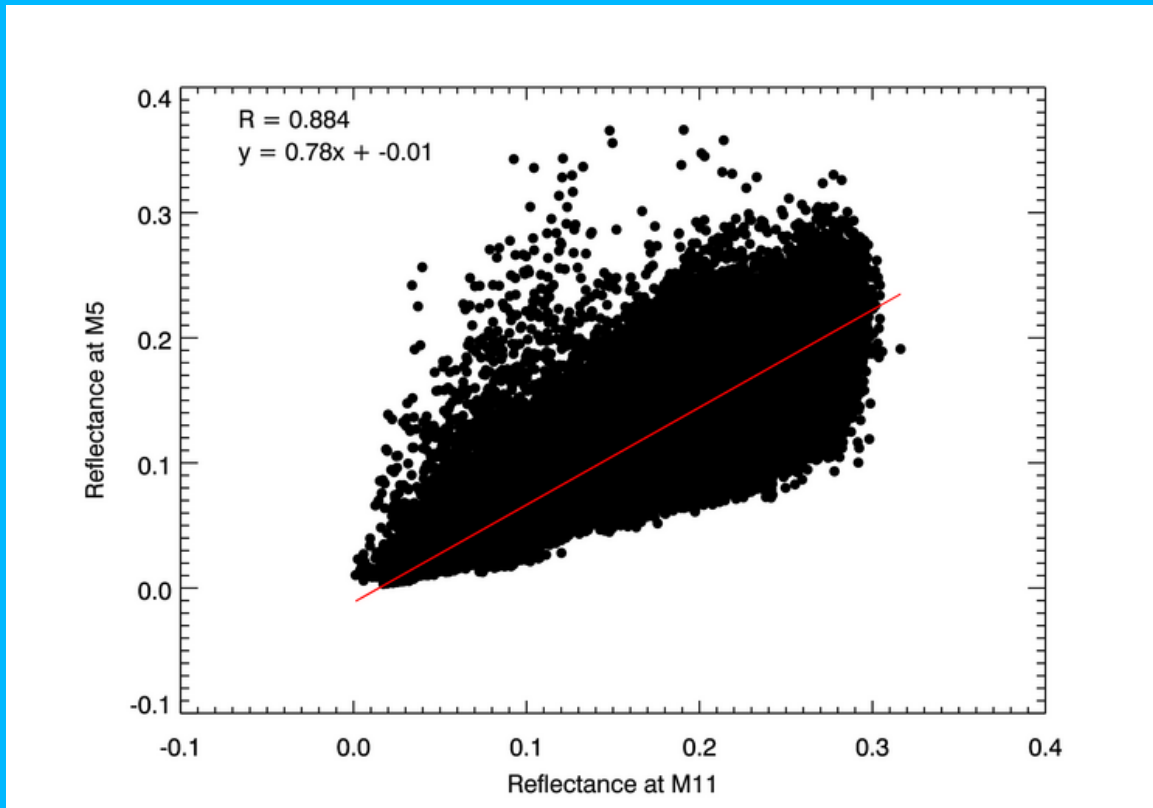


**Figure 9 : Surface reflectance at M5( 0.67μm) vs. surface reflectance at M11(2.25μm) from S-NPP VIIRS.**

As for illustration, scatterplots of the ratio of  $R_{0.47\mu\text{m}}$  to  $R_{1.61\mu\text{m}}$  and the ratio of  $R_{2.25\mu\text{m}}$  to  $R_{1.61\mu\text{m}}$  against  $R_{0.47\mu\text{m}}$  and  $R_{1.61\mu\text{m}}$  were shown, respectively for clear pixels, pixels loaded with thick smoke, thin smoke and cloudy pixels, in Figure 10.

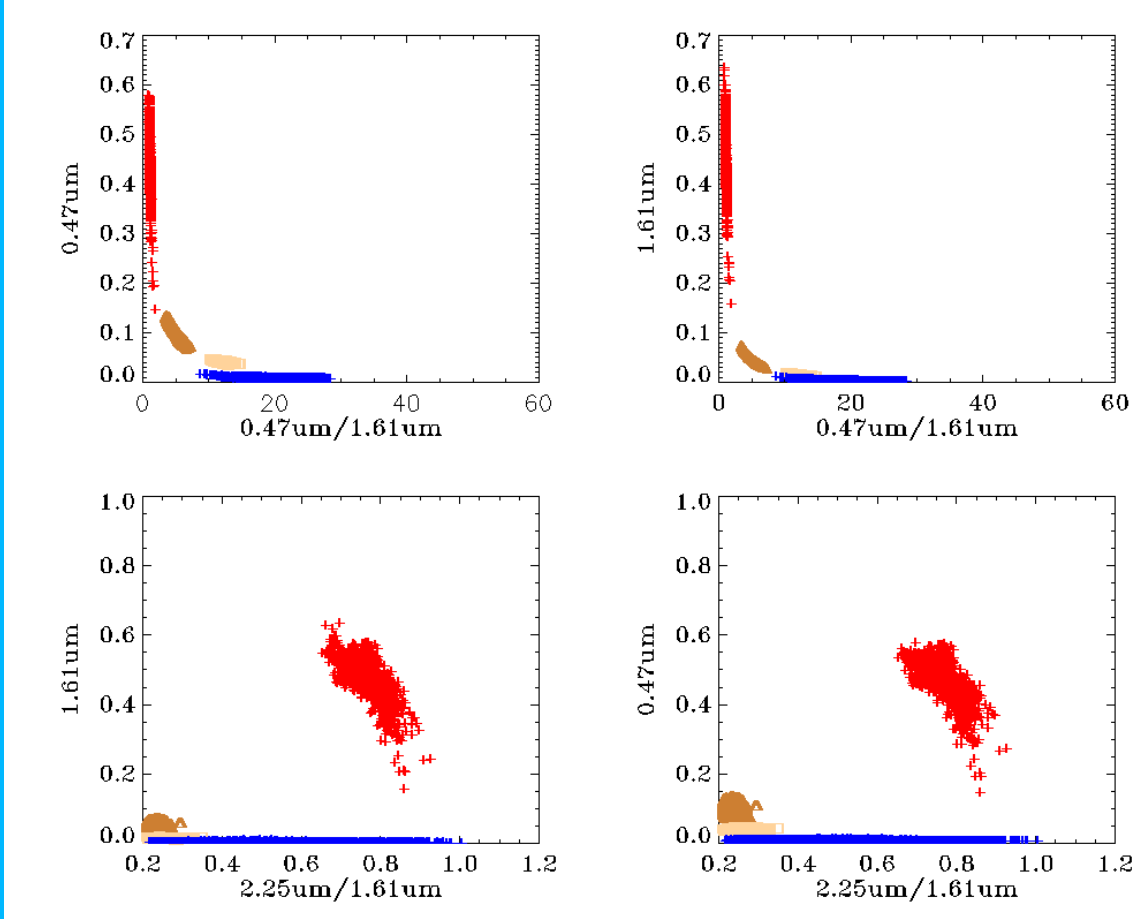


Figure 10: Scatter plots of the ratio of  $R_{0.47}$  to  $R_{1.61}$  vs.  $R_{0.47\mu m}$ , the ratio of  $R_{0.47}$  to  $R_{1.61}$  vs.  $R_{1.61\mu m}$ , the ratio of  $R_{2.25}$  to  $R_{1.61}$  vs.  $R_{0.47\mu m}$ , the ratio of  $R_{2.25}$  to  $R_{1.61}$  vs.  $R_{1.61\mu m}$  for clear-sky pixels (blue), thick smoke pixels (dark brown), thin smoke (light brown) and cloudy pixels (red).

### 3.4.2 Mathematical Description

Computation of binary flag for smoke/dust in the ADP product algorithm is a process of elimination and determination. It has three levels. First, any pixel which contains cloud (ice, high and optically thick clouds) and snow/ice, determined from input cloud mask and snow/ice mask, is tagged as a cloudy and snow/ice pixel respectively and not processed. Second, pixels contaminated by clouds but not screened by cloud mask are further identified by a combination of spectral and spatial variability tests. Third, spectral contrast tests, such as AAI and DSDI (see equation 1 and 2), are used to determine if a pixel has smoke or dust. Due to the fact that the contrast of smoke/dust to underlying surface is different for land and water, computation of binary flag for smoke/dust in the ADP product is separated for land and water. The following sections describe the various tests employed in the ADP product algorithm in detail. Besides the two indices given in equation (1) and (2), the symbols and formulae used in the various tests through the ADP product algorithm are defined as follows:

$$R_1 = \frac{R_{M3}}{R_{M5}}$$

$$R_2 = \frac{R_{M7}}{R_{M5}}$$

$$R_3 = \frac{R_{M3}}{R_{M10}}$$

$$R_4 = \frac{R_{M11}}{R_{M10}}$$

$$Rat_1 = \frac{R_{M5} - R_{M3}}{R_{M5} + R_{M3}}$$

$$Rat_2 = \frac{Rat_1^2}{R_{M3}^2}$$

$$NDVI = \frac{R_{M7} - R_{M5}}{R_{M7} + R_{M5}}$$

$$MNDVI = \frac{NDVI^2}{R_{M5}^2}$$

In the formulae listed above, “R” is reflectance, “Rat” is for ratio, “NDVI” is Normalized Difference Vegetation Index, “MNDVI” is Modified Normalized Difference Vegetation Index. Additionally variables such as “BT” for Brightness Temperature, “BTD” for Brightness Temperature Difference, “StdR” for Standard Deviation of Reflectance computed spatially for 3 X 3 pixels.

Calculation of StdR for pixel which is not on the edge of scan is from the surrounding 3 by 3 pixels. For pixels on the edge of scan, standard deviation for the closest pixel is assigned.

### 3.4.2.1 Snow/ice test over land

Before proceeding to any tests over land, it is important to identify pixels contaminated by snow/ice. As described earlier, VIIRS snow/ice product is the primary source, and if the primary source is unavailable, snow/ice mask from IMS is used as a second source. However, a further test is designed to catch any pixels that pass through but have snow/ice.

The specific internal tests as currently implemented are:

#### 1) Good data test

- $R_{M7}, R_{M8} > 0.0$  &
- $BT_{M15} > 0.0K$  &
- VIIRS quality flags for above channels indicate good data

#### 2) Snow and Ice tests

The Internal snow ice test over land relies on brightness temperature at M15 ( $BT_{M15}$ ) and Normalized Difference Snow Index ( $NDSI$ ).  $NDSI$  is defined as:

$$NDSI = \frac{(R_{M7} - R_{M8})}{(R_{M7} + R_{M8})} \quad (3)$$

The pixels is defined as snow/ice contaminated if  $BT_{M15} < 285K$  and  $NDSI > 0.1$ . And, ADP detection is not avoided but the detected snow/ice is outputted in snow/ice flag for quality control purpose for this pixel.

### 3.4.2.2 Dust Detection over Land

Dust detection over land has two paths. If either path identifies the presence of dust, then dust is shown to be present in the product. The first path is the same algorithm as for GOES-R Advance Baseline Imager (ABI) to detect dust over land, which is based on the spectral variability tests at visible bands and negative brightness temperature difference between two wavelengths in IR regions; the second one is designed for VIIRS, by taking advantage of observations of VIIRS at deep-blue bands. The path is determined by the availability of channels, if no deep-blue channels, as M1 and M2 for VIIRS, are available, the algorithm only takes the first path. Otherwise, both paths are taken.

#### 3.4.2.2.1 IR and visible-based dust detection

The IR and visible-based algorithm is adopted from the heritage of GOES-R ABI ADP algorithm. Figure 11 is a flow chart of the algorithm to detect the presence of dust over land during daytime (defined as solar zenith angle less than or equal to  $87^\circ$  degrees). The tests are not performed over snow and ice or in the presence of clouds.

The specific tests as currently implemented are:

- (1) Test for the presence of snow/ice by using both primary snow/ice mask and internal snow/ice mask, which is given in section 3.4.2.1. Test for the presence of clouds relies on VIIRS cloud mask. Pixel is considered to be obscured by clouds if any of these five cloud mask tests in Table 10, i.e. pCirrus1, pCirrus2, pCirrus3, pFlag1 and pFlag2, is true. Any pixel with positive snow/ice/ or clouds is not processed.
- (2) Test for the quality of the input radiance data
  - $R_{M3}, R_{M5}, R_{M7}, R_{M9} > 0.0$  &
  - $BT_{M12}, BT_{M15}, BT_{M16} > 0.0K$  &
  - VIIRS quality flags for above channels equal to zero, indicating quality of the data is assured.
- (3) Thin Dust detection: BTD and R tests – check for pixels with thin dust and no cirrus clouds  
For detection of thin dust, the following spectral contrast in the visible wavelength and brightness temperature difference are applied:

$$BT_{M15} - BT_{M16} \leq -0.2K$$



$$\begin{aligned}
& BT_{M12} - BT_{M15} \geq 15K \\
& R_{M9} < 0.035 \\
& MNDVI < 0.08 \\
& Rat_2 > 0.005
\end{aligned}$$

Here  $BT_{M12}$ ,  $BT_{M15}$  and  $BT_{M16}$  are brightness temperature at M12, M15 and M16, respectively.  $R_{M9}$  is the reflectance at M9.  $Rat_2$  and  $MNDVI$  are defined in section 3.4.2. If all tests shown above are passes, thin dust (1) is detected for the processed pixel.

Or, if :

$$\begin{aligned}
& BT_{M12} - BT_{M15} \geq 20K \\
& \text{thin dust (2) is also identified for the processed pixel}
\end{aligned}$$

#### (4) Thick dust detection

For detection of thick dust, the following spectral contrast in the visible wavelength and brightness temperature difference are applied:

$$\begin{aligned}
& BT_{M15} - BT_{M16} \leq -0.2K \\
& BT_{M12} - BT_{M15} \geq 20K \\
& R_{M9} < 0.035 \\
& MNDVI < 0.2
\end{aligned}$$

Here  $BT_{M12}$ ,  $BT_{M15}$  and  $BT_{M16}$  are brightness temperature at M12, M15 and M16, respectively.  $R_{M9}$  is the reflectance at M9.  $MNDVI$  is defined in section 3.4.2. If all tests shown above are passes, thick dust is detected for the processed pixel.

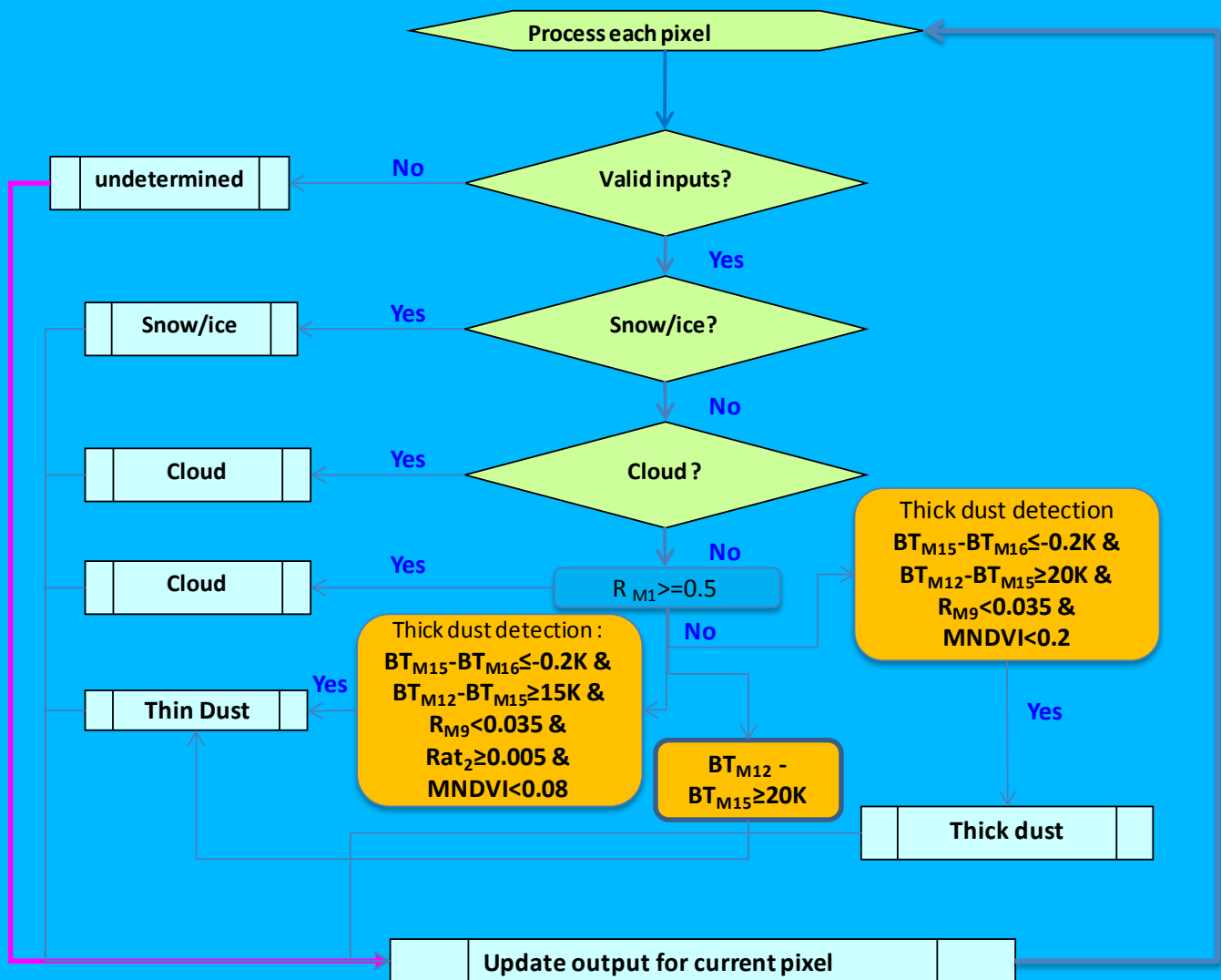


Figure 11: Detail Flow chart of IR-Visible based dust detection over land.

### 3.4.2.2.2 Deep-blue based dust detection

Figure 12 is a flow chart of the algorithm to detect the presence of dust over land during daytime (defined as solar zenith angle less than or equal to  $87^\circ$  degrees). The tests are not performed over snow and ice or in the presence of clouds.

The specific tests as currently implemented are:

(1) Test for the presence of snow/ice by using both primary snow/ice mask and internal snow/ice mask, which is given in section 3.4.2.1. Test for the presence of clouds relies on cirrus cloud tests in VIIRS cloud mask and reflectance at M1. Pixel is considered to be obscured by clouds if any of these three cloud tests in Table 10, i.e. pCirrus1, pCirrus2 and pCirrus3, is true, or  $R_{M1} \geq 0.5$ . Any pixel with the presence of snow/ice or clouds is not processed.

(2) Test for the quality of the input radiance data

- $R_{M1}, R_{M2}, R_{M8}, R_{M11} > 0.0$  &
- VIIRS quality flags for above channels equal to zero, indicating quality of the data is assured.

(2) Bright surface test

- $R_{M8}, R_{M11} > 0.0$  &
- VIIRS quality flags for above channels equal to zero, indicating quality of the data is assured.

$$Bridx = \frac{(R_{M8} - R_{M11})}{(R_{M8} + R_{M11})} \quad (4)$$

If  $Bridx < 0.05$  or  $R_{M11} > 0.25$  then the pixel is considered as a bright pixel.

(3) Dust detection: AAI and DSDI tests – check for pixels with dust

If  $AAI > 11.5$  and  $DSDI \geq 0.0$ , dust exists for the pixel. Once dust is detected for the pixel, dust flag is set and the value of the Dust Aerosol Index (DAI), which is associated with the intensity of the dust, is obtained by scaling AAI as following:

$$DAI = AAI - 11.5 \quad (5)$$

(5) Residual cloud test

Residual cloud contamination is determined by standard deviation of  $R_{M1}$  ( $StdR_{M1}$ ) in a 3 by 3 box centered with the processed pixel. If  $StdR_{M1} \geq 0.01$ , residual cloud exists for the processed and it is assigned as cloudy.

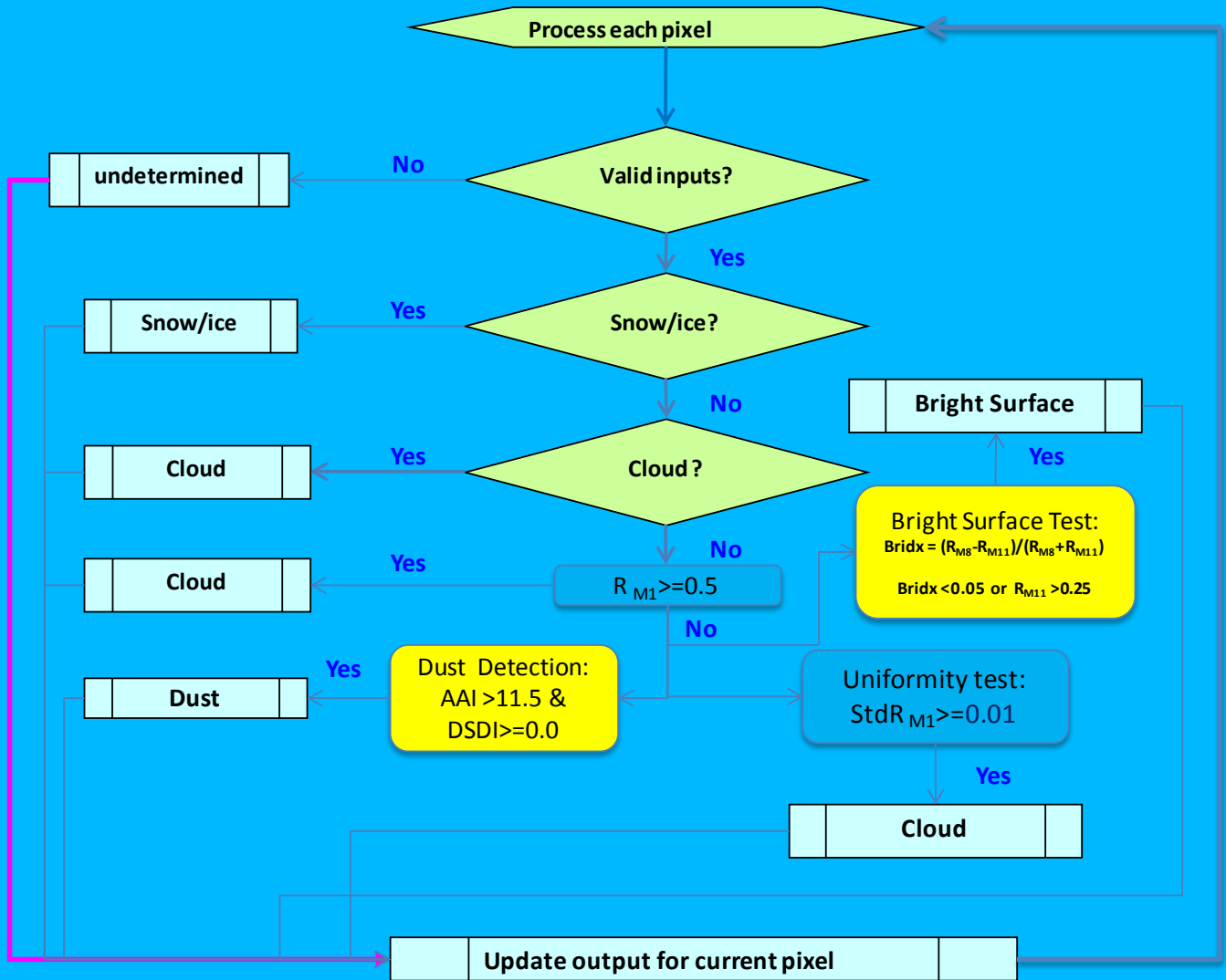


Figure 12: Detail Flow chart of deep-blue based dust detection over land.

### 3.4.2.2.3 Determination of quality and confidence flags

As shown in Section 2.1, dust detection quality flags (00/10/11) are defined as low, medium and high confidence, respectively. Determination of the level of confidence in quality flag relies on several following steps:

1. If the pixel is determined as bright surface, masked as confident adjacent cloud or cloud shadow in cloud mask, then the dust flag detected in this pixel is assigned with a quality flag value of 00, i.e., low confidence
2. The magnitude of AAI and DSDI are also used to assess the quality of detection.

In general, there are two types of test, i.e., 1). Value of the test < threshold. 2). Value of the test > threshold. Details descriptions on how the confidence value (given as Con\_value) is assigned for each type of tests are given as following:

**Test type 1:** used if test looks like  $value < threshold$  or  $value \leq threshold$

The Con\_value is calculated as following:

If  $(threshold - value) < value_1$  then  $Con\_value = 0.0$

If  $value_1 \leq (threshold - value) < value_2$  then  $Con\_value = 0.5$

If  $(threshold - value) \geq value_2$  then  $Con\_value = 1.0$

Where  $value_1$  is  $0.05 \times threshold$ ,  $value_2$  is  $0.30 \times threshold$ . However, under the circumstance that the threshold is 0.0,  $value_1$  and  $value_2$  is assigned with values of 0.05 and 0.3, respectively.

**Test type 2:** used if looks like  $value > threshold$  or  $value \geq threshold$

The Con\_value is calculated as following:

If  $(value - threshold) < value_1$  then  $Con\_value = 0.0$

If  $value_1 \leq (value - threshold) < value_2$  then  $Con\_value = 0.5$

If  $(value - threshold) \geq value_2$  then  $Con\_value = 1.0$

Where  $value_1$  is  $0.05 \times threshold$ ,  $value_2$  is  $0.30 \times threshold$ . However, under the circumstance that the threshold is 0.0,  $value_1$  and  $value_2$  is assigned with values of 0.05 and 0.3, respectively.

**Test type 3:** used if looks like: upper threshold ( $<$  or  $\leq$ ) value ( $<$  or  $\leq$ ) lower threshold

The Con\_value is calculated as following:

$$dv = \frac{(upper\ threshold - lower\ threshold)}{3}$$

If  $value < threshold_{lower} + dv$   
or  $(threshold_{upper} - dv < value)$  then  $Con\_value = 0.0$

If  $(threshold_{lower} + dv \leq value \leq threshold_{upper} - dv)$  then  $Con\_value = 1.0$

Once Con\_value is calculated for individual test, the ensemble confidence value is then calculated by averaging the confidence value for all the tests. Final confidence level is determined by the ensemble confidence value. i.e., high confidence for ensemble confidence value  $\geq 0.66$ , low confidence for

ensemble confidence value  $\leq 0.33$ , medium confidence for ensemble confidence value  $> 0.33$  and  $< 0.66$ . Details on the determination of confidence level for dust detection over land are given as following:

- a. For deep-blue dust detection as shown in section 3.4.2.2.2

Test1:  $AAI \geq 11.5$   
 Test2:  $DSDI \geq 0.0$

Intermediate confidence value ( $con\_value_a$ ) is calculated by averaging the  $con\_value$  for Test1 and Test2 as following:

$$con\_value_a = \frac{con\_value(Test1) + con\_value(Test2)}{2} \quad (6)$$

- b. For IR and visible-based dust detection shown in section 3.4.2.2.1

1. Thin dust (1):

Test 1:  $BT_{M15} - BT_{M16} \leq -0.2K$   
 Test 2:  $BT_{M12} - BT_{M15} \geq 15K$   
 Test 3:  $MNDVI < 0.08$

Intermediate confidence value ( $con\_value_b$ ) is calculated by averaging the  $con\_value$  for Test1 Test2, and Test3 as following:

$$con\_value_b = \frac{con\_value(test1) + con\_value(test2) + con\_value(test3)}{3} \quad (7)$$

2. Thin dust (2):

Test 1:  $BT_{M12} - BT_{M15} \geq 20K$

Intermediate confidence value ( $con\_value_b$ ) is equal to the  $con\_value$  of Test1 as following:

$$con\_value_b = con\_value(test1) \quad (8)$$

3. Thick dust

Test1 :  $BT_{M15} - BT_{M16} \leq -0.2K$   
 Test2 :  $BT_{M12} - BT_{M15} \geq 20K$   
 Test3 :  $MNDVI < 0.2$

Intermediate confidence value ( $con\_value_b$ ) is calculated by averaging the  $con\_value$  for Test1 Test2, and Test3 as following:

$$con\_value_b = \frac{con\_value(test1) + con\_value(test2) + con\_value(test3)}{3} \quad (9)$$

Ensemble confidence value is finally calculated by summing up the  $con\_value_a$  and  $con\_value_b$ .

### 3.4.2.2.4 Example result

The results of an application of the JPSS SM algorithm to S-NPP VIIRS data on September 14, 2013 at around 20:20 UTC is shown in Figure 13. The top panel the figure is a red-green-blue (RGB) false color image of the scene showing the location of the dust outbreak. The bottom panel of the figure shows the results of the smoke/dust detection. Pixels flagged as dusty are colored as yellow to brown, which is scaled with AAI values, as shown in equation 5. A second example is given in Figure 13.

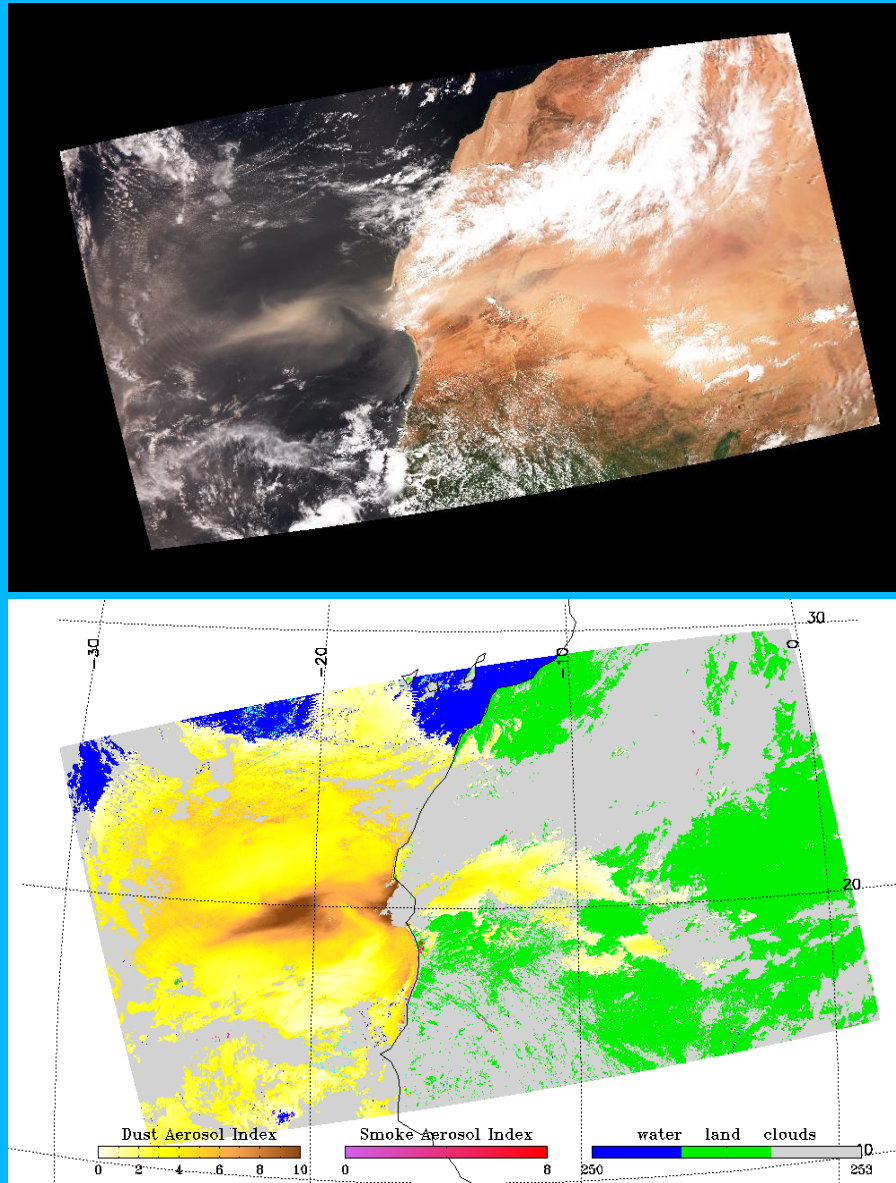


**Figure 13: Top: a red-green-blue (RGB) false color image of S-NPP observation data on September 14, 2013 at approximate 20:20 UTC. Bottom: the results of the dust detection where pixels flagged as dusty are colored as yellow to brown, scaled by DAI.**

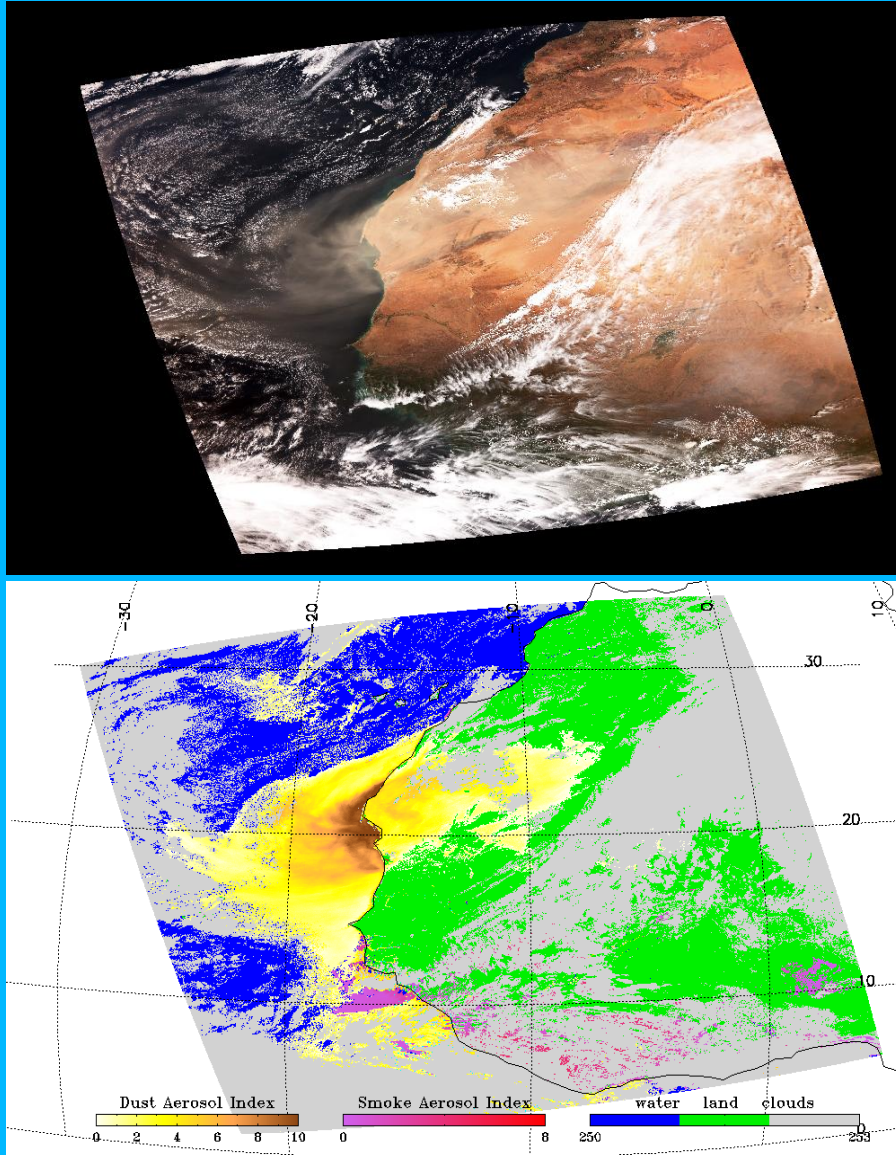


**Figure 14: Top: a red-green-blue (RGB) false color image of S-NPP observation data on December 14, 2013 at approximate 19:55 UTC. Bottom: the results of JPSS ADP algorithm where pixels flagged as dusty are colored as yellow to brown, scaled by DAI; pixels flagged as smoke are colored as pink to red, scaled by SAI.**



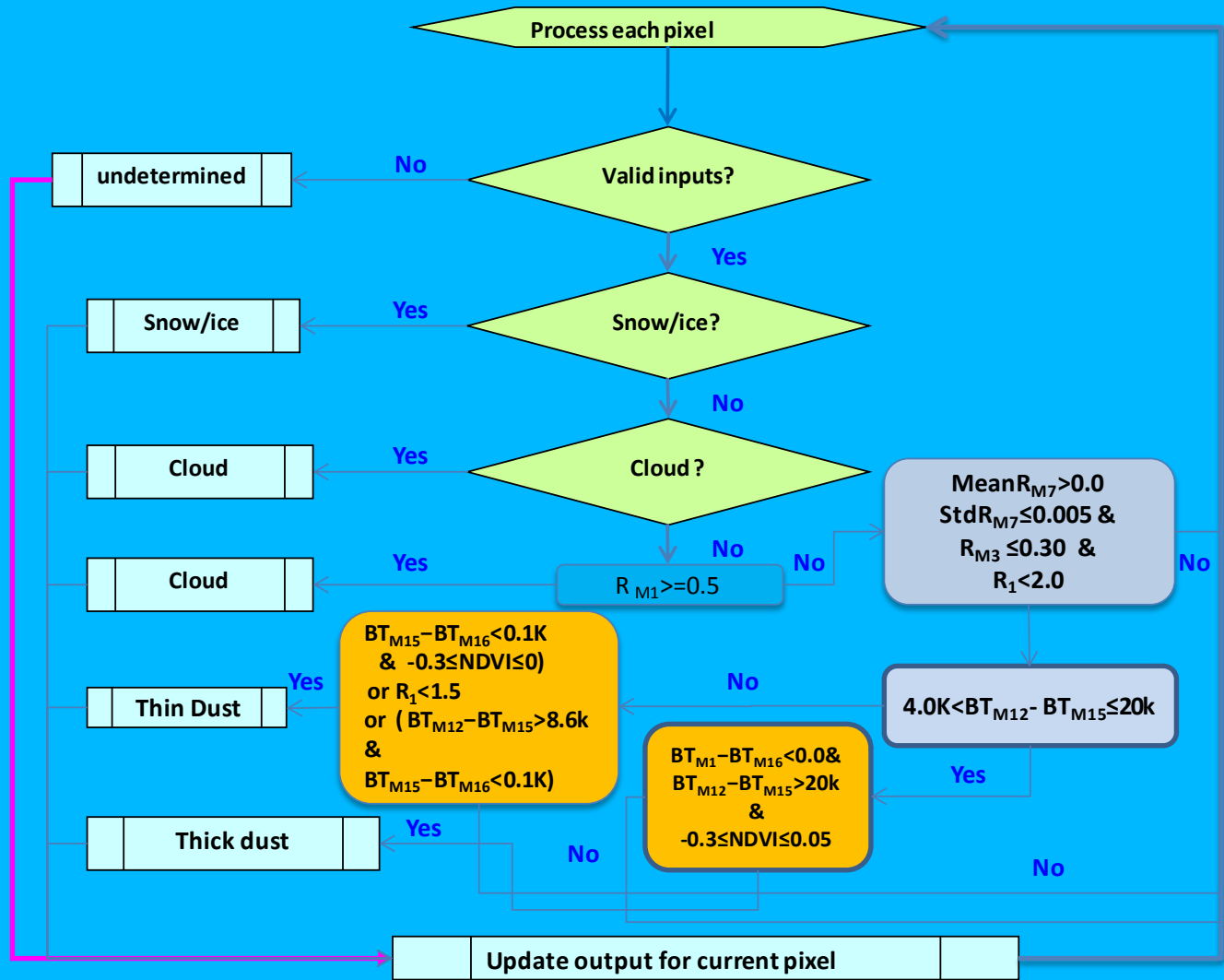


Figure 15: Detailed flow chart of IR-visible based dust detection over water

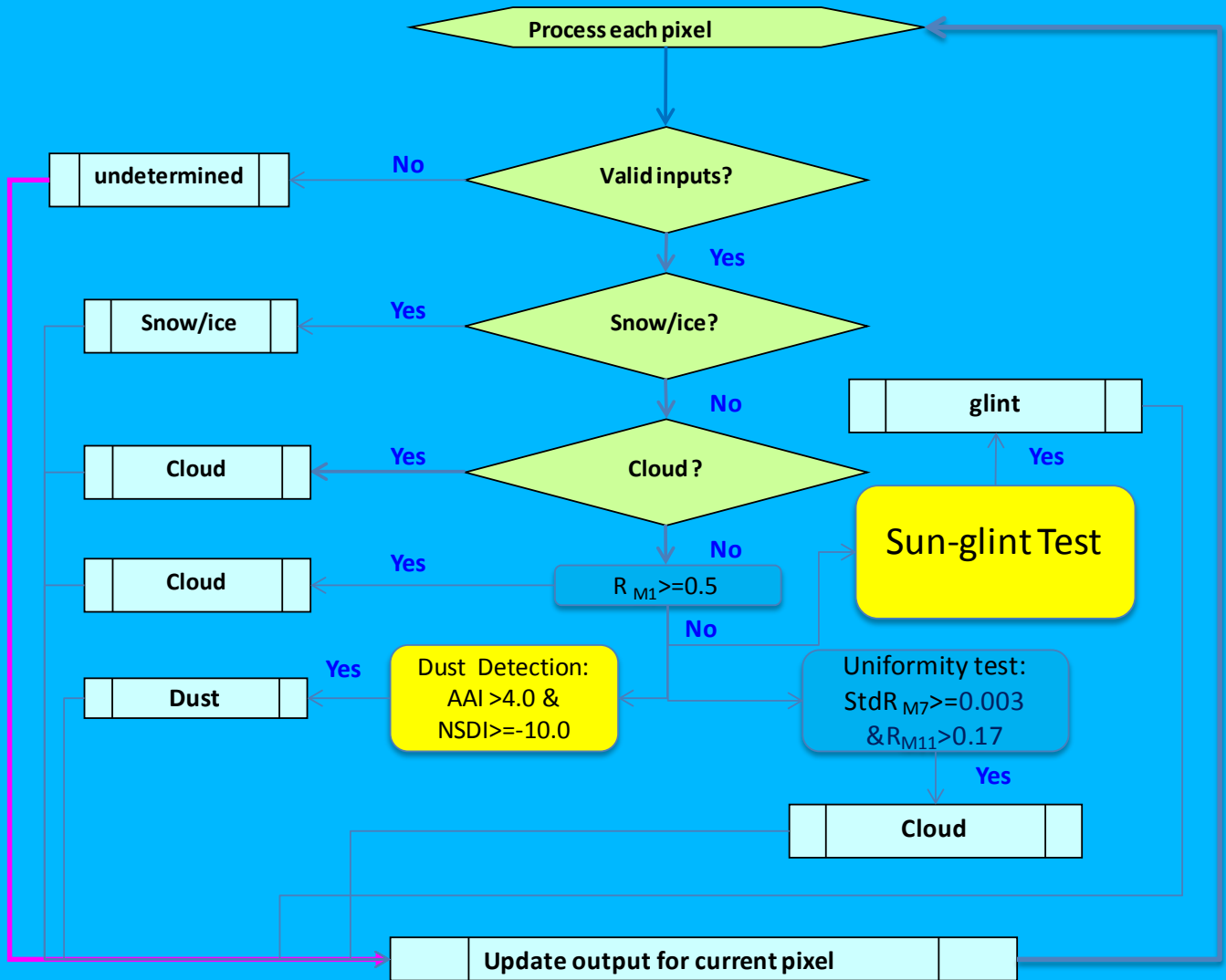


Figure 16: Detailed flow chart of deep-blue dust detection over water.

### 3.4.2.3 Dust Detection over Water

Dust detection over water has also two paths. If either path identifies the presence of dust, then dust is shown to be present in the product. The first path is the same algorithm as for GOES-R Advance Baseline Imager (ABI) to detect dust over land, which is based on the spectral variability tests at visible bands and negative brightness temperature difference between two wavelengths in IR regions; the second one is designed for VIIRS, by taking advantage of observations of VIIRS at deep-blue bands. The path is determined by the availability of channels, if no deep-blue channels, as M1 and M2 for VIIRS, are available, the algorithm only takes the first path. Otherwise, both paths are taken.

#### 3.4.2.3.1 IR and visible-based dust detection

Figure 15 is a detailed flow chart of the algorithm to detect the presence of dust over water during the daytime. The tests are not performed over snow and ice or in the presence of ice clouds.

The specific tests as currently implemented are

1) Test for the presence of snow/ice by using both primary snow/ice mask and internal snow/ice mask, which is given in section 3.4.2.1. Test for the presence of clouds relies on VIIRS cloud mask. Pixel is considered to be obscured by clouds if any one of these two cloud mask tests in Table 10, i.e., pCirrus2 and pFlag1, is true. Any pixel with positive snow/ice or clouds is not processed.

2) Test for the quality of the input radiance data

- $R_{M3}, R_{M5}, R_{M7} > 0.0$  &
- $BT_{M12}, BT_{M15}, BT_{M16} > 0.0K$
- VIIRS quality flags for above channels equal to zero, indicating quality of the data is assured.

3) Uniformity and spectral tests for residual clouds

- $MeanR_{M7} > 0.0$  and  $StdR_{M7} \leq 0.005$  &
- $R_{M3} \leq 0.3$  &
- $R_1 < 2.0$

4) Tests for dust

First of all, test show bellow determines which path to take:

$$4K < BT_{M12} - BT_{M15} \leq 20k$$

If the above test is passed then proceed to thin dust test(4.1), otherwise proceed to thick dust test (4.2).

4.1 thin dust test

For thin dust test, the following tests are applied:

$$BT_{M15} - BT_{M16} \leq 0.1k \text{ and } -0.3 \leq NDVI \leq 0.0$$

$$R_1 < 1.5$$

$$BT_{M12} - BT_{M15} > 8.6k \text{ and } BT_{M15} - BT_{M16} < 0.1k$$

if any one of them is satisfied, then thin dust is detected for the processed pixel.

4.2 thick dust test

For thick dust detection, flowing test are applied:

$$BT_{M11} - BT_{M15} > 20K$$

$$-0.3 \leq NDVI \leq 0.05$$

$$BT_{M15} - BT_{M16} < 0.0K$$

if all of them are satisfied, then thick dust is detected for the processed pixel.

- 5) Set dust mask flag

### 3.4.2.3.2 Deep-blue dust detection over water

Figure 16 is a detailed flow chart of the algorithm to detect the presence of dust over water during the daytime. The tests are not performed over snow and ice or in the presence of clouds.

The specific tests as currently implemented are

- 6) Test for the presence of snow/ice by using primary snow/ice mask, and if the primary is not available, then using secondary snow/ice mask. Test for the presence of clouds relies on VIIRS cloud mask and reflectance at M1. Pixel is considered to be obscured by clouds if any of these three cloud mask tests in Table 10, i.e. pCirrus1, pCirrus2 and pCirrus3, is true, or  $R_{M1} \geq 0.5$ . Any pixel with the presence of snow/ice or clouds is not processed.
- 7) Test for the quality of the input radiance data
  - $R_{M1}, R_{M2}, R_{M7}, R_{M11} > 0.0$  &
  - VIIRS quality flags for above channels equal to zero, indicating quality of the data is assured.
- 8) Dust detection: AAI and DSDI tests – check for pixels with dust

If  $AAI > 4.0$  and  $DSDI \geq -10.0$ , dust exists for the pixel. Once dust is detected for the pixel, dust flag is set and the value of the Dust Aerosol Index (DAI), which is associated with the intensity of the dust, is obtained by scaling AAI as following:

$$DAI = AAI - 4.0 \quad (10)$$

- 9) Uniformity and spectral tests for residual clouds

If  $StdR_{M7} \geq 0.003$  and  $R_{M11} > 0.17$  then residual cloud exists and the pixel is assigned as cloudy.

### 3.4.2.3.3 Determination of quality and confidence flags

The approach to determine the quality flag with confidence value is the similar to what has described in section 3.4.2.2.1. . Dust detection quality flag (00/10/11) are defined as lower, medium and high confidence, respectively. Determination of the level of confidence in quality flag relies on several following steps:

1. If the pixel is masked as confident adjacent cloud or cloud shadow in cloud mask, or within the sun glint, then the dust flag detected in this pixel is assigned a quality flag with an value of 00, i.e., low confidence
2. If the pixel detected having dust passed through step 1, then the confidence of this detection is further determined by closeness of both AAI and DSDI to their threshold. The details on how to calculate the confidence values for individual tests and ensemble confidence value are given in section 3.4.2.2.1.

- a. For deep-blue dust detection as shown in section 3.4.2.3.2

Test1:  $AAI > 4.0$   
 Test2:  $DSDI \geq -10.0$

Intermediate confidence value ( $con\_value_a$ ) is calculated by averaging the  $con\_value$  for Test1 and Test2 as following:

$$con\_value_a = \frac{con\_value(Test1) + con\_value(Test2)}{2} \quad (11)$$

- b. For IR and visible-based dust detection shown in section 3.4.2.2.1

1. Thin dust (1):

Test 1:  $BT_{M15} - BT_{M16} \leq -0.1K$   
 Test 2:  $-0.3 \leq NDVI \leq 0.0$   
 Test 3:  $BT_{M12} - BT_{M15} > 8.6k$

Intermediate confidence value ( $con\_value_b$ ) is calculated by averaging the  $con\_value$  for Test1 Test2, and Test3 as following:

$$con\_value_b = \frac{con\_value(test1) + con\_value(test2) + con\_value(test3)}{3} \quad (12)$$

2. Thin dust (2):

Test 1:  $4K < BT_{M12} - BT_{M15} \leq 20k$   
 Test2:  $R_1 < 1.5$

Intermediate confidence value ( $con\_value_b$ ) is calculated by averaging the  $con\_value$  for Test1 and Test2 as following: as following:

$$con\_value_b = \frac{con\_value(test1) + con\_value(test2)}{2} \quad (13)$$

- Thick dust

$$\text{Test1} : BT_{M15} - BT_{M16} \leq -0.2K$$

$$\text{Test2} : BT_{M12} - BT_{M15} \geq 20K$$

$$\text{Test3} : MNDVI < 0.2$$

Intermediate confidence value ( $con\_value_b$ ) is calculated by averaging the  $con\_value$  for Test1, Test2, and Test3 as following:

$$con\_value_b = \frac{con\_value(test1) + con\_value(test2) + con\_value(test3)}{3} \quad (14)$$

Ensemble confidence value is calculated by summing up the  $con\_value_a$  and  $con\_value_b$ . Final confidence level is set as low if ensemble confidence value is  $\leq 0.25$ ; confidence level is set as medium if ensemble confidence value is  $> 0.25$  but  $< 0.50$ ; confidence level is set as high if ensemble confidence value is  $\geq 0.50$ .

#### 3.4.2.3.4 Example results

The results of an application of the JPSS ADP algorithm to S-NPP VIIRS data on February 1, 2015 at approximate 11:25 to 11:28 UTC is shown in Figure 17. The top panel is a RGB images. The image at the bottom panel shows the results of the water and land dust detection algorithm, where orange and brown regions indicate the presence of dust. It is clearly see that the RGB image and the JPSS ADP dust mask image show qualitative agreement.

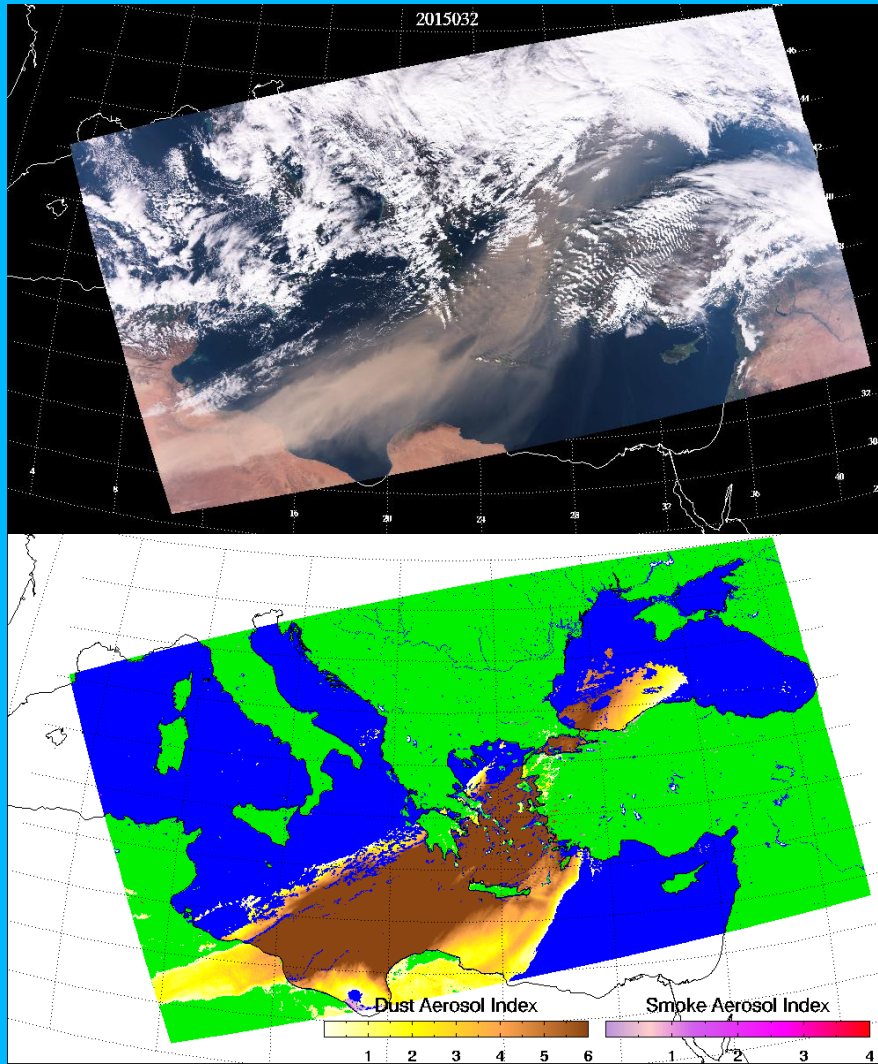


*Figure 17: S-NPP VIIRS observations on Feb 1, 2015 at approximate 11:25 to 11:28 UTC. A dust outbreak is flowing from the Sahara desert over the adjacent Mediterranean Ocean.*

### 3.4.2.4 Smoke Detection over Land

Smoke detection over land has two paths. If either path identifies the presence of smoke, then smoke is shown to be present in the product. The first path is the same algorithm as for GOES-R Advance Baseline Imager (ABI) to detect thick smoke, which is based on the spectral variability tests at visible bands; the second one is designed for VIIRS, by taking advantage of observations of VIIRS at deep-blue bands. Figure 18 is a detailed flow chart of the first algorithm to detect the presence of smoke over land during daytime. A detailed flow chart of the second algorithm to detect the presence of smoke over land during daytime is given in Figure 15: Detailed flow chart of thick smoke detection over land. Note that, the tests are not performed in the presence of snow/ice and ice clouds

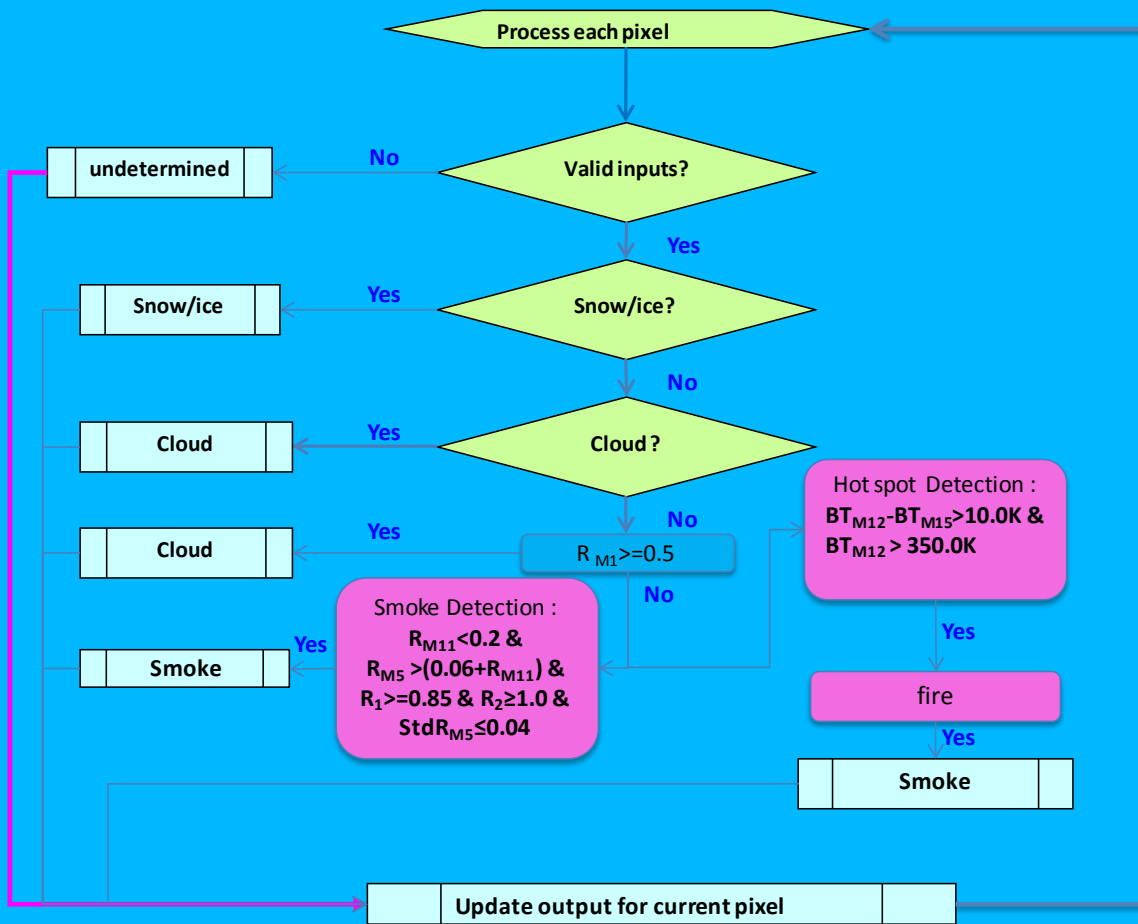


Figure 18: Detailed flow chart of IR-Visible based smoke detection over land.

### 3.4.2.4.1 IR-Visible based smoke detection

Figure 14 is a detailed flow chart of the first algorithm to detect the presence of smoke over land during daytime.

The specific tests as currently implemented sequentially are:

- 1) Test for the presence of snow/ice by using primary snow/ice mask, and if the primary is not available, then using secondary snow/ice mask. Test for the presence of clouds relies on VIIRS cloud mask. Pixel is considered to be obscured by clouds if any of these five cloud mask tests in Table 10, i.e. pCirrus1, pCirrus2, pCirrus3, pFlag1 and, pFlag2, is true. Any pixel with the presence of snow/ice/clouds is not processed.
- 2) Test for the quality of the input reflectance data
  - $R_{M3}, R_{M5}, R_{M7}, R_{M11} > 0.0$  &
  - $BT_{M13}, BT_{M15} > 0.0K$
  - VIIRS quality flags for above channels equal to zero, indicating quality of the data is assured.



3) Fire detection (hot spot)

Fire hot spot is determined by the combination of brightness temperature at  $M_{13}$  ( $BT_{M_{13}}$ ) and the brightness temperature difference between  $M_{13}$  and  $M_{15}$  ( $BT_{M_{13}} - BT_{M_{15}}$ ). If  $BT_{M_{13}} > 360K$  and  $BT_{M_{13}} - BT_{M_{15}} > 10K$ , then the processed pixel is indicated having fire.

4) Spectral and uniformity tests for thick smoke

For detection of thick smoke, the following spectral contrast and uniformity tests are applied:

$$\begin{aligned}R_{M_{11}} &< 0.2 \\R_{M_5} &> (0.06 + R_{M_{11}}) \\R_1 &\geq 0.85 \\R_2 &\geq 1.0 \\StdR_{M_5} &\leq 0.04\end{aligned}$$

Where  $R_{M_{11}}$  and  $R_{M_5}$  are reflectance at  $M_{11}$  and  $M_5$ , respectively.  $R_1$  and  $R_2$  are spectral contrast defined in section 3.4.2.  $StdR_{M_5}$  is the standard deviation of  $R_{M_5}$  in a 3 by 3 box centered with the processed pixel.

If all tests shown above are passes, thick smoke is detected for the processed pixel.

5) Set smoke flag

- If fire or thick smoke is indicated in the process pixel, then thick smoke flag is set

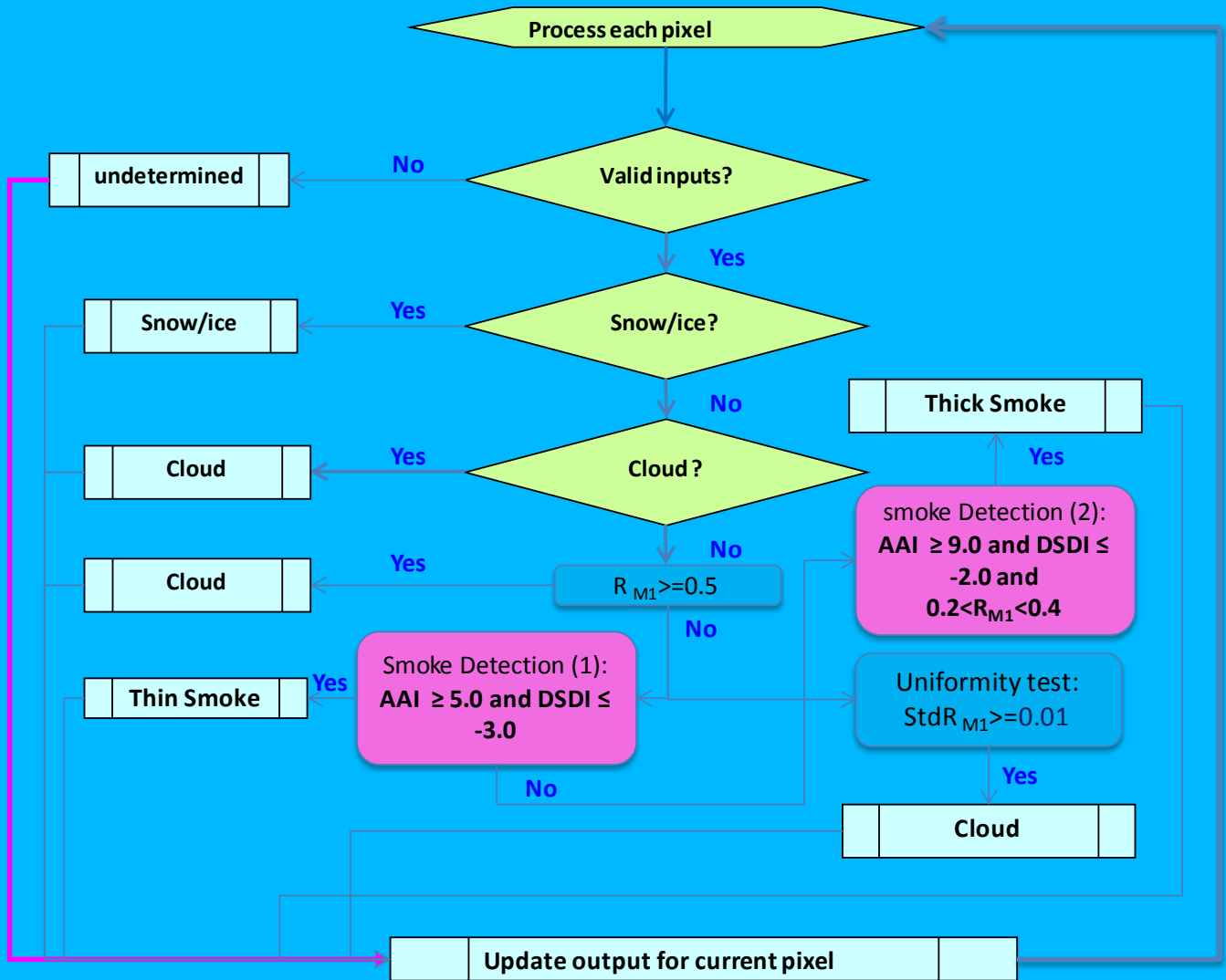


Figure 19: Detailed flow chart of deep-blue smoke detection over land

### 3.4.2.4.2 Deep-blue smoke detection

The specific tests as currently implemented are:

- 1) Test for the presence of snow/ice by using primary snow/ice mask, and if the primary is not available, then using secondary snow/ice mask. Test for the presence of clouds relies on VIIRS cloud mask and reflectance at M1. Pixel is considered to be obscured by clouds if any of these three cloud mask tests in Table 10, i.e. pCirrus1, pCirrus2 and pCirrus3, is true, or  $R_{M1} \geq 0.5$ . Any pixel with the presence of snow/ice or clouds is not processed.
- 2) Test for the quality of the input radiance data

- $R_{M1}, R_{M2}, R_{M7}, R_{M11} > 0.0$  &

- VIIRS quality flags for above channels equal to zero, indicating quality of the data is assured.

3) Smoke detection: AAI and DSDI tests – check for pixels with thin/thick dust

If  $AAI > 5.0$  and  $DSDI \leq -3.0$ , thin smoke exists for the processed pixel. However, If  $AAI > 9.0$  and  $DSDI \leq -2.0$  and  $0.2 < R_{MI} < 0.4$ , then thick smoke exists for the processed pixel. Once smoke (either thin or thick) is detected for the pixel, smoke flag is set and the value of the Smoke Aerosol Index (SAI), which is associated with the intensity of the smoke, is obtained by scaling AAI as following:

$$SAI = AAI - 5.0 \quad (15)$$

4) Uniformity and spectral tests for residual clouds

If the processed pixel is identified as having smoke from above steps, but  $StdR_{MI} \geq 0.01$ , then residual cloud exists and the processed pixel is assigned as cloudy.

### 3.4.2.4.3 Determination of quality and confidence flags

The approach to determine the quality flag with confidence value is the similar to what has described in section 3.4.2.2.1. . Smoke detection quality flag (00/10/11) are defined as lower, medium and high confidence, respectively. Determination of the level of confidence in quality flag relies on several following steps:

1. If the pixel is masked as confident adjacent cloud or cloud shadow in cloud mask, then the smoke flag detected in this pixel is assigned a quality flag with an value of 00, i.e., low confidence
2. If the pixel detected having smoke passed through step 1, then the confidence of this detection is further determined by closeness of tests to their threshold. The details on how to calculate the confidence values are given in section 3.4.2.2.1.

c. For Deep-blue smoke detection (3) as shown in section 3.4.2.3

For thin smoke:

Test1:  $AAI > 5.0$   
 Test2:  $DSDI \leq -3.0$

For thick smoke:

Test1:  $AAI > 9.0$

Test2: DSDI  $\geq$  -2.0

Intermediate confidence value ( $con\_value_a$ ) is calculated by averaging the  $con\_value$  for Test1 and Test2 as following:

$$con\_value_a = \frac{con\_value(Test1) + con\_value(Test2)}{2} \quad (16)$$

d. For thick-smoke detection shown in section 3.4.2.4.1

1) Smoke from fire as shown in section 3.4.2.4

Test1:  $BT_{M13} > 350K$

Test2:  $BT_{M13} - BT_{M15} > 10K$

Intermediate confidence value ( $con\_value_b$ ) is calculated by averaging the  $con\_value$  for Test1 and Test2 as following:

$$con\_value_b = \frac{con\_value(Test1) + con\_value(Test2)}{2} \quad (17)$$

2) Thick smoke as shown in section 3.4.2.4

Test1:  $R_{M11} < 0.2$

Test2:  $R_{M5} > (0.06 + R_{2.25\mu m})$

Test3:  $R_1 \geq 0.85$

Test4:  $R_2 \geq 1.0$

Intermediate confidence value ( $con\_value_b$ ) is calculated by averaging the  $con\_value$  for Test1, Test2, Test3 and Test4 as following:

$$con\_value_b = \frac{con\_value(Test1) + con\_value(Test2) + con\_value(Test3) + con\_value(Test4)}{4} \quad (18)$$

e. Ensemble confidence

Ensemble confidence value is calculated by summing up  $con\_value_a$  and  $con\_value_b$ . Then, confidence level for quality flag is set as low if ensemble confidence value is  $\leq 0.33$ ; confidence level is set as medium if ensemble confidence value is  $> 0.33$  but  $< 0.66$ ; confidence level is set as high if ensemble confidence value is  $\geq 0.66$ .

#### 3.4.2.4.4 Example result

The result of an application of the smoke detection to S-NPP VIIRS observations on August 3, 2014 at 20:10 UTC is shown Figure 20. Smoke over west coast of U.S. is detected. Comparison of smoke mask to RGB images shows that smoke over land was well captured.

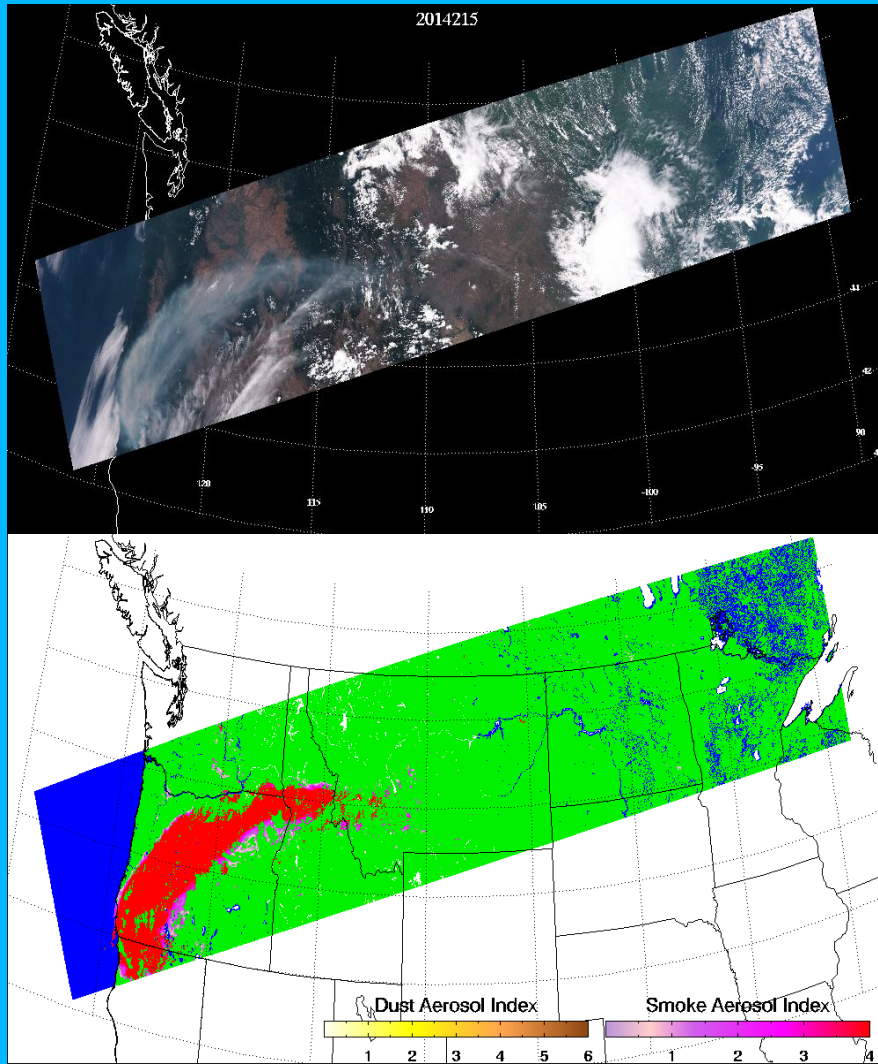


**Figure 20:** Top: a red-green-blue (RGB) false color image of S-NPP VIIRS observation data on August 3, 2014 at approximate 20:10 UTC. Bottom: the results of the smoke detection where pixels flagged as smoky are pink to red.

### 3.4.2.5 Smoke detection over water

Smoke detection over water has two paths. If either path identifies the presence of smoke, then smoke is shown to be present in the product. The first path is the same algorithm as for GOES-R Advance Baseline Imagery to detection thick smoke, which is based on the spectral variability test at visible bands; the second one is designed for VIIRS, by taking advantage of observations of VIIRS at deep-blue bands. Figure 21 is a detailed flow chart of the first algorithm to detect the presence of smoke over water during daytime. A detailed flow chart of the second algorithm to detect the presence of smoke over water during daytime is given in Figure 22. Note that, the tests are not performed in the presence of snow/ice and ice clouds

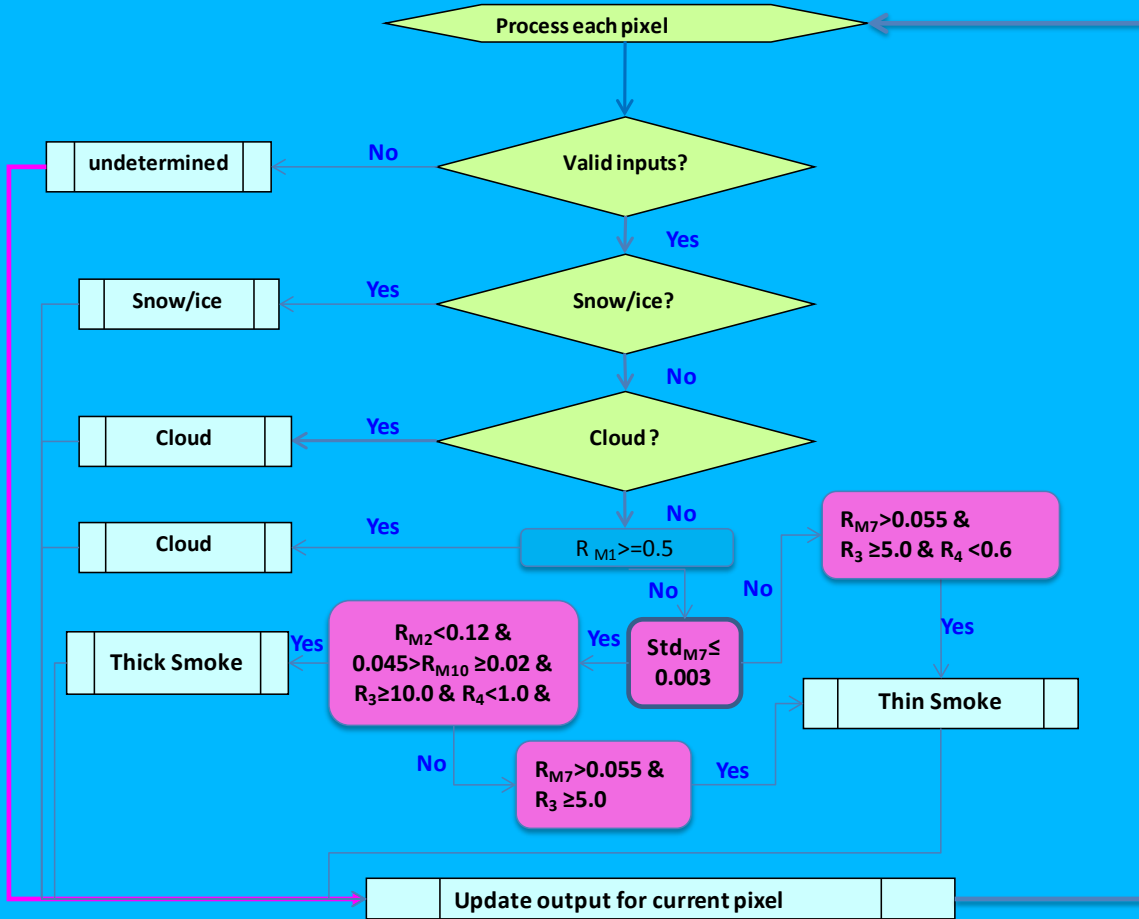


Figure 21: Detailed flow chart of Visible-NIR based smoke detection over water.

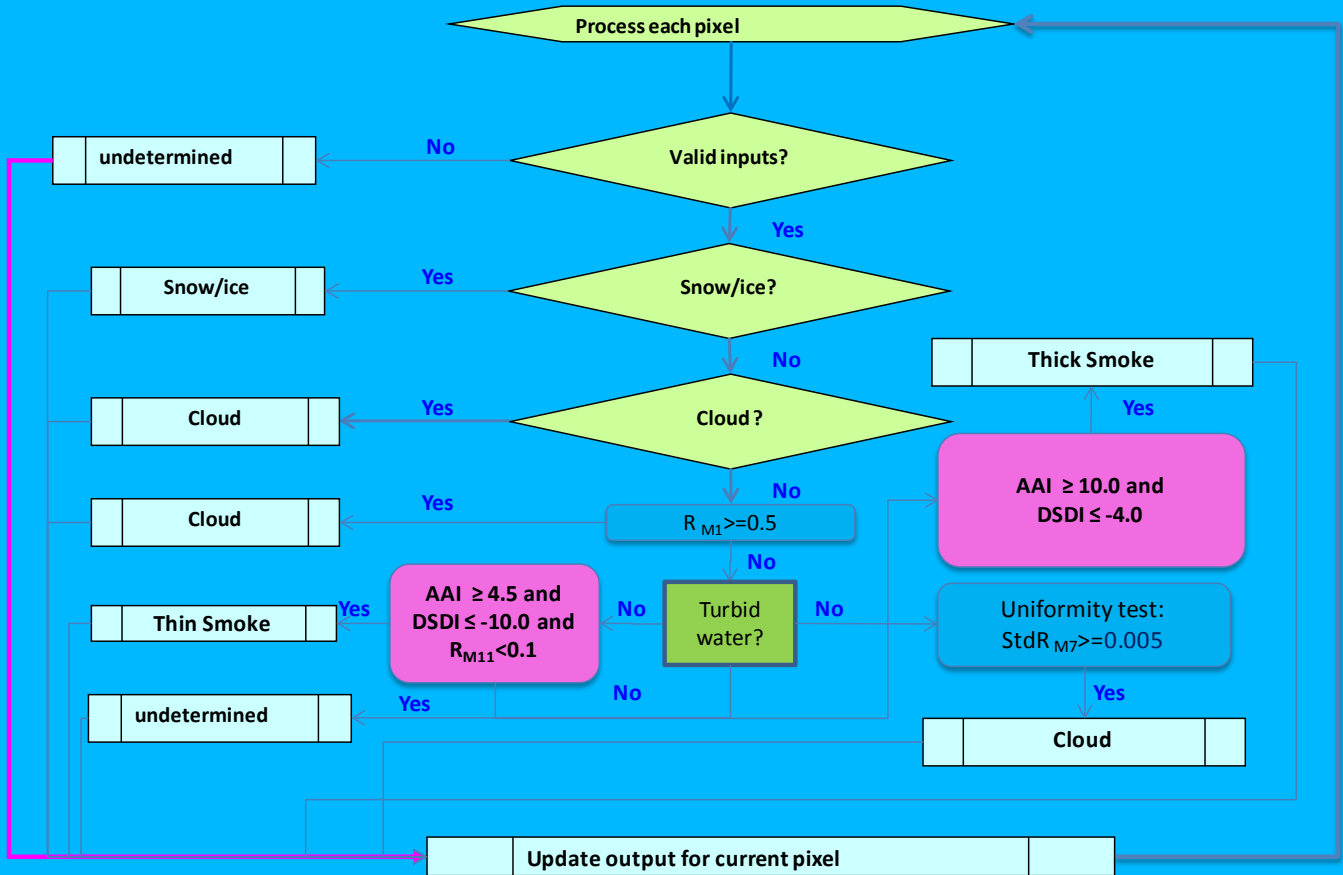


Figure 22: Detailed flow chart of deep-blue smoke detection over water.

### 3.4.2.5.1 Visible-NIR based Smoke detection

The specific tests as currently implemented sequentially are

- 1) Test for the presence of snow/ice by using primary snow/ice mask, and if the primary is not available, then using secondary snow/ice mask. Test for the presence of clouds relies on VIIRS cloud mask. Pixel is considered to be obscured by clouds if any of these four cloud mask tests in Table 10, i.e. pCirrus1, pCirrus2, pCirrus3 and pFlag1, is true. Any pixel with positive snow/ice/cloud mask is not processed.
- 2) Test for the quality of the input radiance data
  - $R_{M2}, R_{M7}, R_{M10}, R_{M11} > 0.0$
  - VIIRS quality flags for above channels equal to zero, indicating quality of the data is assured.
- 3) Uniformity test

Uniformity test with  $\text{Std}R_{M7}$  is first performed to decide the following detection path. If  $\text{Std}R_{M7} \leq 0.003$ , thick smoke determination test is performed. Otherwise, thin smoke determination test is performed.

### 3.1) Thick smoke determination test

Thick smoke is detected for the processed pixel if the all of the following tests are passed:

$$\begin{aligned} R_3 &\geq 10.0 \\ R_{M2} &\geq 0.12 \\ 0.02 &\leq R_{M10} < 0.045 \\ R_4 &< 1.0 \end{aligned}$$

Where  $R_{M2}$  and  $R_{M11}$  are respectively the reflectance at M2 and M11,  $R_3$  and  $R_4$  are spectral contrast defined in section 3.4.2.

If above tested are not passed, then further tests are performed, and thin smoke is identified if the all of the following tests are passed:

$$\begin{aligned} R_{M7} &> 0.055 \\ R_3 &\geq 5.0 \end{aligned}$$

Where  $R_{M7}$  is the reflectance at  $M_7$ ,  $R_3$  is spectral contrast defined in section 3.4.2.

### 3.2). thin smoke determination test

Thin smoke is detected for the processed pixel if the all of the following tests are passed:

$$\begin{aligned} R_{M7} &> 0.055 \\ R_3 &\geq 5.0 \\ R_4 &< 0.6 \end{aligned}$$

Where  $R_{M7}$  is the reflectance at  $M_7$ ,  $R_3$  and  $R_4$  are spectral contrast defined in section 3.4.2.

### 4) Set smoke flag

If either thin or thick smoke is detected for the processed pixel, then smoke flag is set.

## 3.4.2.5.2 Deep-blue smoke detection

The specific tests as currently implemented are:

- 1) Test for the presence of snow/ice by using primary snow/ice mask, and if the primary is not available, then using secondary snow/ice mask. Test for the presence of clouds relies on VIIRS



cloud mask and reflectance at  $M_1$  ( $R_{M1}$ ) Pixel is considered to be obscured by clouds if any of these three cloud mask tests in Table 10, i.e. pCirrus1, pCirrus2 and pCirrus3, is true, or  $R_{M1} \geq 0.5$ . Any pixel with the presence of snow/ice or clouds is not processed.

2) Test for the quality of the input radiance data

- $R_{M1}, R_{M2}, R_{M7}, R_{M11} > 0.0$  &
- VIIRS quality flags for above channels equal to zero, indicating quality of the data is assured.

3) Turbid/shallow water and algae bloom test

The MODIS heritage turbid/shallow water test described in Li et al. (2003) is used to identify turbid water containing suspended sediments and also shallow water, in which smoke detection will not be carried out to reduce false alarm must. The sediment masking algorithm follows: the observed reflectances at  $M_3, M_8, M_{10}$ , and  $M_{11}$  are used to derive the power law fit using least squares minimization. The computed reflectances ( $R'_{M4}$ ) at  $M_4$  based on the power law fit are then compared with the observed reflectances ( $R_{M4}$ ) at the same band. The specific criteria to trigger that the pixel is affected by turbid water are:

$$\begin{aligned} R_{M4} - R'_{M4} &> 0.015 \\ R_{M3} &< 0.25 \\ R_{M11} &< 0.10 \end{aligned} \quad (19)$$

In addition, for water surface, phytoplankton bloom will be miss-identified as smoke plume by the above smoke detection algorithm. To eliminate this false alarm, any pixel which has phytoplankton bloom, smoke detection will be carried out. To determine if a pixel contains phytoplankton bloom, and index (*SABI*), which is defined as following, is used:

$$SABI = \frac{R_{M4} - R_{M5}}{R_{M4} + R_{M7}} \quad (20)$$

any pixel with an *SABI* value larger than 0.28 is considered as having phytoplankton bloom.

4) Smoke detection: AAI and DSDI tests – check for pixels with thin/thick dust

If  $AAI > 4.5$ ,  $DSDI \leq -10.0$  and  $R_{M11} < 0.1$ , thin smoke exists in the processed pixel. However, If  $AAI > 10.0$  and  $DSDI \leq -4.0$ , thick smoke exists in the processed pixel. Once smoke (either thin or thick) is detected for the pixel, smoke flag is set and the value of the Smoke Aerosol Index (SAI), which is associated with the intensity of the smoke, is obtained by scaling AAI as following:

$$SAI = AAI - 4.5 \quad (21)$$

5) Uniformity and spectral tests for residual clouds

If the processed pixel is identified as having smoke from above steps, but  $\text{StdR}_{M7} \geq 0.005$ , then residual cloud exists and the processed pixel is assigned as cloudy.

### 3.4.2.5.3 Determination of quality and confidence flags

The approach to determine the quality flag with confidence value is the similar to what has described in section 3.4.2.2.1. . Smoke detection quality flag (00/10/11) are defined as lower, medium and high confidence, respectively. Determination of the level of confidence in quality flag relies on several following steps:

3. If the pixel is masked as confident adjacent cloud or cloud shadow in cloud mask, then the smoke flag detected in this pixel is assigned a quality flag with an value of 00, i.e., low confidence
  4. If the pixel detected having smoke passed through step 1, then the confidence of this detection is further determined by closeness of tests to their threshold. The details on how to calculate the confidence values are given in section 3.4.2.2.1.
- f. For Deep-blue smoke detection (3) as shown in section 3.4.2.5.2.  
For thin smoke:

Test1:  $\text{AAI} > 4.5$   
Test2:  $\text{DSDI} \leq -10.0$

For thick smoke:

Test1:  $\text{AAI} > 10.0$   
Test2:  $\text{DSDI} \leq -4.0$

Intermediate confidence value ( $\text{con\_value}_a$ ) is calculated by averaging the  $\text{con\_value}$  for Test1 and Test2 as following:

$$\text{con\_value}_a = \frac{\text{con\_value}(\text{Test1}) + \text{con\_value}(\text{Test2})}{2} \quad (22)$$

- g. For visible-NIR based smoke detection shown in section 3.4.2.5.1

- 1) Thin Smoke (1) as shown in section 3.4.2.5.1

Test1:  $R_3 \geq 5.0$

Intermediate confidence value ( $\text{con\_value}_b$ ) is EQUAL TO  $\text{Con\_value}$  of Test1.

- 2) Thin Smoke (2) as shown in section 3.4.2.5.1

Test1:  $R_3 \geq 5.0$

Test2:  $R_4 < 0.6$

Intermediate confidence value ( $con\_value_b$ ) is calculated by averaging the  $con\_value$  for Test1 and Test2 as following:

$$con\_value_b = \frac{con\_value(Test1) + con\_value(Test2)}{2} \quad (23)$$

3) Thick smoke (3) as shown in section 3.4.2.5.1

Test1:  $R_3 \geq 10.0$

Test2:  $R_{0.47\mu m} \geq 0.12$

Test3:  $0.02 \leq R_{1.61\mu m} < 0.45$

Test4:  $R_4 < 1.0$

Intermediate confidence value ( $con\_value_b$ ) is calculated by averaging the  $con\_value$  for Test1, Test2, Test3 and Test4 as following:

$$con\_value_b = \frac{con\_value(Test1) + con\_value(Test2) + con\_value(Test3) + con\_value(Test4)}{4} \quad (24)$$

h. Ensemble confidence

Ensemble confidence value is calculated by summing up  $con\_value_a$  and  $con\_value_b$ . Then, confidence level for quality flag is set as low if ensemble confidence value is  $\leq 0.33$ ; confidence level is set as medium if ensemble confidence value is  $> 0.33$  but  $< 0.66$ ; confidence level is set as high if ensemble confidence value is  $\geq 0.66$ .

#### 3.4.2.5.4 Example result

The results of an application of the JPSS ADP algorithm to S-NPP VIRRS data on July 11, 2015 at approximate 13:00 UTC is shown in Figure 23. The smoke feature stretched from the east coast of Greenland to the central Atlantic Ocean is shown on RGB image. This ribbon of smoke aloft from forest fires over Russia is transported eastward across the North Atlantic Ocean by the circulation of a large area of low pressure on 17 July 2015. The leading edge of the smoke had moved over the British Isles and was headed toward Scandinavia. It is clear seen that the detected coverage of the smoke is very similar to the pattern that observed from the RGB image, indicating the success of ADP product algorithm.

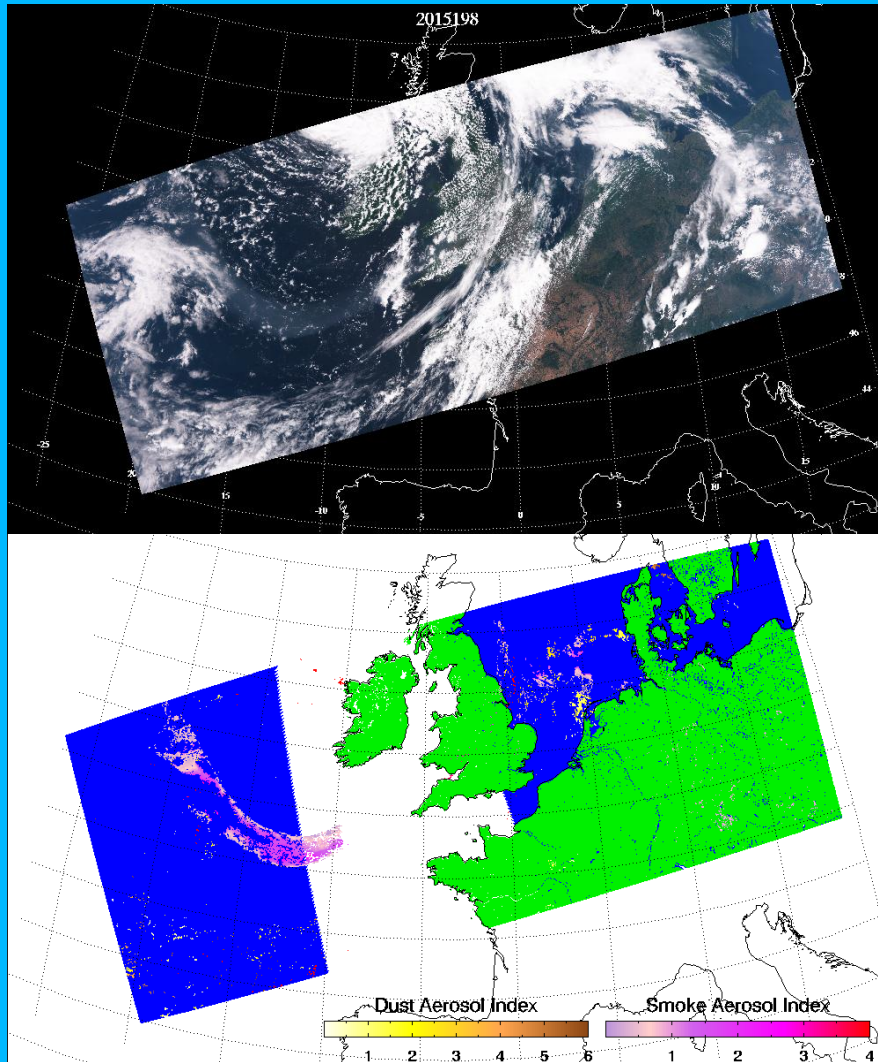


**Figure 23: Top: a red-green-blue (RGB) false color image of S-NPP VIIRS observations on July 11, 2015 at approximate 12:58 UTC. Bottom: the results of ADP product algorithm.**

### 3.4.3 Algorithm Output

The final outputs of this algorithm are both yes/no flag and quality flag for 6 categories, i.e., volcanic ash, clouds, smoke, dust, none/unknown/clear and snow/ice, values for smoke/dust aerosol index (SAI/DAI), non-dust aerosol index (DSDI) and smoke concentration, and quality flags for the parameters are listed below in Table 12.

**Table 12 JPSS ADP algorithm output summary**

Name	Type	Description	Dimension
Volcanic ash flag	Integer	Volcanic ash flag (1/0 - yes/no) Passed down from cloud mask product	grid (xsize, ysize)
Clouds flag	Integer	clouds flag (1/0 - yes/no)	grid (xsize, ysize)
Smoke flag	Integer	smoke flag (1/0 - yes/no)	grid (xsize, ysize)
Dust flag	Integer	Dust flag (1/0 - yes/no)	grid (xsize, ysize)

NUC Flag	Integer	None/Unknown/Clear flag (1/0 – yes/no)	grid (xsize, ysize)
Snow/ice flag	Integer	Snow/Ice flag (1/0 – yes/no)	grid (xsize, ysize)
Quality flag for Detected Volcanic Ash	Binary (2 bits)	Low/Medium/high confidence (10/01/11) for the detected flag (passed down from cloud mask product)	grid (xsize, ysize)
Quality flag for Detected Smoke	Binary (2 bits)	Low/Medium/high confidence (10/01/11) for the detected flag	grid (xsize, ysize)
Quality flag for Detected Dust	Binary (2 bits)	Low/Medium/high confidence (10/01/11) for the detected flag	grid (xsize, ysize)
Quality flag for Detected NUC	Binary (2 bits)	Low/Medium/high confidence (10/01/11) for the detected flag	grid (xsize, ysize)
Smoke Detection algorithm path	Binary (2 bits)	00: Deep-blue based algorithm 00: IR-Visible based algorithm 11: Both algorithm	grid (xsize, ysize)
Dust Detection Algorithm path	Binary (2 bits)	00: Deep-blue based algorithm 00: IR-Visible based algorithm 11: Both algorithm	grid (xsize, ysize)
Dust/smoke Aerosol Index (DAI/SAI)	float	Dust/aerosol index for pixel values with dust/smoke	grid (xsize, ysize)
Non-dust Aerosol Index	float	Non-dust Aerosol index values for pixel with smoke/dust	grid (xsize, ysize)
Smoke Mass concentration	float	Smoke mass concentration ( $\mu\text{g}/\text{m}^3$ ) value for pixel with smoke	grid (xsize, ysize)

In addition the following meta data information is included in the output:

- Product information
  - project
  - naming authority
  - institution
  - standard name vocabulary
  - title and summary
  - processing level
  - version number
  - history
  - reference
- Date and Time
  - product creating time
  - day/night flag
  - granule starting time(Year-Month-Day-hour:minutes:seconds)
  - granule ending time(Year-Month-Day-hour:minutes:seconds)
- Bounding Box
  - Latitude of the first field of view at the first scanline
  - Latitude of the last field of view at the first scanline
  - Latitude of the first field of view at the last scanline
  - Latitude of the lat field of view at the last scanline
  - Longitude of the first field of view at the first scanline
  - Longitude of the last field of view at the first scanline

- Longitude of the first field of view at the last scanline
- Longitude of the lat field of view at the last scanline
- Geospatial bounds
- Satellite
  - Orbit number
  - Ascending/descending flag
- Instrument
- Number of good dust retrievals
- Number of good smoke retrievals
- Total number of attempted retrievals
- Percent of retrievals with Good (determined) smoke retrievals
- Percent of retrievals with Bad (not determined) smoke retrieval
- Percent of retrievals with Good (determined) dust retrievals
- Percent of retrievals with Bad (not determined) dust retrieval
- Percent of retrievals with Low Confidence Smoke Detection
- Percent of retrievals with Medium Confidence Smoke Detection
- Percent of retrievals with High Confidence Smoke Detection
- Percent of retrievals with Low Confidence Dust Detection
- Percent of retrievals with Medium Confidence Dust Detection
- Percent of retrievals with High Confidence Dust Detection

## 4 Test Datasets and Outputs

### 4.1 Proxy Input Data Sets and validation data

#### 4.1.1 Input Data sets

The VIIRS instrument flying on NASA's Suomi-NPP satellites measures radiances at 16 wavelengths including infrared and visible bands with a spatial resolution of 750m at Nadir. The cloud mask is part of the Suomi-NPP Cloud Product [Ackerman *et al.*, 1998, 2008; Frey *et al.*, 2008; King *et al.*, 2003; Platnick *et al.*, 2003]. Due to the fact that Suomi-NPP VIIRS is identical to JPSS-VIIRS, currently S-NPP VIIRS provides the optimum source of data for testing, the channels of Suomi-NPP VIIRS and those used in the JPSS VIIRS ADP algorithm is listed in Table 6.

S-NPP VIIRS Sensor Data Record (SDR) data, VIIRS cloud mask product and Terrain Corrected Geolocation (GMTCO) were obtained from NASA Atmosphere Product and Evaluation and Test Element (PEATE) hosted at Space Science and Engineering Center (SSEC) in University of Wisconsin (<http://peate.ssec.wisc.edu/>). The corresponding required inputs for JPSS ADP product, which are listed in Table 8, are derived from these data. The Visible channel reflectances and Brightness Temperatures for the IR channels were from SDR data. Viewing and illumination geometry and geolocation are from GMTCO. Various cloud tests used in ADP product are extracted from the corresponding bits in the VIIRS cloud mask product (VCM). Snow/ice mask from VCM is used as the primary source of snow/ice mask. Land/water mask is also from VCM. Both sun glint mask and day/night flag are internally calculated as described in section 3.12.

## 4.1.2 Truth data

### 4.1.2.1 Supervised S-NPP VIIRS RGB image and VIIRS Aerosol Optical Depth Product

Both smoke and dust have a distinctive signature in RGB image, and NASA Natural Hazard system (<http://earthobservatory.nasa.gov/NaturalHazards/>) and MODIS rapid response system (<http://rapidfire.sci.gsfc.nasa.gov/gallery/>) routinely issues MODIS observations containing the smoke and dust outbreaks around the globe. By selecting VIIRS granules which are dominated by either only smoke or only dust, a supervised truth dataset were obtained. Then the corresponding Aerosol Optical Depth (AOD) product is used to identify the smoke/dust laden ( $AOD > 0.2$ ) and smoke/dust free ( $0.2 > AOD > 0.0$ ) pixels; Note that, currently the IDPS NPP VIIRS AOD product over land only covers dark dense vegetation surface. VIIRS pixels with no AOD retrievals are considered as covered by clouds or snow/ice, bright surface over land and bad input data. These conditions are consistently unfavorable for detection of smoke/dust as well as discussed in Section 3. In addition, due to the difference in cloud screening procedures between VIIRS AOD product and JPSS ADP algorithm, only pixels with both VIIRS AOD product and JPSS ADP product indicating cloud-free conditions are used for quantitative analysis.

### 4.1.2.2 Aerosol Robotic Network (AERONET) observations

The ground-based remote sensing network, AEROSol Robotic Network (AERONET), equipped with well-calibrated sunphotometers over more than 100 sites throughout the world, measures and derives quality-assured aerosol optical properties for a wide diversity of aerosol regimes, for up to the last 10 years [Holben et al., 1998; 2001; Dubovik et al., 2002]. These high quality data have been widely used as ground “truth” for evaluation and validation of satellite remote sensing of aerosols [Yu et al., 2003; Remer et al., 2005]. As for primary source of *in situ* observations, observations from AERONET will be the primary source, since the stratification of Angstrom Exponent data from AERONET indicates the presence of smoke or dust particles in the atmosphere. However, the Angstrom Exponent used as a proxy for aerosol particle size parameter has a limited ability to separate different types of aerosols. At best it can provide a clean separation of dust and smoke but not haze and smoke (see Figure 24)

# Aerosol Particle Size Parameter

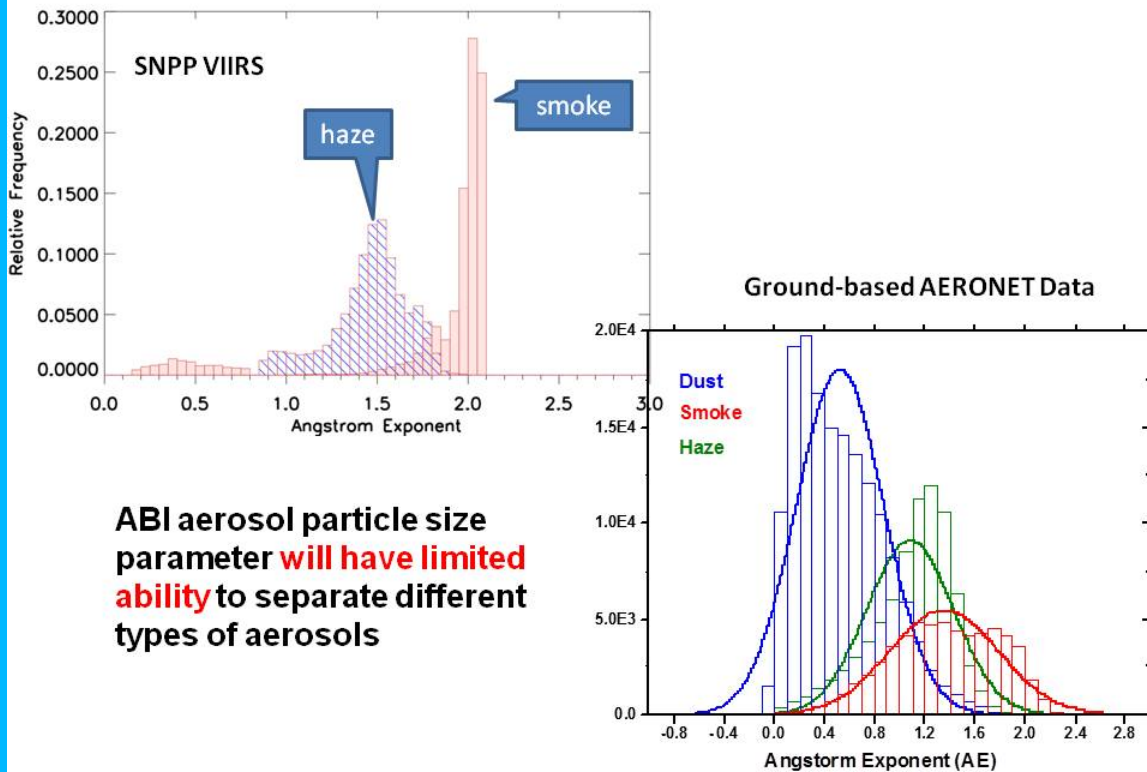


Figure 24 : Top: histogram of Angstrom Exponent (AE) for pixels with smoke and haze in S-NPP VIIRS observations. Bottom: histogram of Angstrom Exponent (AE) for smoke, dust and haze from AERONET observations.

The matchup strategies are as following:

- Collocated AERONET and JPSS VIIRS ADP smoke/dust detection results
  - Spatial coverage: a circle with a radius of 25 km and centered on AERONET stations are chosen to determine the dominant SM type from JPSS ADP product.
  - Temporal average: AERONET measurements within a 30minutes window centered on the NPP VIIRS overpass time, at least three measurements are available.
- Dominant SM type from JPSS ADP product
  - 80% of pixels in the circle are cloud, snow/ice and glint-free (for over water)
  - The type of more than half the valid retrievals was chosen as the dominant type from JPSS ADP product.
- Classification of Aerosol Type over AERONET:
  - Smoke:
    - AOD>0.3 and AE>1.1
  - Dust:
    - AOD>0.3 and AE<0.6



### 4.1.2.3 CALIPSO VFM product

With the launch of CALIPSO and CloudSat in the EOS A-Train formation in April 2006, the ability to conduct global satellite cloud product validation increased significantly. Besides cloud type, CALIPSO also identifies aerosol types including smoke and dust. Vertical Feature Mask (VFM) is the CALIPSO product which is used for validating VIIRS ADP product. It gives not only vertical distribution of aerosol layer but also 6 types of aerosol, including clean marine, dust, polluted dust, polluted continental, clean continental, polluted dust and smoke. However, the sparse spatial coverage and narrow swath of CALIPSO lidar observation limits the amount of match-up overpasses with VIIRS for smoke and dust cases.

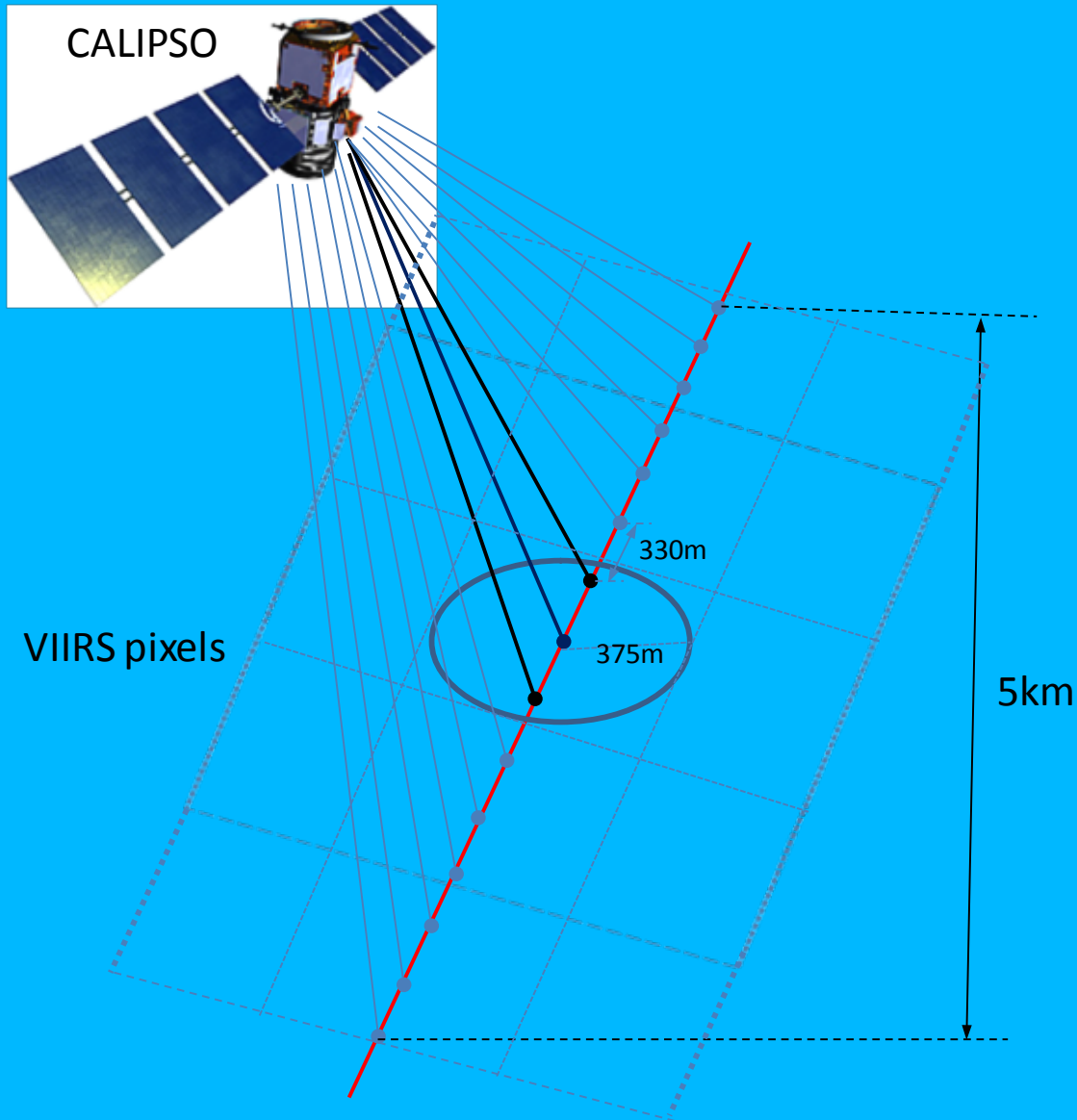


Figure 25: Schematic illustration of matchups between S-NPP VIIRS and CALIPSO-VFM product.

The matchup strategies are as following:

- Time difference:  $\pm 30$  minutes within the starting time of each CALIPSO VFM track.

- Spatially, VIIRS pixel that is within  $\pm 375\text{m}$  of the location of the middle profile (i.e., 8<sup>th</sup> profile) in each 5km trunk of CALIPSO VFM product is selected, then a box of 5 by 5 pixels, total of 25 pixels, centered over the selected pixel is matched.
- SM Types in CALIPSO VFM are grouped as :
  - a. dust (including polluted dust)
  - b. smoke
  - c. cloudy
  - d. clear
  - f. others
- SM Types in JPSS VIIRS ADP product are grouped in 5 by 5 box as :
  - a. dust
  - b. smoke
  - c. cloudy
  - d. Unknown/None/Clear
- Determination the dominant SM type in CALIPSO VFM

For each 5 km trunk of CALIPSO VFM, which consists of 15 profiles, the dominated aerosol type for each profile is first determined through the calculation of dust (, smoke and others) fraction (i.e., no of dust (, smoke and others) layer divided by the no. of aerosol layer from surface to 20.2 km. For profile without clouds at any layer, any aerosol type has the fraction larger than 80% is defined as the dominant type. If all of three is less than 80%, then the dominant type is defined as “others”. If clouds exist in any layer, this profile is defined as “cloudy”. Otherwise, this profile is defined as “clear”. The ensemble SM type for each 5km trunk is further determined as: dust if 12 out of 15 profiles are dust, as smoke if 12 out of 15 profiles are dust, as others if not smoke or dust, as cloudy if any one of 15 profiles is cloudy or as clear if all of 15 profiles are clear.

- Quality Control
  - Medium to high quality used

## 4.2 *Output from proxy data sets*

### 4.2.1. Output for Dust Detection

#### 4.2.1.1. Comparison with RGB image and AOT product

Supervised RGB image can capture dust events very well since dust plumes look bright and brown in the image compared to cloud. Thus, RGB image can be used to validate the ADP product dust detection algorithm qualitatively. Therefore, we can apply dust detection algorithm to S-NPP VIIRS measurement of a dust event and compare the detection result with the VIIRS RGB image. One example is shown in Figure 26 for the NPP VIIRS observations on April 5, 2015 at around 09:59 UTC. Qualitative comparison of dust detection with VIIRS RGB image shows a good agreement.

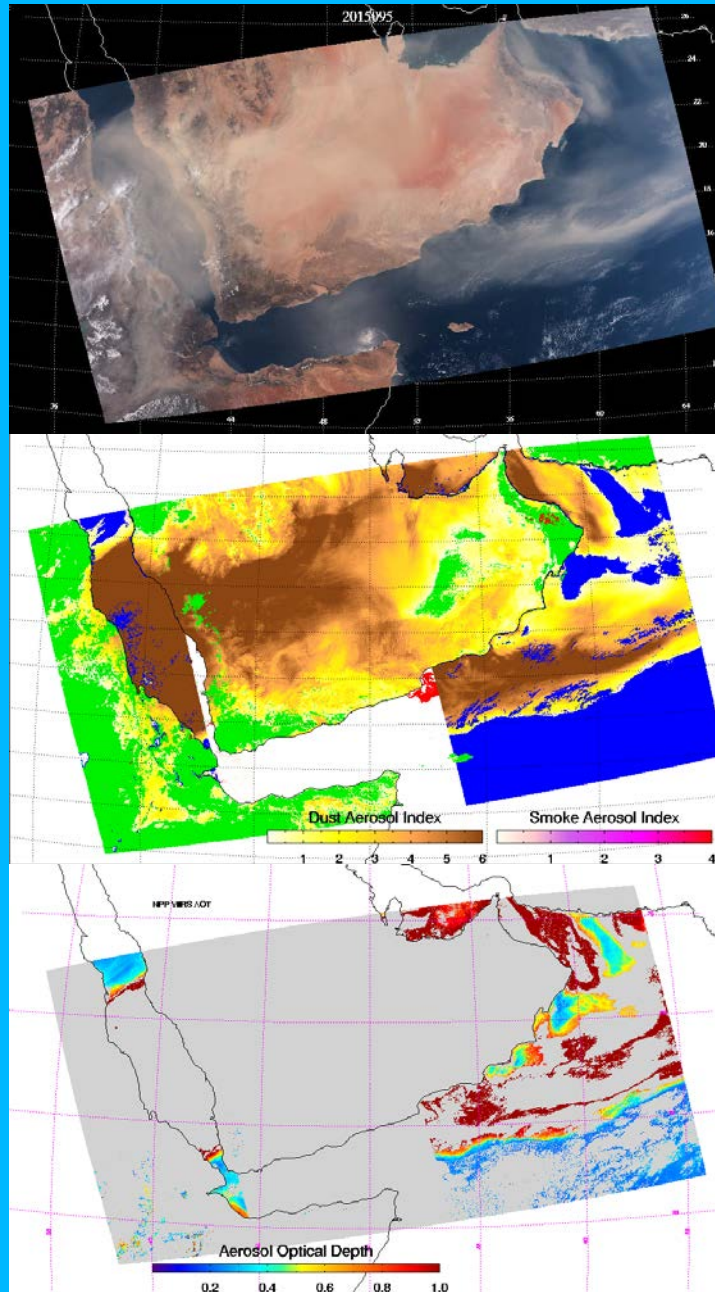


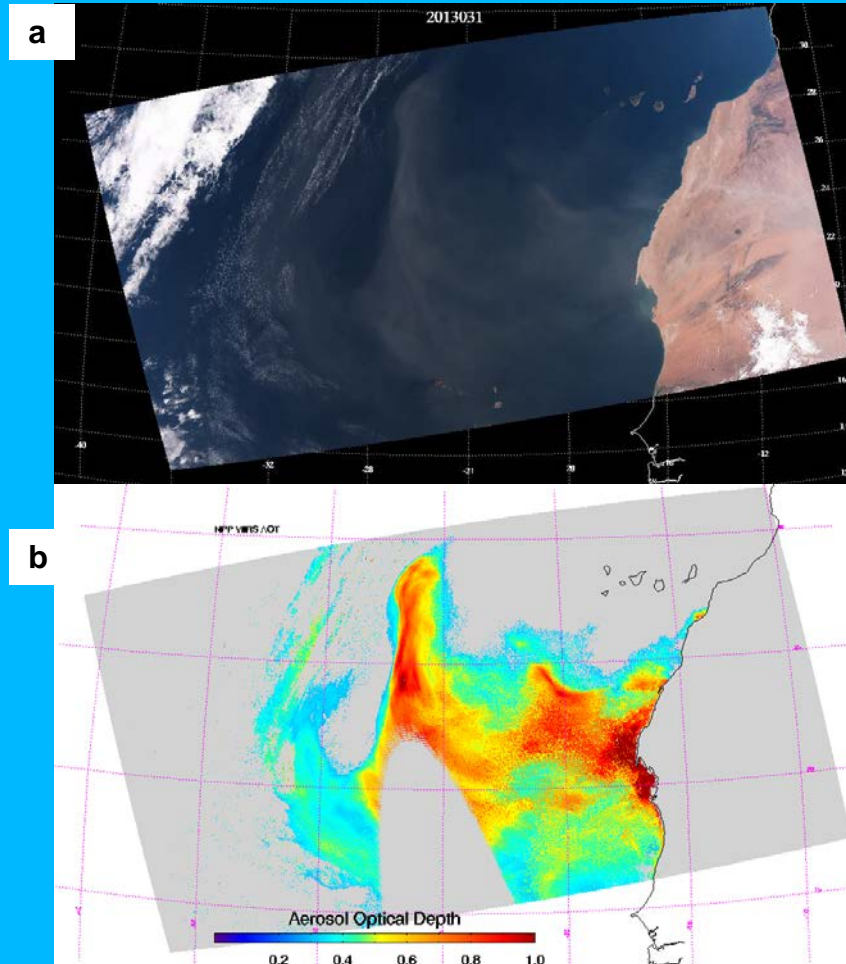
**Figure 26: TOP: S-NPP VIIRS RGB Image on April 5, 2015 at about 09:59 UTC. Middle: the results of the dust detection from JPSS ADP product. Bottom: S-NPP VIIRS AOD (only pixels with AOD > 0.2 are shown)**

Dust particles are mainly located near desert regions and downwind areas and a dust event is mainly associated with high aerosol optical depth (AOD) so that the AOD distribution retrieved from satellite observation can help us to qualitatively examine the ADP product dust detection algorithm.

#### **4.2.1.2. Comparison with CALIPSO VFM**

CALIPSO is onboard the same spacecraft as MODIS Aqua, which is afternoon satellites as S-NPP VIIRS and its VFM products provide vertical distribution of 6 aerosol types, including smoke and dust

over its narrow (a footprint with a 70m diameter) track. Although the sparse spatial coverage of CALIPSO lidar observations limits the number of overpass matchups with S-NPP VIIRS granule, Over a whole global during the time period of 2.5 yrs (from 2012 to June of 2015), many cases containing dust outbreak were found. And the possibility of using the S-NPP VIIRS and CALIPSO overpass and the CALIPSO aerosol type data to validate the dust detection in JPSS ADP product is explored.



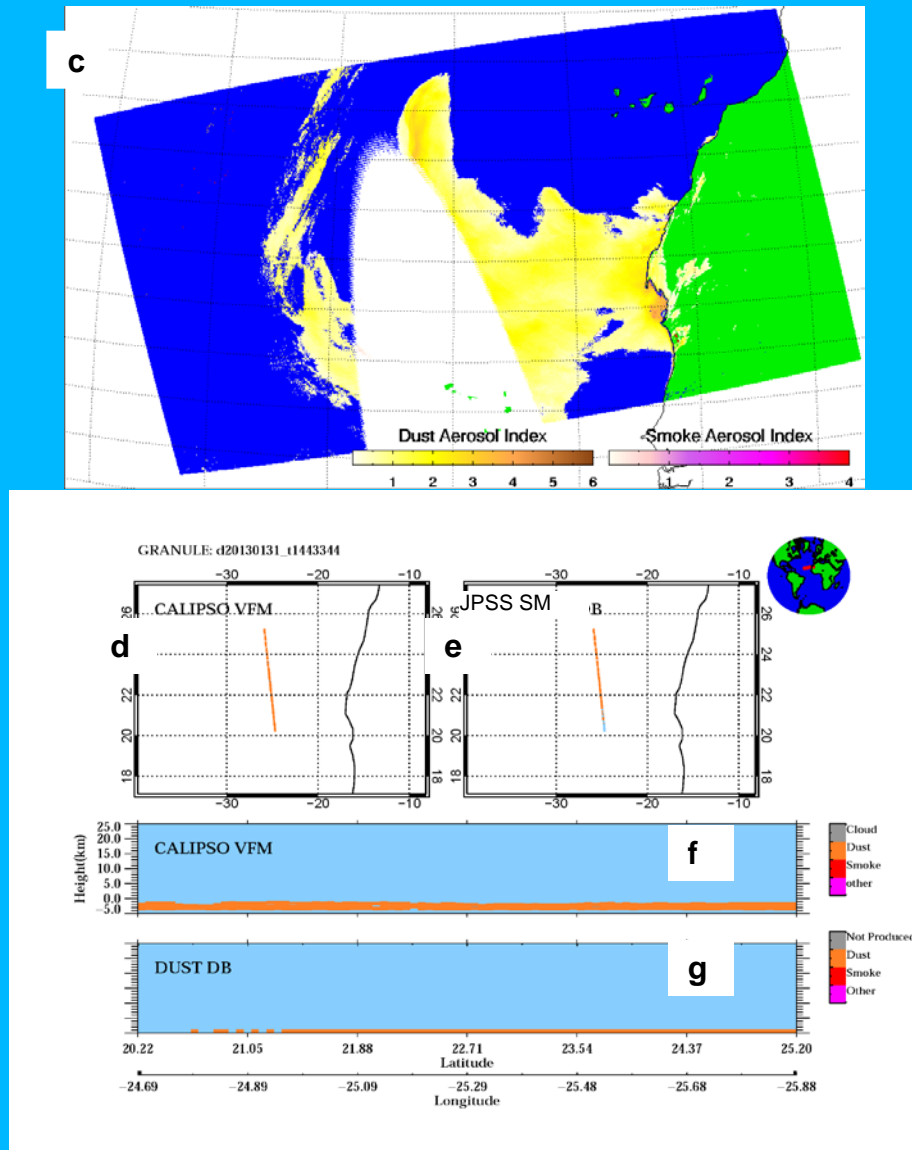


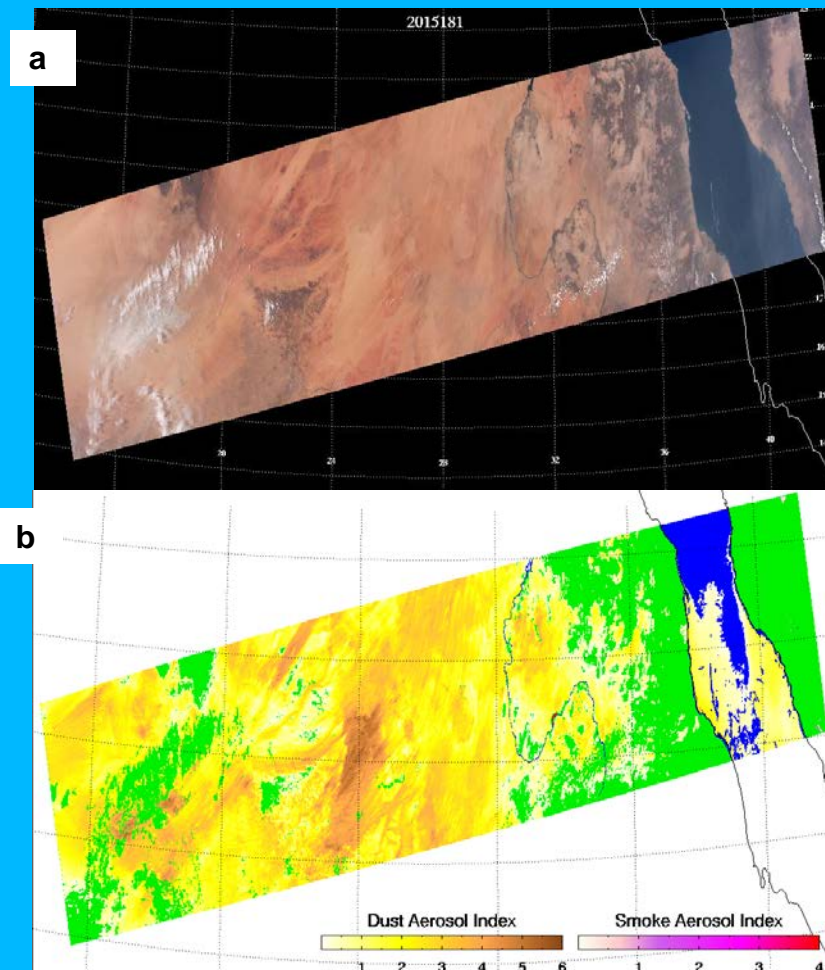
**Figure 27: Comparison of dust detected (orange) using VIIRS ADP product algorithm with CALIPSO Vertical Feature Mask (VFM) on January 30, 2013, UTC 14:33. a) RGB image, b) Aerosol Optical depth from S-NPP VIIRS aerosol Product, c) Dust mask from ADP product, d) Dust (orange) on CALIPSO track, e) Dust (orange) detected with VIIRS ADP product algorithm on CALIPSO track, f) Dust vertical distribution on the part of CALIPSO track collocated with VIIRS ADP product, g) Dust from VIIRS ADP product on the same part of track as in b.**

First example is shown in Figure 27 for CALIPSO VFM vs. VIIRS ADP product for S-NPP VIIRS observations on January 30, 2013 at around 14:33 UTC. The dust plume is clearly visible in the RGB image (Figure 27 a). As shown in Figure 27(d), CALIPSO VFM indicates existence of dust over the middle part of CALIPSO track which has collocations with S-NPP VIIRS, and the dust is seen over the coast of West Africa and close to sunglint region. VIIRS ADP product dust mask over the co-located CALIPSO track is given in Figure 27 c.

CALIPSO VFM data shows that dust was dispersed between the surface and 2 km (Figure 27 g). First of all, it is clearly seen that there is a good agreement between the dust plume pattern detected by ADP product and the pattern shown in both RGB and VIIRS AOD ( $>0.2$ ). Secondly, similar good agreement

is also seen on CALIPSO VFM track. It is noted that this co-located overpass is right on the edge of a sun glint region where VIIRS ADP product data are not processed. Therefore, by excluding pixels in the overpass within sun glint and with VIIRS AOD less than 0.2, the agreement between VIIRS ADP product and CALIPSO VFM for this event is 83% and 85%, respectively for Accuracy and PTPD. The definition of accuracy (and PTPD) is given shown in equation in 4.31

Unlike the case in Figure 27, the co-located overpass shown in Figure 28 between CALIPSO and S-BPP VIIRS is over land, the agreement between VIIRS ADP product and CALIPSO VFM is about 86 % and 88%, respectively for Accuracy and PTPD.



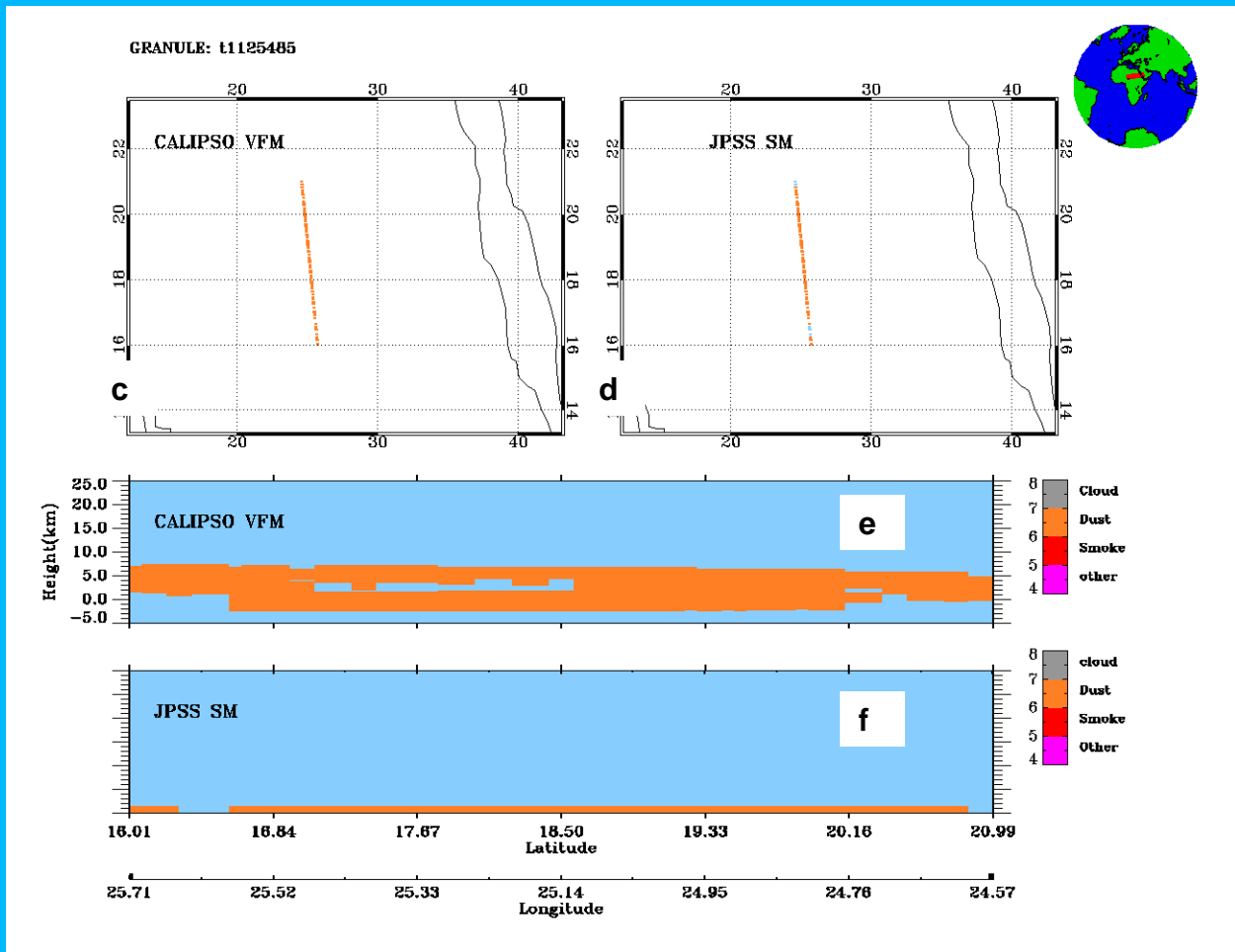


**Figure 28:** Comparison of dust detected (orange) using JPSS ADP product algorithm with dust (orange) in CALIPSO Vertical Feature Mask (VFM) on June 30, 2015 at UTC 11:25. a) S-NPP VIIRS RGB image, b) Smoke/dust mask from JPSS ADP product, c) Dust (orange) on CALIPSO track, d) Dust (orange) detected with JPSS ADP product algorithm on CALIPSO track, e) Dust vertical distribution on the part of CALIPSO track collocated with JPSS ADP product, f) Dust from VIIRS ADP product on the same part of track as in b.

## 4.2.2. Output for Smoke Detection

### 4.2.2.1. Comparison with RGB image

Smoke is associated with fire events and the spatial distribution of smoke plume is uniform and looks gray to a human eye compared to a cloud. This feature is useful in identifying smoke plumes in a RGB image without difficulty. Thus, RGB image can be used to validate the ADP product smoke detection. One example is shown in Figure 29 for forest fire events over U.S. and Canada observed by S-NPP VIIRS on June 29, 2015. Qualitative comparison of smoke detection with S-NPP VIIRS RGB image shows a good agreement, especially for the thick smoke plumes over vegetated areas.

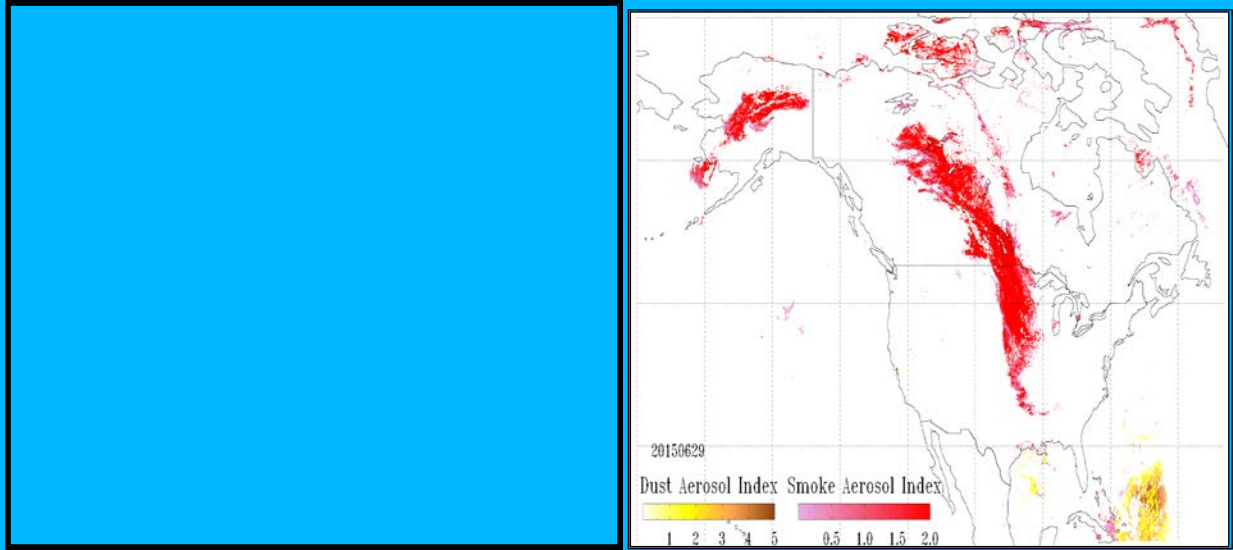


**Figure 29: Left: S-NPP VIIRS RGB Image on June 29, 2015 over North America. Right: the results of the smoke detection (pixels flagged as smoky are in colored red) from JPSS ADP product.**

In general, the two smoke plumes, one from Canada down to the Middle West in U.S. and another one over Alaska, identified by JPSS ADP products. i.e., pinkish to red color shown in the left image of Figure 29, are very consistent with the dark-gray area in RGB image (right image in Figure 29) where the elevated smoke plumes are shown. It is also noted that patches of dust plumes, transported by crossing Atlantic Ocean from West Africa, are also identified in JPSS ADP product, i.e., yellow-brown color shown in the left image of Figure 29. Some false smoke were identified over the snow/ice edges, however, it is expected such false alarm will be eliminated after a better snow/ice mask is adopted.

#### 4.2.2.2. Comparison with CALIPSO VFM

In Figure 30 and Figure 31, two cases of VIIRS smoke detection is shown for two different days in different years. For both examples shown, VIIRS smoke detection mask agrees well with MODIS RGB image and the matchups with CALIPSO track show that the agreement between what CALIPSO observed and what VIIRS is showing is good. Parts of the track where CALIPSO detects smoke, VIIRS identifies those pixels as clear-sky/clouds or the other way. It should be noted that we have not yet tested the sensitivity of our retrieval to the height of the aerosol layer and aerosol amount. Although, we can use CALIPSO to identify the height of the aerosol, we have not taken the validation efforts to the next level where we will be conducting “deep-dive” studies of individual case studies to understand the limitations of the algorithms.



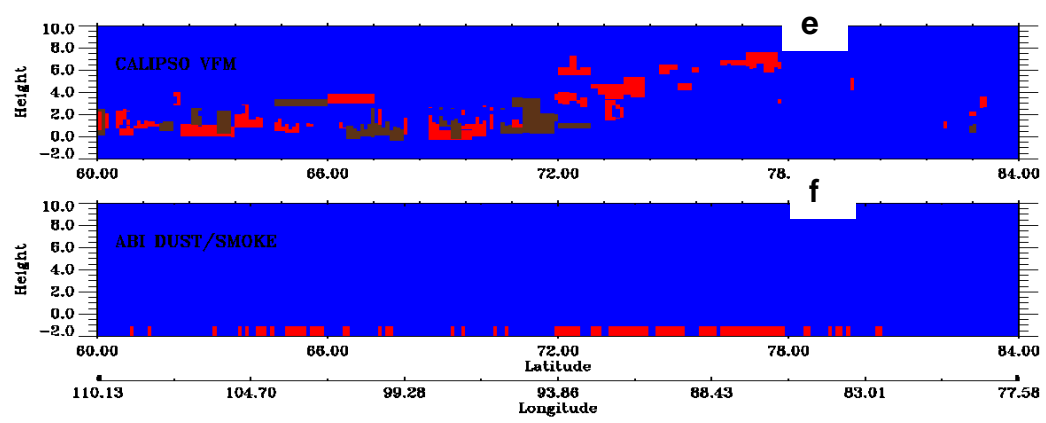
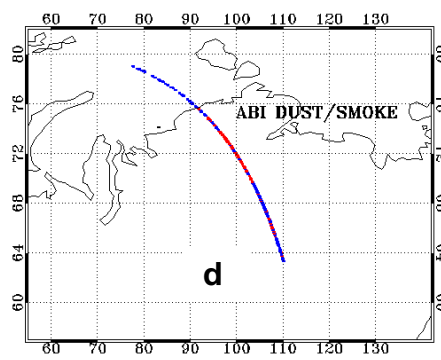
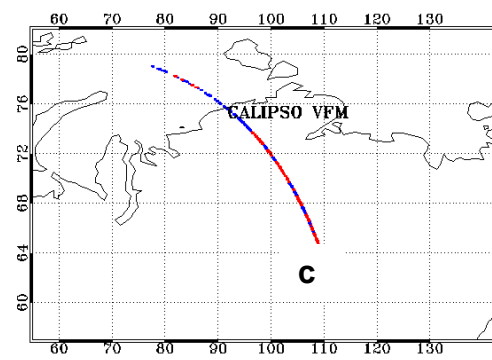
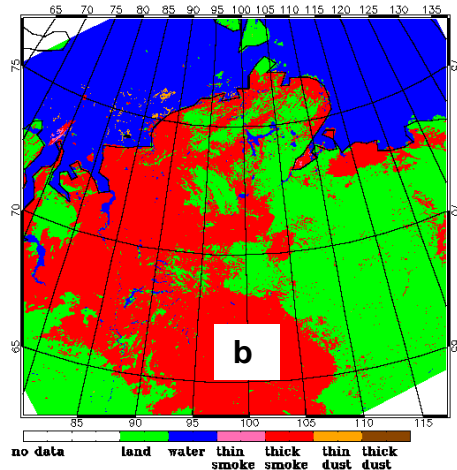
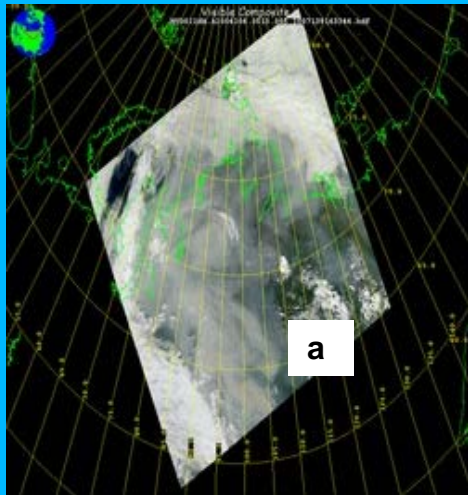


**Figure 30: Comparison of smoke detected (red)) using VIIRS ADP product algorithm with smoke in CALIPSO Vertical Feature Mask (VFM) on July 25, 2006, UTC 05:15. a. RGB image b. Aerosol Optical depth from MODIS C5 aerosol Product. C. Smoke (red) on CALIPSO track. d. Smoke detected with VIIRS ADP product algorithm on CALIPSO track. e. Smoke vertical distribution on the part of CALIPSO track collocated with VIIRS ADP product d. smoke from VIIRS ADP product on the same part of track as in b.**

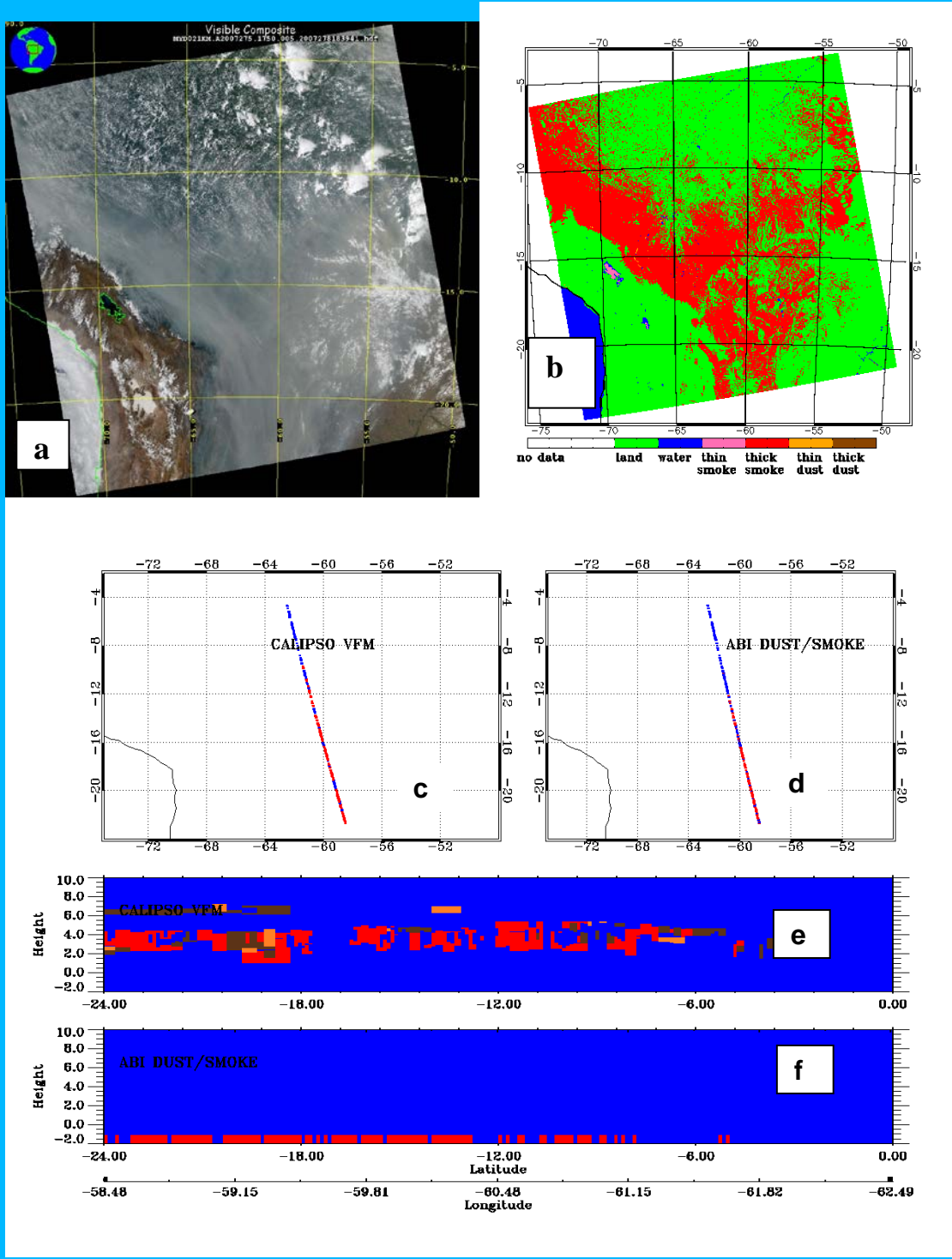


Figure 31: Comparison of smoke detected (red) using VIIRS ADP product algorithm with smoke in CALIPSO Vertical Feature Mask (VFM) on October 2, 2007 at 17:50 UTC. a) RGB image, b) Aerosol Optical depth from MODIS C5 aerosol Product, c) Smoke (red) on CALIPSO track, d) Smoke detected with VIIRS ADP product algorithm on CALIPSO track, e) Smoke vertical distribution on the part of CALIPSO track collocated with VIIRS ADP product, d) smoke from VIIRS ADP product on the same part of track as in b.

For smoke detection, two CALIPSO VFM vs. VIIRS ADP product cases are presented. They are both over land on July 23, 2006 at 05:15 UTC and October 2, 2007 at 17:50 UTC (Figure 30 and Figure 31). The agreement between the VIIRS ADP product and CALIPSO VFM is 75% and 80% respectively. For a total of 22 smoke cases, the agreement between VIIRS ADP product and CALIPSO VFM is about 80%.

### 4.1.3. Product Performance Evaluations

Due to lack of true ground truth for the accuracy estimate, the evaluation of ADP product products is mainly based on the inter-comparison to other satellite based smoke and dust products (such as RGB image, HMS smoke analysis, and CALIPSO VFM product) and aerosol types derived from AERONET measurements. The statistics matrix for evaluating ADP product is consisted of three parameters. Among them, accuracy, this is defined as the Probability of Correct Detection (PCD), is semi-quantitative and given as:

$$PCD = \frac{TPD + TND}{TPD + FPD + TND + FND} \times 100 \quad (4.3.1)$$

In equation 4.3.1, TPD is true positive detection, TND is true negative detection, FPD is false positive detection, and FND is false negative detection. The primary validation approach will provide an overall performance of the algorithm but will not provide information on performance of the algorithm over different geographic regions. Therefore, additional spot checks and statistics will be carried out.

Because the accuracy of aerosol detection calculated using equation 4.3.1 will include true negative detects (clear sky pixels), it will not provide information on the true positive detects which a user might be interested in. Therefore, other two parameters, i.e., Probability of True Positive Detection (PTPD) and Probability of False Positive Detection (PFPD) are computed using equations 4.3.2 and 4.3.3:

$$PTPD = \frac{(TPD)}{(TPD+FND)} \times 100 \quad (4.3.2)$$

$$PFPD = \frac{(FPD)}{(FPD+TPD)} \times 100 \quad (4.3.3)$$

As discussed in section 4.2, two types of truth data are used for quantitative evaluations of JPSS ADP product performance. One is the AERONET observations and the other one is CALIPSO VFM product. By collocating outputs from JPSS VIIRS ADP product algorithm run with S-NPP VIIRS measured radiance as proxy with these two types of truth data, statistics on accuracy, PTPD, and PFPD are calculated. The time period covers from January 1, 2013 to August 30, 2015. Details on the statics are given in the following two sections.

#### 4.2.1.1 Against AERONET observations

**Table 13 Accuracy, Probability of True Positive Detection, and Probability of False Positive Detection of JPSS ADP product for Dust detection over AERONET Stations**

<b>Stations</b>	<b>Year</b>	<b>True positive</b>	<b>False positive</b>	<b>True negative</b>	<b>False negative</b>	<b>Accuracy (%)</b>	<b>PTPD (%)</b>	<b>PFPD (%)</b>
<b>Darkar</b>	2013	63	1	106	10	93.9	86.3	0.2
	2014	74	3	45	10	90.1	88.1	0.4
<b>Solar_Village</b>	2013	81	26	59	30	71.4	73.0	24.3
	2014	11	4	65	5	89.4	68.8	26.7
<b>Capo_Verde</b>	2013	44	0	56	3	97.1	93.6	0.0
	2014	53	1	17	1	97.2	98.1	0.2

**Table 14 Accuracy, Probability of True Positive Detection, and Probability of False Positive Detection of JPSS ADP product for smoke detection over AERONET Stations**

<b>Stations (Biomass –burning)</b>	<b>True positive</b>	<b>False positive</b>	<b>True negative</b>	<b>False negative</b>	<b>Accuracy (%)</b>	<b>PTPD (%)</b>	<b>POFD (%)</b>
<b>Alta_Floresta</b>	10	0	178	0	100.0	100.0	0.0
<b>Bonanza_Creek</b>	1	0	48	0	100.0	100.0	0.0
<b>Jabiru</b>	1	0	313	0	100.0	100.0	0.0
<b>Moscow_MSU_MO</b>	16	2	92	1	97.2	94.1	11.0
<b>Tomsk_22</b>	17	1	83	0	99.0	100.0	5.0
<b>Yakutsk</b>	22	1	88	1	98.2	95.6	4.3

Table 13 and Table 14 is the results of comparisons of JPSS ADP product with AERONET Observations, respectively for smoke and dust over stations which is prevailing with the corresponding aerosol type. It is clearly see that, for dust prevailing stations (as shown in Table 13), the accuracy varies from 70 to 97%, PTPD is in the range from 73 to 98%, and PFPD can reach up to 27%. For smoke prevailing stations (as shown in Table 14), the number of true positive event is a lot smaller the accuracy, compared with dust, PTPD and PFPD is respectively about 97~100%, 94~100% and 0~11%.

To evaluate the overall performance of JPSS ADP product performance, ensemble values for accuracy, PTPD and PFPD are calculated with matchups between ADP products with observations over all the available AERONET stations during this 2 and half yrs time period (about 400 stations). The results are given in Table 15. It is seen that the ensemble value of Accuracy (i.e., Probably of Correct Detection), POPD and PFPD is 99%, 70% and 21% for dust and 97%, 92% and 11% for smoke.

Therefore, based on these validation results, the JPSS VIIRS ADP product meets the mission requirement as shown in Table 1.

**Table 15 Ensemble Accuracy, Probability of True Positive Detection, and Probability of False Positive Detection of JPSS ADP product for smoke and dust detection**

Type	True positive	False positive	True negative	False negative	Accuracy	PTPD	PFPD
Dust	2028	549	149897	882	99.0	69.7	21.3
smoke	9324	1214	60397	799	97.2	92.1	11.5

#### 4.2.1.2 Against CALIPSO VFM product

Performance evaluations of JPSS ADP product are also carried out by comparing with CALIPSO VFM product. The global coverage of CALIPSO VFM renders us to stratify the evaluation according to the land type, i.e., over land and over water. The results for over land and over water are given respectively in Table 16 and Table 17.

It is seen that, for dust detection, the Accuracy and PTPD are 84 and 80% over land, while they can reach up 96 and 95% respectively, indicating more accurate dust detection can be obtained over water then over land. This is consistent with the results shown in Section 3.4.1., i.e., the surface reflectance over water is much smaller and uniform over water than that over land. As for smoke detection, the accuracy and PTPD are very similar between over land and over water. They are about 99% and 95% over land and 94% and 97% over water. In addition, it is clear that PFPD for smoke detection is much larger than that for dust detection. PFPD for smoke detection can reach up to 45%, while it is less than 5% for smoke detection.

In general, comparisons with CALIPSO VFM products indicate that JPSS ADP product meets the mission requirement as shown in Table 1.

**Table 16. Accuracy, Probability of True Positive Detection, and Probability of False Positive Detection of JPSS ADP product for smoke and dust detection over land**

Type	True positive	False positive	True negative	False Negative	Accuracy (%)	PTPD (%)	PFPD (%)
DUST	10669	170	5676	2840	84.4	80.0	1.6
SMOKE	307	159	19534	14	99.1	96.7	34.1

**Table 17. Accuracy, Probability of True Positive Detection, and Probability of False Positive Detection of JPSS ADP product for smoke and detection over water**

Type	True positive	False positive	True negative	False negative	Accuracy (%)	PTPD (%)	PFPD (%)
DUST	297	11	139	10	95.4	96.4	3.3
SMOKE	601	507	7605	15	94.0	97.5	45.7

### 4.3 Framework run and validation

#### 4.1.1. Framework run

As shown in section 4.1, the ADP product algorithm was validated extensively. However, this validation work was done with offline runs, i.e., running ADP product algorithm without integrating it into JPSS Reduction VIIRS product framework. Under the operational environment, ADP product algorithm will be running in the framework. In general, the procedure for running the ADP product algorithm in the framework is as follows: first, common input radiance data are generated from proxy data set, the common dataset includes both the required input and ancillary data in a common data format, i.e., netCDF. Second, the aerosol detection algorithm is called according to the order of precedence. Finally, results from each product are written to an output file in netCDF format.

#### 4.1.2. Consistency tests with S-NPP VIIRS granules

To test the offline runs with runs through integration of ADP product algorithm into the framework, comparisons were made between outputs from offline run with outputs from framework run with common input data and using the ADP algorithm. For tests shown below, S-NPP VIIRS observations from several granules were used as proxy for JPSS VIIRS, i.e., 750 m radiances from S-NPP VIIRS bands corresponding to JPSS VIIRS channels required by ADP product algorithm and cloud mask from S-NPP VIIRS cloud mask product. Figure 32 and Figure 33 show the comparisons of offline smoke/dust mask with those from framework run for two cases, one for smoke event and one for dust outbreak. It is seen that Framework runs were able to reproduce the same results as those from offline run for both cases, with an agreement of about 99.5%.

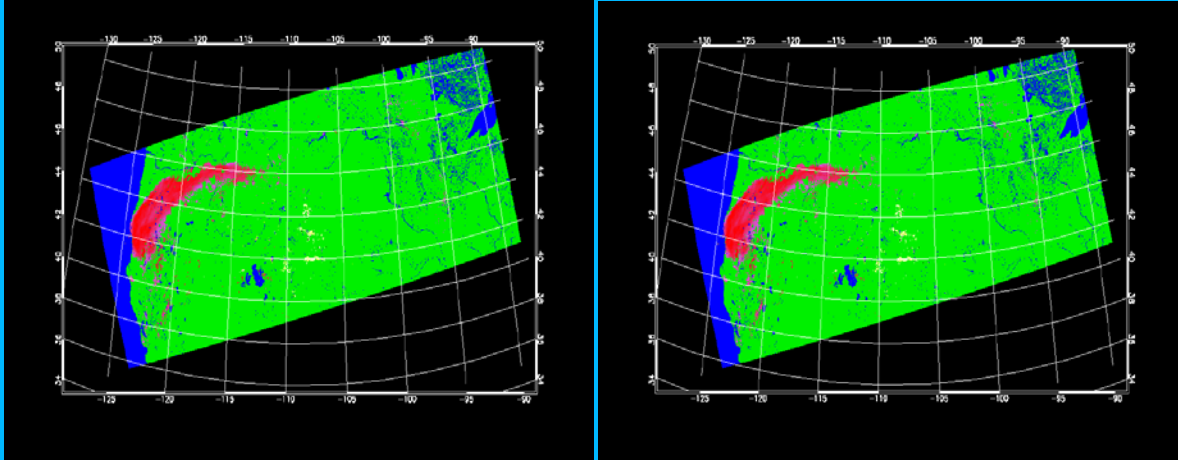


**Figure 32: Comparison of offline run with framework run for S-NPP VIIRS observation on August 3, 2014, UTC13:20. a) smoke/dust mask from framework run, b) smoke/dust mask from offline run.**

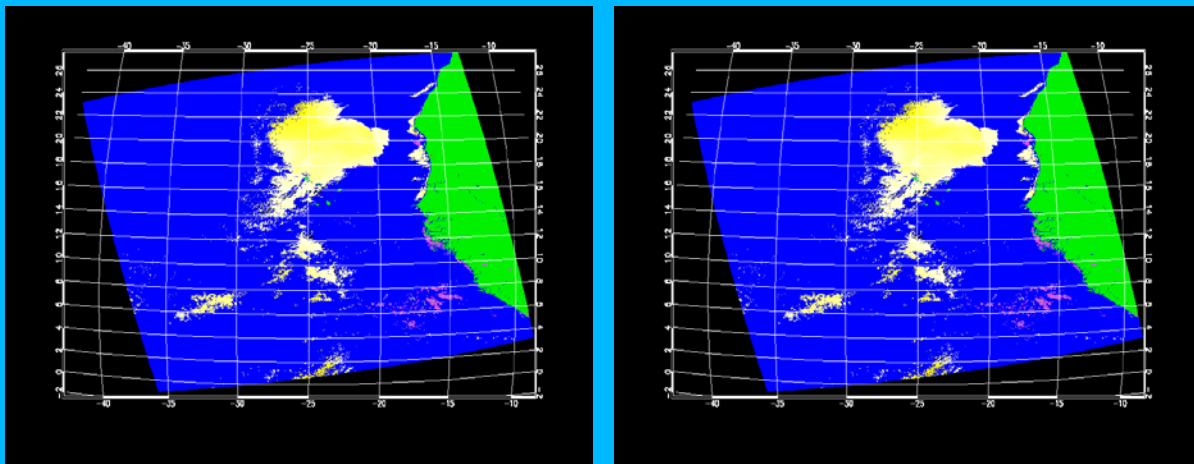


**Figure 33: Comparison of offline run with framework run for S-NPP VIIRS observation on February 13, 2014, UTC 03:25. a) smoke/dust mask from framework run, b) smoke/dust mask from offline run.**

### 4.1.3. Results from Framework run with global S-NPP VIIRS observation

To further test the framework run, global S-NPP VIIRS observations for July 15, 2014 and July 16, 2014 were selected as proxy input to run ADP product algorithm in the framework. Figure 34a and b show global smoke/dust mask product from framework run of the ADP product algorithm for these two consecutive days. For the purpose of comparison, OMPS Absorbing Aerosol Indexes for the corresponding two consecutive days are also showed in Figure 34b and c. In general, the framework run produced no abnormal smoke or dust pattern for each of these two days, and consistency is seen between results from these two consecutive days. Furthermore, large smoke plumes resulting from biomass burning were identified over North America and Russia, and dusts from dust storm are shown over Sahara desert. Although the location of the dust and smoke plumes are consistent between the two days, there are differences in the amount of smoke and dust present. This is very typical because while old fires die out, new fires form and dust transport occurs in the free troposphere moving it long distance over short time periods. In addition, smoke/dust mask produced by ADP product from framework run has very similar pattern as OMPS Absorbing Aerosol Index (shown in Figure 34b and c), which is an

indication of the presence of smoke/dust by using UV observations, even though it cannot differentiate between smoke and dust.

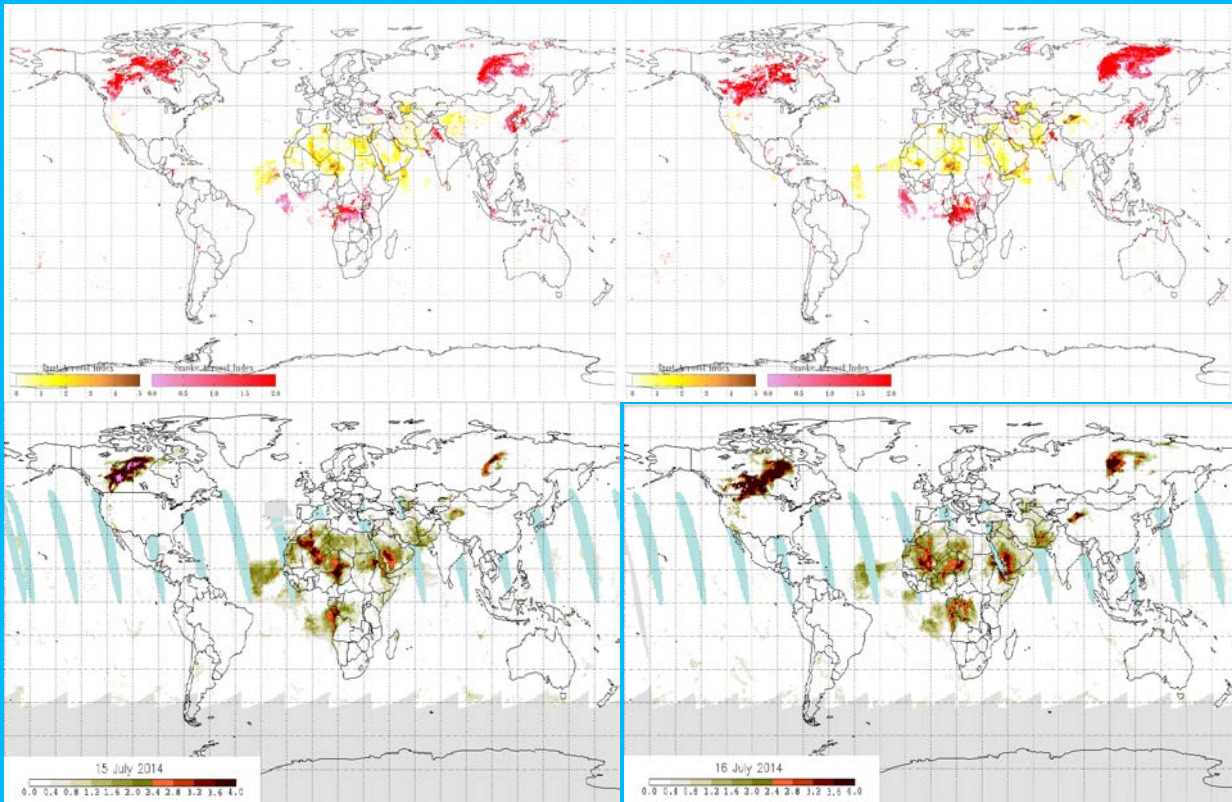


**Figure 34: Global smoke/dust mask from ADP product algorithm run in the framework for S-NPP VIIRS observations. a) July 15, 2014, b) July 16, 2014. Absorbing Aerosol Indexes from OMPS for these two days are also shown in c) and d).**

## 5. PRACTICAL CONSIDERATIONS

### 5.1 Numerical Computation Considerations

The ADP product algorithm is implemented sequentially. Because some tests require ancillary data, the ancillary data (e.g., day/night, snow/ice, sun glint, and cloud/clear) need to be input first. To balance the efficiency and memory requirement for the full disk processing, a block of scanning pixels are read into a RAM buffer together instead of reading data pixel by pixel.

### 5.2 Programming and Procedural Considerations

The ADP product requires knowledge of spatial uniformity metrics that are computed for each pixel using pixels that surround it. Detection is performed separately for land and water. In addition, future temporal tests require information from the previous image. Beyond this reliance, the ADP product is a pixel by pixel algorithm.



### **5.3 Quality Assessment and Diagnostics**

The following procedures are recommended for diagnosing the performance of the ADP product.

- Monitor the percentage of pixels falling into each ADP product aerosol bin values. These values should be quasi-constant over a large area.
- Monitor frequency of false positives of regions to assess need to have region specific thresholds developed and implemented.
- Periodically image the individual test results to look for artifacts or non-physical behaviors.
- Monitor retrievals over different surface (geographic) type for dependency of errors on surface brightness
- Monitor spectral threshold values and provide a quality flag depending on how close the tests used in the ADP algorithm are to specified thresholds
- Monitor retrievals for temporal consistency. Are retrievals consistent from image to image?

Quality flag with value of 0/1/2 representing lower/medium/high confidence is generated according to how far the actual value for each test is from the predefined threshold.

### **5.4 Exception Handling**

The quality control flags for VIIRS ADP product will be checked and inherited from the flagged Level 1b sensor input data, including bad sensor input data, missing sensor input data and validity of each channel used; and will also be checked and inherited from the VIIRS cloud mask at each pixel.

The ADP product also expects the Level 1b processing to flag any pixels with missing geolocation or viewing geometry information.

The ADP product does check for conditions where the ADP product cannot be performed and generates quality control flags for snow/ice pixel, pixels with saturated channels; pixels missed geolocation or viewing geometry information.

### **5.5 Algorithm Validations**

For pre-launch validation, ADP product algorithm will be extensively validated by using S-NPP VIIRS RGB images, S-NPP VIIRS aerosol product, AERONET observations, Vertical Feature Mask from CALIPSO. For post-launch validation, besides above-mentioned approach, field campaigns will also be carried out. Details on Algorithm Validation are given separately in the VIIRS ADP product algorithm testing and validation plan document.

## **6. ASSUMPTIONS AND LIMITATIONS**

The following assumptions have been made in the current algorithm:

- Calibrated and geo-located radiances in VIIRS channels as required by VIIRS ADP product algorithm as shown in Table 2 are available;
- VIIRS cloud mask is available and adequate for the purpose of ADP algorithm
- All the ancillary data are available.

Limitations applying to current algorithm are:

- Only for daytime
- Smoke detection over land is limited to dark surface

- Not optimal for optically thin smoke and dust
- No testing has been done to determine algorithm limitations if smoke and dust or other types of aerosols co-exist in the same pixel

## **6.1 Performance**

The following assumptions are made in estimating the performance of ADP product algorithm:

- smoke/dust mask from CALIPSO VFM represents the truth;
- visual separation of smoke, dust and clear pixels from S-NPP VIIRS RGB image introduces negligible error;
- Thresholds used in the current algorithm are tailored for S-NPP VIIRS channel specifications. Post –launch tuning of these thresholds will not affect the estimate of algorithm performance.
- In case of VIIRS sensor degradation, product production might squeeze but studies will be carried out prior to the launch on the extent of the effect any changes to instrument characteristics will have on product quality.

## **6.2 Assumed Sensor Performance**

VIIRS ADP product algorithm assumes the sensor will meet its current specifications and produce calibrated quality radiance in the required channels (see Table 2). As shown in section 3.4.1., impacts from instrument noise and calibration error can be mitigated by adjusting threshold accordingly. However, ADP product algorithm has low tolerance on missing channels. As discussed in above sections, ADP product algorithm selects the optimal channels or combination of channels to best separate signal of smoke/dust from others. Therefore, missing any channel will definitely downgrade the performance of the algorithm and eventually leads to failure if crucial channels are missing.

In addition, ADP product algorithm will be dependent on the following instrumental characteristics.

- The spatial uniformity tests in ADP product will be critically dependent on the amount of striping in the data.
- Errors in navigation from image to image will affect the performance of the temporal tests.

## **6.3 Pre-Planned Product Improvement**

### **6.1.1. Improvement 1**

The spectral screening thresholds are currently not a function of viewing and solar geometry. Testing will be carried out to understand the dependencies of some of the smoke/dust tests on viewing and solar geometries. Additional testing will also be done using simulated proxy data to determine VIIRS spectral thresholds and how robust these spectral thresholds are under different scenarios. Based on these tests, algorithm could be improved.

### **6.1.2. Improvement 2**

Validation of smoke/dust detection still remains a challenge at this stage. Besides the validation exercises that have already been completed, additional validations will be carried out. They include comparisons with the ground-based measurements and other satellite products. Validation with ground-based measurement will take advantage of measurements from aerosol sampler in IMPROVE network and Angstrom exponent information from AERONET for any indications of smoke/dust particle over

some local and regional event. This, however, is not a direct comparison but an indirect subjective evaluation of smoke/dust detection product. For comparisons with other satellite products, Aerosol Index from OMI will be fully used to quantify the accuracy of smoke/dust products.

## 7. REFERENCES

- Ackerman, S. A., Using the radiative temperature difference at 3.7 and 11mm to track dust outbreaks, *Remote Sensing of Environment*, **27**: (2) 129-133, 1989.
- Ackerman, S. A., and K. I. Strabala, Satellite remote sensing of H<sub>2</sub>SO<sub>4</sub> aerosol using the 8-12μm window region: Application to Mount Pinatubo. *J. Geophys. Res.*, **99**, 18,639-18,649, 1994.
- Ackerman, S. A., Remote sensing aerosols using satellite infrared observations. *J. Geophys., Res.*, **102**, 17069–17079, 1997.
- Ackerman, Steven A.; Strabala, Kathleen I.; Menzel, W. Paul; Frey, Richard A.; Moeller, Christopher C. and Gumley, Liam E., Discriminating clear sky from clouds with MODIS, *J. Geophys. Res.*, **103**, 32,141-32,157, 1998.
- Ackerman, S. A., R. E. Holz, R. Frey, E. W. Eloranta, B. Maddux, and M. McGill, Cloud Detection with MODIS: Part II Validation. Accepted with revision to *J. Tech.*, 2008.
- Al-Saadi, J., et al., Improving national air quality forecasts with weather satellite aerosol observations, *Bull. Am. Meteorol. Soc.*, **86**, 1249– 1261, 2005
- Ashpole, I., and R. Washington (2012), An automated dust detection using SEVIRI: A multiyear climatology of summertime dustiness in the central and western Sahara, *J. Geophys. Res.*, **117**, D08202, doi:10.1029/2011JD016845.
- Barton, I. J., A. J. Prata, I. G. Watterson and S. A. Young, Identification of the Mount Hudson volcanic cloud over SE Australia. *Geophys. Res. Lett.*, **19**(12), June 19, 1992, 1211-1214, 1992.
- Bohren, C. F. and D. R. Huffman, “Absorption and scattering of light by small particles”, Wiley, New York, 1983.
- Burton, S. P.; Ferrare, R. A.; Vaughan, M. A.; Omar, A. H.; Rogers, R. R.; Hostetler, C. A.; Hair, J. W. (2013) , Aerosol classification from airborne HSRL and comparisons with the CALIPSO vertical feature mask, *Atmospheric Measurement Techniques Discussions*; Vol. 6 Issue 1, p1815.
- Bullard, J. E., Baddock, M. C., McTainsh, G. H., & Leys, J. F. (2008). Sub-basin scale dust source geomorphology detected using MODIS. *Geophysical Research Letters*, **35** (15), L15404. doi:10.1029/2008GL033928.
- Cho, H.-M., S. L. Nasiri, P. Yang, I. Laszlo, X. Zhao (2013), Detection of optically thin mineral dust aerosol layers over the ocean using MODIS. *J. Atmos. Ocean Tech.*, **30**, p. 896-916.
- Ciren, Pubu and Kondragunta, Shobha, Dust aerosol index (DAI) algorithm for MODIS, *Journal of Geophysical Research-Atmospheres* Volume: 119 Issue: 8 Pages: 4770-4792, 2014. DOI: 10.1002/2013JD020855
- Darmenov, A., and I. N. Sokolik (2005), Identifying the regional thermal-IR radiative signature of mineral dust with MODIS, *Geophys. Res. Lett.*, **32**, L16803, doi:10.1029/2005GL023092.
- Darmenov, A., and I. N. Sokolik (2009), spatial variability of satellite visible radiances in dust and dust-cloud mixed conditions: Implications for dust detection, *Geophys. Res. Lett.*, **36**, L14811, doi:10.1029/2009GL038383.
- Dubovik, O., Holben, B., Eck, T. F., Smirnov, A., Kaufman, Y. J., King, M. D., et al. (2002), Variability of absorption and optical properties of key aerosol types observed in worldwide locations. *Journal of the Atmospheric Sciences*, **59**, 590–608.
- Dubovik, O., et al. (2006), Application of light scattering by spheroids for accounting for particle nonsphericity in remote sensing of desert dust, *J. Geophys. Res.*, **111**, D11208, doi:10.1029/2005JD006619.
- Dunion, J.P. and Velden, C.S., The Impact of the Saharan Air Layer on Atlantic Tropical Cyclone Activity, *Bulletin of the American Meteorological Society*, **90**, 353–365, 2004.

- Eck, T. F., B. N. Holben, J. S. Reid, O. Dubovik, A. Smirnov, N. T. O'Neill, I. Slutsker, and S. Kinne (1999), Wavelength dependence of the optical depth of biomass burning, urban, and desert dust aerosols, *J. Geophys. Res.*, 104(D24), 31333–31349, doi:10.1029/1999JD900923.
- Evan, A. T., A. K. Heidinger, and M. J. Pavolonis (2006), Development of a new over-water advanced very high resolution radiometer dust detection algorithm, *Int. J. Remote Sens.*, 27, 3903 – 3924, doi:10.1080/01431160600646359.
- Frey, R. A., S. A. Ackerman, Y. Liu, K. I. Strabala, H. Zhang, J. R. Key, and X. Wang, Cloud detection with MODIS, Part I: Improvements in the MODIS cloud mask for collection 5. *Journal of Atmospheric and Wateric Technology*, 25, 7, 1057-1072, 2008.
- Hansell R.A., S.C. Ou, K.N. Liou, J.K. Roskovensky, S.C. Tsay, C. Hsu, and Q. Ji (2007), Simultaneous Detection/Separation of Mineral Dust and Cirrus Clouds Using MODIS Thermal Infrared Window Data, *Geophys. Res. Lett.*, 34, L13802, doi:10.1029/2007GLO31035.
- Herman, J. R., P. K. Bhartia, O. Torres, N. C. Hsu, C. J. Seftor, and E. Celarier (1997), Global distribution of UV-absorbing aerosols from Nimbus 7/TOMS data, *J. Geophys. Res.*, 102, 16,911-16,921.
- Holben B.N., T.F. Eck, I. Slutsker, D. Tanré, J.P. Buis, A. Setzer, E. Vermote, J.A. Reagan, Y. Kaufman, T. Nakajima, F. Lavenu, I. Jankowiak, and A. Smirnov, 1998: AERONET - A federated instrument network and data archive for aerosol characterization, *Rem. Sens. Environ.*, 66, 1-16.
- Holben, B.N., Tanré, D., Smirnov, A., Eck, T.F., Slutsker, I., Abuhassan, N., Newcomb, W.W., Schafer, J.S., Chatenet, B., Lavenu, F., Kaufman, Y.J., Castle, J.V., Setzer, A., Markham, B., Clark, D., Frouin, R., Halthore, R., Karneli, A., O'Neill, N.T., Pietras, C., Pinker, R.T., Voss, K. and Zibordi, G. (2001). An emerging ground-based aerosol climatology: Aerosol optical depth from AERONET. *Journal of Geophysical Research* 106: doi: 10.1029/2001JD900014. issn: 0148-0227.
- Hsu, N. C., J. R. Herman, O. Torres, B. N. Holben, D. Tanre, T. F. Eck, A. Smirnov, B. Chatenet, and F. Lavenu (1999), Comparisons of the TOMS aerosol index with Sun-photometer aerosol optical thickness: Results and applications, *J. Geophys. Res.*, 104(D6), 6269–6279, doi:10.1029/1998JD200086.
- Hsu N.C., W. D. Robinson, S. W. Bailey, and P. J. Werdell (2000). The description of the SeaWiFS absorbing aerosol index *SeaWiFS NASA Technical Memorandum 2000-206892*, 10, 3-5
- Hsu, N.C., S.-C. Tsay, M. D. King, and J. R. Herman (2004), *Aerosol properties over bright reflecting source regions*, *IEEE Trans. Geosci. Remote Sens.*, 42 (3), 557-569, doi: 10.1109/TGRS.2004.824067.
- Hsu, N.C., S.-C. Tsay, M. D. King, and J. R. Herman (2006), Deep Blue *retrievals of Asian aerosol properties during ACE-Asia*, *IEEE Trans. Geosci. Remote Sens.*, 44 (11), 3180-3195, doi: 10.1109/TGRS.2006.879540.
- Hu, X. Q., Lu, N. M., Niu, T., and Zhang, P. (2008), Operational retrieval of Asian sand and dust storm from FY-2C geostationary meteorological satellite and its application to real time forecast in Asia, *Atmos. Chem. Phys.*, 8, 1649–1659.
- IPCC, 2007: Climate Change 2007: The Physical Science Basis. Contribution of Working Group I to the Fourth Assessment Report of the Intergovernmental Panel on Climate Change [Solomon, S., D. Qin, M. Manning, Z. Chen, M. Marquis, K.B. Averyt, M.Tignor and H.L. Miller (eds.)]. Cambridge University Press, Cambridge, United Kingdom and New York, NY, USA.
- Jankowiak, I., D. Tanré (1992), *Satellite Climatology of Saharan Dust Outbreaks: Method and Preliminary Results*. *J. Climate*, 5, 646–656.
- Kaufman, Y. J., et al., Operational remote sensing of tropospheric aerosol over land from EOS moderate resolution imaging spectroradiometer, *J. Geophys. Res.*, 102, 16,971-16,988, 1997.

- Kaufman, Y. J., D. Tanré, L. Remer, E. Vermote, A. Chu, and B. N. Holben (1997), Remote sensing of tropospheric aerosol from EOS-MODIS over the land using dark targets and dynamic aerosol models, *JGR-Atmosphere*, special issue on Remote Sensing of Aerosol and Atmospheric Corrections, 102,17051-17067.
- Kaufman, Y. J., Arnon Karnieli, Didier Tanré (2000), Detection of dust over deserts using satellite data in the solar wavelengths. *IEEE T. Geoscience and Remote Sensing (TGRS)* 38(1):525-531.
- Kim, K. M., Lau, W. K.-M., Sud, Y. C., and Walker, G. K. (2010), Influence of aerosol-radiative forcings on the diurnal and seasonal cycles of rainfall over West Africa and Eastern Atlantic Ocean using GCM simulations, *Clim. Dynam.*, 26, doi:10.1007/s00382-010-0750-1.
- King, M. D., Menzel, W. Paul, Y. Kaufmann, Didier T., B.-C. Gao, S. Platnick, S. Ackerman, L. Remer, R. Pincus, and P. A. Hubanks, Cloud and aerosol properties, precipitable water, and profiles of temperature and water vapor from MODIS. *IEEE Transactions on Geoscience and Remote Sensing*, 41, 442-458, 2003.
- Klüser, L., and K. Schepanski (2009), Remote sensing of mineral dust over land with MSG infrared channels: A new Bitemporal Mineral Dust index, *Remote Sens. Environ.*, 113, 1853–1867, doi:10.1016/j.rse.2009.04.012.
- Kotchenova, S.Y., E.F. Vermote, R. Matarrese, & F.J. Klemm, Jr. (2006), Validation of a vector version of the 6S radiative transfer code for atmospheric correction of satellite data. Part I: Path Radiance, *Applied Optics*, 45(26), 6726-6774.
- [Kwiatkowska, E. J.](#), [Bryan A. Franz](#), [Gerhard Meister](#), [Charles R. McClain](#), and [Xiaoxiong Xiong](#) (2008), Cross calibration of ocean-color bands from Moderate Resolution Imaging Spectroradiometer on Terra platform, *Applied Optics*, Vol. 47, Issue 36, pp. 6796-6810.
- Legrand, M., G. Cautenet, and J.-C. Buriez, Thermal impact of Saharan dust over land, Part II: application to satellite IR remote sensing, *J. Appl. Meteorol.*, 31, 181-193, 1992.
- Legrand, M., A. Plana-Fattori, and C. N'Doume, Satellite detection of dust using IR imagery of Meteosat 1. Infrared difference dust index, *J. Geophys. Res.*, 106, 18,251-18,274, 2001.
- Liu, Z., et al. (2008), CALIPSO lidar observations of the optical properties of Saharan dust: A case study of long-range transport, *J. Geophys. Res.*, 113, D07207, doi:10.1029/2007JD008878.
- Liu, Z., M. A. Vaughan, D. M. Winker, C. Kittaka, R. E. Kuehn, B. J. Getzewich, C. R. Trepte, and C. A. Hostetler, 2009: The CALIPSO lidar cloud and aerosol discrimination: Version 2 algorithm and initial assessment of performance. *J. Atmos. Oceanic Technol.*, 26, 1198–1213.
- Nicholson, S. E. (2000), Land surface processes and Sahel climate, *Rev. Geophys.*, 38, 117–139.
- Martins, J.V., D. Tanré, L. Remer, Y. Kaufman, S. Mattoo, R. Levy (2002), *MODIS Cloud screening for remote sensing of aerosol over oceans using spatial variability*. *Geophys. Res. Lett.*,29(12),10.1029/2001GL013252.
- Mielonen, T., Arola, A., Komppula, M., Kukkonen, J., Koskinen, J., de Leeuw, G., and Lehtinen, K. E. J. (2009), Comparison of CALIOP level 2 aerosol subtypes to aerosol types derived from AERONET inversion data, *Geophys. Res. Lett.*, 36, L18804, doi:10.1029/2009gl039609.
- Miller, S. D. (2003), A consolidated technique for enhancing desert dust storms with MODIS, *Geophys. Res. Lett.*, 30(20), 2071, doi:10.1029/2003GL018279.
- Platnick, S., M. King, S. A. Ackerman, P. W. Menzel, B. A. Baum, J. C. Riédi, R. A. Frey, The MODIS Cloud Products: Algorithms and Examples from Terra, *IEEE Transactions on Geoscience and Remote Sensing*, 41, 459-???, 2003
- Prata, A. J., Observations of volcanic ash clouds in the 10-12-MU-M window using AVHRR/2 data. *International Journal of Remote Sensing* 10(4-5), 751-761, 1989.

- Prospero, J. M. and Lamb, P. J.(2003), African droughts and dust transport to the Caribbean: Climate change implications, *Science*, 302, 1024–1027.
- Rember, L., Y. J. Kaufman, D. Tanré, D., S. Mattoo, D. A. Chu, J. V. Martins, R-R. Li, C. Ichoku, R. C. Levy, R. G. Kleidman, T. F. Eck, E. Vermote, and B. N. Holben, The MODIS aerosol algorithm, products, and validation. *J. Atmos. Sci.*, **62**, 947–973, 2005.
- Remer, L. A., D. Tanre, Y.J. Kaufman, R. Levy and S. Mattoo, Algorithm for Remote Sensing of Tropospheric aerosol from MODIS: Collection 5, Product ID MOD04/MYD04, 2006.
- Ramirez-Beltran, ND., R. Kuligowski and E. Harmsen (2008), Validation and Strategies to Improve the Hydro-Estimator and NEXRAD over Puerto Rico, 12th WSEAS International Conference on SYSTEMS, Heraklion, Greece, July 22-24.
- Schepanski, K., Tegen, I., Laurent, B., Heinold, B., & Macke, A. (2007), A new Saharan dust source activation frequency map derived from MSG–SEVIRI IR-channels. *Geophysical Research Letters*, 34, L18803. doi:10.1029/2007GL030168.
- Smirnov, A., BN Holben, TF Eck, O Dubovik, I Slutsker (2000), [Cloud-screening and quality control algorithms for the AERONET database](#), *Remote Sensing of Environment*, 73 (3), 337-349
- Sokolik, I. N. (2002), The spectral radiative signature of wind-blown mineral dust: Implications for remote sensing in the thermal IR region, *Geophys. Res. Lett.*, 29(24), 2154, doi:10.1029/2002GL015910.
- Tan, S.-C., G.-Y. Shi, J.-H. Shi, H.-W. Gao, and X. Yao (2011), Correlation of Asian dust with chlorophyll and primary productivity in the coastal seas of China during the period from 1998 to 2008, *J. Geophys. Res.*, 116, G02029, doi:10.1029/2010JG001456.
- Tanre, D., and M. Legrand, On the Satellite Retrieval of Saharan Dust Optical Thickness Over Land: Two Different Approaches, *J. Geophys. Res.*, **96**, 5221–5227, 1991.
- Torres, O., Bhartia, P.K., Herman, J.R., Sinyuk, A. (2002), "Aerosol properties from EP-TOMS near UV observations", *Adv Space Res.*, 29, 1771-1780.
- Vaughan, M., and Coauthors, 2009: Fully automated detection of cloud and aerosol layers in the CALIPSO lidar measurements. *J. Atmos. Oceanic Technol.*, 26, 2034–2050
- Wilks, D.S. (1995), *Statistical Methods in the Atmospheric Sciences: An Introduction*. Academic Press, San Diego, 467 pp.
- Verge-Depre, G., M. Legrand, C. Moulin, A. Alias, and P. Francois, Improvement of the detection of desert dust over the Sahel using METEOSAT IR imagery, *Ann. Geophys.*, **24**, 2065-2073, 2006.
- Winker, D. M., M. A. Vaughan, A. Omar, Y. X. Hu, K. A. Powell, Z. Y. Liu, W. H. Hunt, and S. A. Young (2009), Overview of the CALIPSO mission and CALIOP data processing algorithms, *J. Atmos. Oceanic Technol.*, 26, 2310–2323, doi:10.1175/2009JTECHA1281.1.
- Winker, D. M., et al. (2010), The CALIPSO mission: A global 3D view of aerosols and clouds, *Bull. Am. Meteorol. Soc.*, 91, 1211–1229, doi:10.1175/2010BAMS3009.
- Xie, Y., (2009), Detection of smoke and dust aerosols using Multi-Sensor Satellite remote sensing measurements. Department of Geography and Geoinformation Science, George Mason University, Doctor of Philosophy.
- Yoshioka, M. and Mahowald, N. M. (2007), Impact of desert dust radiative forcing on Sahel precipitation: Relative importance of dust compared to sea surface temperature variations, vegetation changes, and greenhouse gas warming, *J. Climate*, 20, 1445–1467.
- Zhao, C., Liu, X., Ruby Leung, L., and Hagos, S. (2011), Radiative impact of mineral dust on monsoon precipitation variability over West Africa, *Atmos. Chem. Phys.*, 11, 1879–1893, doi:10.5194/acp-11-1879-2011.

Zhao, T. X.-P., S. Ackerman, and W. Guo (2010), Dust and smoke detection for multi-channel imagers. *Remote Sens.*, 2, 2347–2368, doi:10.3390/rs2102347.

---